

2013

# Patient-Specific Modeling Of Adult Acquired Flatfoot Deformity Before And After Surgery

Edward Meade Spratley

*Virginia Commonwealth University*

Follow this and additional works at: <http://scholarscompass.vcu.edu/etd>

 Part of the [Biomedical Engineering and Bioengineering Commons](#)

© The Author

---

Downloaded from

<http://scholarscompass.vcu.edu/etd/3278>

This Dissertation is brought to you for free and open access by the Graduate School at VCU Scholars Compass. It has been accepted for inclusion in Theses and Dissertations by an authorized administrator of VCU Scholars Compass. For more information, please contact [libcompass@vcu.edu](mailto:libcompass@vcu.edu).

© Edward Meade Spratley, 2013

All Rights Reserved

PATIENT-SPECIFIC MODELING OF ADULT ACQUIRED FLATFOOT  
DEFORMITY BEFORE AND AFTER SURGERY

A Dissertation submitted in partial fulfillment of the requirements for the degree of Doctor of  
Philosophy in Biomedical Engineering at Virginia Commonwealth University

by

EDWARD MEADE SPRATLEY

B.S., University of Virginia, 2004

M.S., Virginia Commonwealth University, 2009

Director: Jennifer S. Wayne, Ph.D.

Departments of Biomedical Engineering & Orthopaedic Surgery

Virginia Commonwealth University

Richmond, Virginia

November, 2013

## ACKNOWLEDGEMENT

It seems very strange to be writing an acknowledgments page and setting about wrapping up my duties here at VCU. While I'm sure no one ever says that this time has come too soon, it is nonetheless bittersweet to be moving on. Over the past years, I've come to view VCU as a home away from home and certainly much more than just the place I went for a degree. So, first and foremost, for that welcome feeling, and for any positive professional skill or trait that I may claim, I am indebted to my wonderful advisor Dr. Jennifer Wayne. She has helped me in so many ways in her capacity as a teacher, a mentor, a colleague, and finally as a friend. I count myself lucky to have been able to study under her for these past six years.

I would also like to thank my many peers and lab mates, past and present, for their friendship and excellent collaboration. Among these especially, I would like to thank Johnny Owen for his guidance, statistics wizardry, and unflappable, kind demeanor; Sean Higgins and Charles Taylor for exposing me to new skills and challenges, as well as being terrific friends; Erika Matheis for all her efforts and sarcastic charm as we worked together on this study; and Ruchi Chande for putting up with me and always setting such a fine example of hard work, compassion, and humor.

I would like to acknowledge Dr. Gerald Miller who has served as both a Master's and Doctoral advisor to me and been a mentor and confidant since my first year here at VCU. He has been a great source of support and inspiration and no small amount of prodding. Thank you to my committee members and the faculty and staff who have helped us get this project off the ground, especially Dr. Robert Adelaar for his vision and enthusiasm for our work; Carol Ford and Barbara Ennis for coordinating all the schedules of the doctors and our patients; and Dr. Curtis Hayes and Lanea Bare for helping us gather and make sense of all the x-rays and MRIs.

Finally, I need to thank my family and friends for all their support and for making Richmond home now for so many years. Thank you to my parents Katherine and Jack who have always encouraged me in everything I do. Thanks to my Grandmother for all that she has done to help me through this program. Lastly, thank you to my wife Jennifer, for just absolutely everything. She has been my loudest cheerleader and best friend for so many years and I can't wait to see what's in store for us next.

# TABLE OF CONTENTS

|  | Page      |
|--|-----------|
| ACKNOWLEDGEMENT .....                                  | iii       |
| TABLE OF CONTENTS.....                                 | iv        |
| LIST OF FIGURES .....                                  | ix        |
| LIST OF TABLES .....                                   | xiii      |
| ABSTRACT.....  | xiv       |
| <b>1. INTRODUCTION.....</b>                            | <b>1</b>  |
| 1.1 Overview Of Computational Modeling .....           | 1         |
| <i>1.1.1 Finite Element Analysis .....</i>             | <i>1</i>  |
| <i>1.1.2 Rigid Body Kinematics.....</i>                | <i>2</i>  |
| 1.2 Scope of this Dissertation .....                   | 5         |
| <b>2. FOOT AND ANKLE ANATOMY .....</b>                 | <b>6</b>  |
| 2.1 Bony Anatomy .....                                 | 6         |
| 2.2 Ligaments.....                                     | 12        |
| 2.3 Muscle Constraints.....                            | 17        |
| <b>3. ADULT ACQUIRED FLATFOOT DEFORMITY .....</b>      | <b>21</b> |
| 3.1 Clinical Presentation and Diagnosis .....          | 21        |
| <i>3.1.1 Radiographic Evaluation .....</i>             | <i>22</i> |
| <i>3.1.2 Soft-Tissue and Kinematic Evaluation.....</i> | <i>25</i> |
| 3.2 Etiology.....                                      | 26        |

|           |  |    |
|-----------|--|----|
| 3.2.1     | <i>Posterior Tibial Tendon Dysfunction</i> ..... | 27 |
| 3.2.2     | <i>Ligamentous Changes</i> .....                 | 28 |
| 3.3       | Stages of AAFD.....                              | 29 |
| 3.4       | Treatment .....                                  | 31 |
| 3.4.1     | <i>Tendon Transfer as PTT Augmentation</i> ..... | 33 |
| 3.4.2     | <i>Medializing Calcaneal Osteotomy</i> .....     | 36 |
| <b>4.</b> | <b>STUDY DESIGN AND DATA ACQUISITION</b> .....   | 38 |
| 4.1       | Patient Recruitment.....                         | 38 |
| 4.2       | X-ray .....                                      | 39 |
| 4.3       | Plantar Force Measurements.....                  | 41 |
| 4.4       | Magnetic Resonance Imaging (MRI).....            | 41 |
| 4.4.1     | <i>Tissue Attenuation</i> .....                  | 44 |
| 4.5       | Study Objectives .....                           | 46 |
| <b>5.</b> | <b>MODEL CREATION</b> .....                      | 48 |
| 5.1       | Overview.....                                    | 48 |
| 5.2       | Mask Creation And Thresholding.....              | 49 |
| 5.3       | Preprocessing .....                              | 50 |
| 5.3.1     | <i>Morphology Operations</i> .....               | 51 |
| 5.4       | Stereolithography (STL) Files .....              | 53 |
| 5.4.1     | <i>Mesh Quality</i> .....                        | 55 |
| 5.4.2     | <i>Smoothing</i> .....                           | 56 |
| 5.4.3     | <i>Triangle Reduction</i> .....                  | 57 |

|           |  |           |
|-----------|--|-----------|
| 5.5       | Characterizing The Models .....                  | 60        |
| 5.5.1     | <i>Long Bone Axes</i> .....                      | 60        |
| 5.5.2     | <i>Talar Dome</i> .....                          | 62        |
| 5.6       | Anatomy Reconstruction .....                     | 65        |
| 5.6.1     | <i>5th Metatarsals</i> .....                     | 66        |
| 5.6.2     | <i>Proximal Tibia and Fibula</i> .....           | 68        |
| <b>6.</b> | <b>RIGID-BODY KINEMATIC SIMULATIONS</b> .....    | <b>70</b> |
| 6.1       | Overview .....                                   | 70        |
| 6.2       | Defining Neutral Plantarflexion .....            | 70        |
| 6.3       | Origins And Insertions .....                     | 73        |
| 6.4       | COSMOSMotion .....                               | 74        |
| 6.4.1     | <i>Solver Parameters</i> .....                   | 75        |
| 6.4.2     | <i>Contact parameters</i> .....                  | 76        |
| 6.5       | Body Weight And Muscles .....                    | 79        |
| 6.5.1     | <i>Achilles Tendon Course</i> .....              | 81        |
| 6.5.2     | <i>FHL Tendon Course</i> .....                   | 82        |
| 6.5.3     | <i>FDL Tendon Course</i> .....                   | 83        |
| 6.5.4     | <i>Peronei Tendon Courses</i> .....              | 85        |
| 6.6       | Ligament Constraints .....                       | 87        |
| 6.6.1     | <i>Ligament Arrangement and Properties</i> ..... | 88        |
| 6.6.2     | <i>Mechanical Modeling</i> .....                 | 92        |
| 6.6.3     | <i>FORTTRAN Expressions</i> .....                | 93        |



|  |            |
|--|------------|
| <b>7. PREOPERATIVE MODEL/PATIENT AGREEMENT .....</b>           | <b>95</b>  |
| 7.1 Overview.....  | 95         |
| 7.2 Methods.....   | 95         |
| 7.2.1 <i>Tissue Grading</i> .....                              | 95         |
| 7.2.2 <i>Model Loading</i> .....                               | 96         |
| 7.2.3 <i>Measurements and Validation</i> .....                 | 97         |
| 7.3 Results.....   | 100        |
| 7.3.1 <i>Population Characteristics</i> .....                  | 100        |
| 7.3.2 <i>Radiographic Validation - Preoperatively</i> .....    | 103        |
| 7.4 Discussion .....   | 107        |
| <b>8. POSTOPERATIVE MODEL/PATIENT AGREEMENT .....</b>          | <b>112</b> |
| 8.1 Overview.....  | 112        |
| 8.2 Methods.....   | 113        |
| 8.2.1 <i>X-ray and Plantar Force Data Collection</i> .....     | 113        |
| 8.2.2 <i>Model Creation and Loading</i> .....                  | 117        |
| 8.2.3 <i>Measurements and Validation</i> .....                 | 120        |
| 8.3 Results.....   | 121        |
| 8.3.1 <i>Radiographic Validation - Postoperatively</i> .....   | 121        |
| 8.3.2 <i>Plantar Force Validation</i> .....                    | 124        |
| 8.3.3 <i>Soft-tissue Strains and Joint Contact Force</i> ..... | 125        |
| 8.4 Discussion .....   | 127        |
| <b>9. PARAMETRIC ANALYSIS.....</b>                             | <b>135</b> |

|            |  |            |
|------------|--|------------|
| 9.1        | Overview .....   | 135        |
| 9.2        | Methods.....   | 135        |
| 9.3        | Results.....   | 138        |
| 9.3.1      | <i>Radiographic Predictions</i> .....                                | 138        |
| 9.3.2      | <i>Plantar Force Predictions</i> .....                               | 142        |
| 9.3.3      | <i>Soft-tissue Strains and Joint Contact Force Predictions</i> ..... | 144        |
| 9.4        | Discussion .....   | 146        |
| <b>10.</b> | <b>FUTURE DIRECTIONS AND CONCLUSIONS.....</b>                        | <b>151</b> |
|            | Literature Cited .....   | 154        |
|            | Additional Acknowledgements.....                                     | 168        |
|            | APPENDIX A .....   | 169        |
|            | List of Abbreviations .....  | 169        |
|            | General Abbreviations .....  | 169        |
|            | Anatomic Abbreviations .....   | 170        |
|            | X-ray measure Abbreviations .....                                    | 171        |
|            | APPENDIX B .....   | 172        |
|            | STL Characteristics.....   | 172        |
|            | APPENDIX C .....   | 174        |
|            | Ligament Properties .....  | 174        |
|            | APPENDIX D.....  | 176        |
|            | APPENDIX E .....   | 177        |
|            | VITA.....  | 176        |

## LIST OF FIGURES

|  | Page: |
|--|-------|
| Figure 2-1: Tibia and fibula shown with interosseous membrane. ....              | 8     |
| Figure 2-2: Bones comprising the foot and ankle. ....                            | 9     |
| Figure 2-3: Joint divisions of the foot. ....                                    | 10    |
| Figure 2-4: Medial and lateral arches of the foot. ....                          | 12    |
| Figure 2-5: Lateral ankle and hindfoot ligaments. ....                           | 13    |
| Figure 2-6: Medial ankle and hindfoot ligaments. ....                            | 14    |
| Figure 2-7: Major divisions of the spring ligament complex.. ....                | 15    |
| Figure 2-8: Overview of the short interosseous ligaments of the foot.....        | 16    |
| Figure 2-9: Bands of the plantar fascia. ....                                    | 17    |
| Figure 2-10: Medial view of the foot showing invertor tendons .....              | 19    |
| Figure 2-11: Lateral view of the foot showing evtor tendons.....                 | 20    |
| Figure 3-1: Normal and AAFD afflicted foot. ....                                 | 22    |
| Figure 3-2: Diagram of most often used AAFD measures in the ML view. ....        | 24    |
| Figure 3-3: Diagram of the most often used AAFD measures in the AP view. ....    | 24    |
| Figure 3-4: Example of a plantar pressures contour map from an AAFD patient..... | 26    |
| Figure 3-5: Anterior view of an AAFD patient. ....                               | 27    |
| Figure 3-6: Intraoperative view of FHL tendon transfer surgery. ....             | 35    |
| Figure 3-7: Radiographs of MCO on a right foot. ....                             | 37    |

|  |    |
|--|----|
| Figure 4-1: Diagrams of the three x-rays taken for each patient..                | 40 |
| Figure 4-2: Imaging jig used for initial MRI sequences.                          | 43 |
| Figure 4-3: Typical images for each of the five MRI sequences used.....          | 44 |
| Figure 5-1: Example of masks created to isolate bones from the DESS scans.....   | 50 |
| Figure 5-2: Typical workflow for masking individual bones from MRI.....          | 52 |
| Figure 5-3: Scaling of MIMICS masks using the "dilate" tool.....                 | 53 |
| Figure 5-4: Representation of how masks are tessellated.....                     | 55 |
| Figure 5-5: Example of the R-in/R-out shape quality metric is used. ....         | 56 |
| Figure 5-6: Example STL body of a talus with morphology operations. ....         | 59 |
| Figure 5-7: Isometric view showing the best-fit tibia diaphyseal long axis. .... | 62 |
| Figure 5-8: Isometric view of best-fit tibiotalar flexion/extension axis ....    | 65 |
| Figure 5-9: Typical reconstruction of the 5th metatarsal bone. ....              | 67 |
| Figure 5-10: Tibia model combined high and lower resolution STL meshes.....      | 69 |
| Figure 6-1: Neutral plantar/dorsiflexion positioning of the foot model. ....     | 72 |
| Figure 6-2: Isometric view of the model loading pin assembly.....                | 73 |
| Figure 6-3: COSMOSMotion interface for input of ADAMS solver conditions. ....    | 76 |
| Figure 6-4: Penalty regularization approach for solving rigid body contacts..... | 77 |
| Figure 6-5: COSMOSMotion interface for defining the contact condition.....       | 79 |
| Figure 6-6: View of a calcaneus with the four Achilles insertion points.....     | 82 |
| Figure 6-7: Right foot model under load showing the FHL. ....                    | 83 |
| Figure 6-8: Right foot model under load showing the FDL. ....                    | 85 |
| Figure 6-9: Right foot model showing the PL and PB.....                          | 87 |

|  |     |
|--|-----|
| Figure 6-10: Model with proximal tibiofibular ligaments and interosseous membrane.....   | 89  |
| Figure 6-11: Model with passive soft-tissue elements.....                                | 90  |
| Figure 6-12: Model showing spring ligament bands. ....                                   | 91  |
| Figure 6-13: Model showing plantar fascia and deep tissues of the sole of the foot. .... | 92  |
| Figure 7-1: Radiographic measurements for ML view .....                                  | 98  |
| Figure 7-2: Radiographic measurements for standard AP view .....                         | 99  |
| Figure 7-3: Plot of model mean ANGLE predictions versus patient observations.....        | 105 |
| Figure 7-4: Plot of model mean DISTANCE predictions versus patient observations .....    | 105 |
| Figure 7-5: Bland-Altman plots for the ML talo-1st metatarsal angle. ....                | 106 |
| Figure 7-6: Bland-Altman plots for the AP talonavicular angle.....                       | 107 |
| Figure 7-7: Bland-Altman plots for the ML 1st cuneiform height. ....                     | 107 |
| Figure 8-1: Radiographic measurements for ML view.....                                   | 114 |
| Figure 8-2: Radiographic measurements for standard AP view .....                         | 115 |
| Figure 8-3: Example of plantar force profile obtained from HRMat® software.....          | 116 |
| Figure 8-4: Creation of three region plantar force mask.....                             | 116 |
| Figure 8-5: Creation of patient-specific MCO.....  | 119 |
| Figure 8-6: Average ANGLES for patient and model pre- and postoperatively .....          | 123 |
| Figure 8-7: Average DISTANCES for patient and model pre- and postoperatively .....       | 123 |
| Figure 8-8: Changes in patient and model plantar force loading after surgery .....       | 125 |
| Figure 8-9: Changes in model soft-tissue strains after surgery.....                      | 126 |
| Figure 8-10: Changes in medial and lateral column joint contact in the model .....       | 127 |
| Figure 9-1: Example variable MCO creation workflow. ....                                 | 137 |

|   |     |
|---|-----|
| Figure 9-2: Overview of treatment effect on simulated x-ray angle measures. ....          | 139 |
| Figure 9-3: Overview of treatment effect on simulated x-ray distance measures. ....       | 139 |
| Figure 9-4: Average ANGLE effects of isolated FHL tendon transfer. ....                   | 140 |
| Figure 9-5: Average DISTANCE effects of isolated FHL tendon transfer. ....                | 141 |
| Figure 9-6: Average ANGLE effects of 10mm MCO following tendon transfer.....              | 142 |
| Figure 9-7: Average DISTANCE effects of 10mm MCO following tendon transfer. ....          | 142 |
| Figure 9-8: Average plantar force distribution for across states.....                     | 144 |
| Figure 9-9: Changes in average soft-tissue strains predicted across the four states. .... | 145 |
| Figure 9-10: Changes in average joint contact force predicted across the four states..... | 146 |

## LIST OF TABLES

|  | Page: |
|--|-------|
| Table 3-1: Stages of AAFD .....  | 31    |
| Table 4-1: MRI sequence acquisition parameters.....                              | 42    |
| Table 4-2: Four-tiered grading scale of investigated soft-tissues. ....          | 45    |
| Table 4-3: Observed patient values for grading of MRIs. ....                     | 45    |
| Table 6-1: Fat pad thicknesses measured on the loaded ML X-rays .....            | 71    |
| Table 6-2: Muscle loading incorporated into each of the six models. ....         | 81    |
| Table 7-1: Preoperative muscle loading (N) scaled relative to patient BW. ....   | 96    |
| Table 7-2: Modified four-tiered grading of the MRIs. ....                        | 101   |
| Table 7-3: Patient radiographic angle means compared to published values .....   | 102   |
| Table 7-4: Patient radiographic distance means compared to published values..... | 103   |
| Table 7-5: Model to Patient agreement for all radiographic measures .....        | 104   |
| Table 8-1: Postoperative muscle loading (N) scaled relative to patient BW .....  | 118   |
| Table 8-2: Model to Patient agreement for all postoperative x-ray measures ..... | 124   |

## **ABSTRACT**

### **PATIENT-SPECIFIC MODELING OF ADULT ACQUIRED FLATFOOT DEFORMITY BEFORE AND AFTER SURGERY**

By Edward Meade Spratley, B.S., M.S.

A Dissertation submitted in partial fulfillment of the requirements for the degree of Doctor of Philosophy in Biomedical Engineering at Virginia Commonwealth University.

Virginia Commonwealth University, 2013

Major Director: Jennifer S. Wayne, Ph.D.

Professor, Biomedical Engineering & Orthopaedic Surgery; Director, Orthopaedic Research Laboratory

The use of computational modeling is an increasingly commonplace technique for the investigation of biomechanics in intact and pathological musculoskeletal systems. Moreover, given the robust and repeatable nature of computer simulation and the prevalence of software techniques for accurate 3-D reconstructions of tissues, the predictive power of these models has increased dramatically. However, there are no patient-specific kinematic models whose function is dictated solely by physiologic soft-tissue constraints, articular shape and contact, and without idealized joint approximations. Moreover, very few models have attempted to predict surgical effects combined with postoperative validation of those predictions.

Given this, it is not surprising that the area of foot/ankle modeling has been especially underserved. Thus, we chose to investigate the pre- and postoperative kinematics of Adult Acquired Flatfoot Deformity (AAFD) across a cohort of clinically diagnosed sufferers. AAFD was chosen as it is a chronic and degenerative disease wherein degradation of soft-tissue



supporters of the medial arch eventually cause gross malalignment in the mid- and hindfoot, along with significant pain and dysfunction. Also, while planar radiographs are still used to diagnose and stage the disease, it is widely acknowledged that these 2-D measures fail to fully describe the 3-D nature of AAFD.

Thus, a population of six patient-specific rigid-body computational models was developed using the commercially available software packages Mimics® and SolidWorks® in order to investigate foot function in patients with diagnosed Stage IIb AAFD. Each model was created from patient-specific sub-millimeter MRI scans, loaded with body weight, individualized muscle forces, and ligament forces, in single leg stance. The predicted model kinematics were validated pre- and postoperatively using clinically utilized radiographic angle distance measures as well as plantar force distributions. The models were then further exploited to predict additional biomechanical parameters such as articular contact force and soft-tissue strain, as well as the effect of hypothetical surgical interventions. Subsequently, kinematic simulations demonstrated that the models were able to accurately predict foot/ankle motion in agreement with their respective patients. Additionally, changes in joint contact force and ligament strain observed across surgical states further elucidate the complex biomechanical underpinnings of foot and ankle function.

# 1. INTRODUCTION

## 1.1 OVERVIEW OF COMPUTATIONAL MODELING

Computer Aided Design (CAD) offers numerous advantages for evaluating musculoskeletal function, identifying pathomechanic conditions, and the ability to pre-operatively predict the outcome of corrective procedures. As a consequence, there have been a great many CAD musculoskeletal models developed to evaluate and predict joint loads, load and stress propagation, muscle efficiency and ergonomics, joint kinematics, and orthopaedic implant design, just to name a few. Indeed, even in the narrowed scope of this work, there are an ever increasing number of foot and ankle musculoskeletal models being developed that aim to investigate the biomechanics of the intact and pathologic body.<sup>1-11</sup> Of these, the majority are derived from CT or MRI of native geometry whether from in vivo or cadaveric tissues.<sup>12</sup>

### 1.1.1 *Finite Element Analysis*

Modeling of the foot and ankle, or indeed any other portion of the musculoskeletal system, is typically done using one of two computational approaches. The first and historically more common of these is the Finite Element Analysis method (FEA). In the broadest terms, this approach allows for the analysis of material and structural deformation in the system of interest. Briefly, this is done by discretizing the musculoskeletal geometry of interest, be it bone or soft-tissue, using many small and numerically simple elements wherein the mathematic expressions governing each segment are assigned based on the material stress/strain behavior. Each of these

elements is connected to all its adjacent neighbors at nodes and thereby yield a continuous mesh of interdependent mathematic entities, much like the individual segments of a hammock or fishing net are connected at knots. Boundary and initial value conditions, such as fixations, forces, or displacements, are then imparted to the entire system and the resulting deformation and force behavior observed. Conceptually, this is analogous to approximating any curved line with many smaller linked straight lines; the more line elements, the more accurate the approximation.

Given the numerical complexity of this approach, most investigators have limited their analysis to quasi-static, small deformation studies; yet still, these FEA models can incorporate hundreds of thousands of elements and require days or weeks to solve on typical workstations. While there are scores of these such models, a few recent examples for the foot and ankle include the work of Cheung et al. and more recently Cheng et al. who both sought to characterize plantar fascia loading and to further quantify the windlass effect.<sup>1-3</sup> Isvilanonda et al. created a model of the first ray of the foot in order to investigate surgical reconstructions of hallux valgus deformity.<sup>6</sup> And finally, Yu et al. created a model to investigate the altered biomechanics in forefoot loading while standing in high heel shoes.<sup>11</sup>

### *1.1.2 Rigid Body Kinematics*

The second main type of computational method is rigid body kinematics. Here the bony tissues are assumed to be rigid beams connected by force vectors representing muscles and ligaments. The assumption of rigidity offers advantages and disadvantages. The biggest drawback is that these assumptions only hold for testing scenarios where the expected forces within the system are sufficiently small that the expected deformation of the bones is infinitesimal. For example, a tibia bearing normal bodyweight with undergo  $\gg 1\%$  strain and

may therefore be assumed rigid. By contrast, a tibia bearing the load of a fall from great height would grossly deform and would therefore not be accurately modeled through a rigid body approach. The main advantage of rigid body modeling is that it is computationally efficient since the geometry is not discretized and the equations of motion are readily solved both analytically and numerically. These computational savings manifest as the ability to solve large, complex, dynamic systems without the assumption of quasi-static loading and all in a reasonable amount of simulation time (hours, not days).

Rigid body modeling can be further divided into two general categories; inverse kinematics and forward kinematics. The most widely used of these is inverse kinematics wherein the relative motion between rigid segments, usually obtained from in vivo kinematic data, is prescribed as an input so that the resulting joint forces and requisite muscle or ligament loads can be calculated. While this approach can yield insight into the system biomechanics, e.g. changing muscle moment arms and kinematic efficiency, the joints must be represented as simplified mechanical joints with fixed centers. This approximation means that an inverse kinematics approach is therefore unable to predict physiologic contact forces and locations, nor is it able to predict ligament loads across joints with floating rotation axes. In this category, some of the first work was put forth by Delp et al. and described a lower extremity model wherein bony anatomy, idealized joints, and physiologic muscle/tendon complex actuators were driven by kinematic data. Thus, the outputs of these models were the requisite joint torques and muscle tensions required to maintain equilibrium.<sup>13,14</sup> This software eventually became the Software for Interactive Musculoskeletal Modeling (SIMM) package and was perhaps the area's first dedicated computational musculoskeletal analysis software. It is currently used by many

authors to derive the inverse kinematics of nearly any joint in the body.<sup>15</sup> Specifically as it relates to flatfoot, Salathé and Arangio have published extensively regarding their 2-D and 3-D analytic models of the pre- and postoperative flatfoot model. In these experiments, the metatarsals are fixed against the ground while loaded by body weight. A minimization function was then used to calculate the lowest energy muscle loading scenario.<sup>8,16-18</sup> Like the work by Delp et al., these models also assumed simplified mechanical joints throughout the foot.

The second technique used in rigid body analysis is forward kinematics. Unlike in inverse kinematics, the relative motion of the segments is unknown initially. In short, forward kinematics requires explicit definitions of body weight and soft-tissue loads and the kinematics are the dependent variables. The earliest versions of these models utilized idealized joint definitions, similar to the inverse kinematics case, in order to connect in vivo electromyography measures of muscle output to movement tasks such as seated rise and jumping.<sup>19,20</sup> However, not until Kwak et al. offered up one of the first techniques for unconstrained body-body contact through the segment overlap penalty method did accurate predictions of joint loading in a musculoskeletal model become possible.<sup>21</sup> Subsequent to this, a number of authors, including those from this lab, have used the forward kinematics approach while utilizing Kwak et al.'s penalty regularization technique to allow physiologic joint function.<sup>7,9,10</sup> While representing an important improvement over idealized joint models, these later approaches still utilize simplified geometry and grouping of multiple bones into functional segments. To date, only Iaquinto and Wayne have described foot function using non-idealized joint contacts along with physiologic soft-tissue loading in a complete model of the intact foot.<sup>4,5</sup>

## 1.2 SCOPE OF THIS DISSERTATION

Currently, there exist no computational models of the foot, or any other joint, wherein function is predicted by solely by patient-specific geometry, physiologic articular contact, passive capsuloligamentous tension, muscle force, and body weight. Thus, this dissertation and the published and/or pending manuscripts comprising Chapters 7 and 8 are the first to describe the creation and application of population of 3-D patient-specific rigid-body computer models, derived through a consistent methodology, from diagnosed Stage IIb Adult Acquired Flatfoot Deformity (AAFD) patients.<sup>22</sup> The purpose of this work was to investigate pre- and postoperative foot biomechanics and the effect of surgical correction on joint kinematics, distributed plantar loading, soft-tissue strain, and articular contact force. Moreover, this dissertation will outline how those models were validated through their ability to predict clinically relevant radiographic measures.<sup>22</sup>

## **2. FOOT AND ANKLE ANATOMY**

The human lower extremity is a marvelously complex structure with many specific and nuanced adaptations allowing for decades of high-impact bipedal motion. Owing to this superb adaptation, the healthy foot and ankle will provide a lifetime of support in the activities of daily living with the potential to at an instant bear many times a person's full body weight while moving quickly over rapidly changing surfaces. Underlying this remarkable level of function is a uniquely adapted structure comprised of a multi-bone joint complex, a dense web of passive soft-tissues, and a myriad intrinsic and extrinsic muscles. Each of these tissues must work in concert to effect normal limb function and a deficit in any will manifest as disability.

Thus, in order to understand any sort of foot pathology, it is important to first understand the intact anatomy. Given its complexity, what follows will only be a cursory introduction to the foot and ankle, but it will nonetheless serve to put in context the origins of flatfoot pathology, the morphology of its deformity, and the mechanism of its repair.

### **2.1 BONY ANATOMY**

The structural foundation of the lower limb are the bones. Moving distally from the knee, the two large bones of the shin are the tibia and the fibula. The tibia is significantly larger than the fibula and is responsible for transmitting the majority of load from the proximal body down into the ground, while the fibula functions predominantly as an attachment site for various soft-tissues. The proximal end of the tibia terminates in the tibial plateau, a flat shelf aligned roughly

in the transverse plane, with an approximately trapezoidal cross section that is larger on the posterior aspect. On top of this shelf are two shallow ellipsoid depressions separated by a short ridge running anteroposterior; these features articulate and support the bone of the thigh, the femur. Moving distally from the plateau, there is a small notch laterally that accepts the proximal end of the fibula and is secured with thick capsule. This is the proximal tibiofibular articulation and it is nearly immobile. Continuing down, the tibia's cross section becomes triangular with the anterior shin being blade like. The slender fibula roughly parallels the tibial course and is tethered to it with a broad sheet of collagenous tissue known as the interosseous membrane and ligament. The distal end of both bones, their epiphyses, become bulbous anteriorly and posteriorly with the tibia having a shallow longitudinal depression along its lateral end that accepts the distal fibula, again anchored through strong capsule. [Figure 2-1] This is known as the distal tibiofibular articulation and it is slightly movable, though it is not directly effected on by any muscles. The inferior most surface of the tibial epiphysis is known as the plafond and is characterized by a cylindrical concavity that sweeps anteroposterior and is covered in hyaline (articular) cartilage. The medial and lateral most aspects of the tibia and fibula, respectively, extend inferiorly as large round processes known as the malleoli.



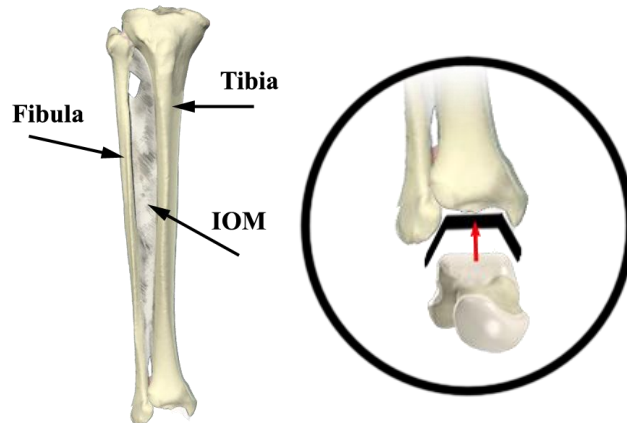


**Figure 2-1: Anterior view of the tibia and fibula shown with connecting interosseous membrane (IOM). INSET: The tibia-fibula-talus mortise joint.**

The concave tibial plafond, bolstered on either side by the malleoli, form a natural mortise into which fits the first of the tarsal bones, the talus. The superior portion of the talus is referred to as the dome and is shaped such as to form a congruous articulation with the tibial plafond.

[Figure 2-1] Likewise, its medial and lateral aspects are slightly concave and articulate with the medial and lateral malleoli. This is known as the talocrural joint and it is a synovial joint allowing large flexion/extension motion with limited inversion/eversion motion. Anteriorly, the talus narrows into the neck before becoming semi-spheroid and articulating with the navicular bone. On its inferior surface, the small squat talus has three ellipsoid concavities aligned along the posterior, medial, and anterior margins. Though distinct from one another, all three of these indentations articulate with the calcaneus and are collectively known as the subtalar joint.

Peculiarly, the talus has no muscular attachments and its motion is thus dictated solely by its relationship with the adjacent bones of the foot and ankle.<sup>23,24</sup> [Figure 2-2]

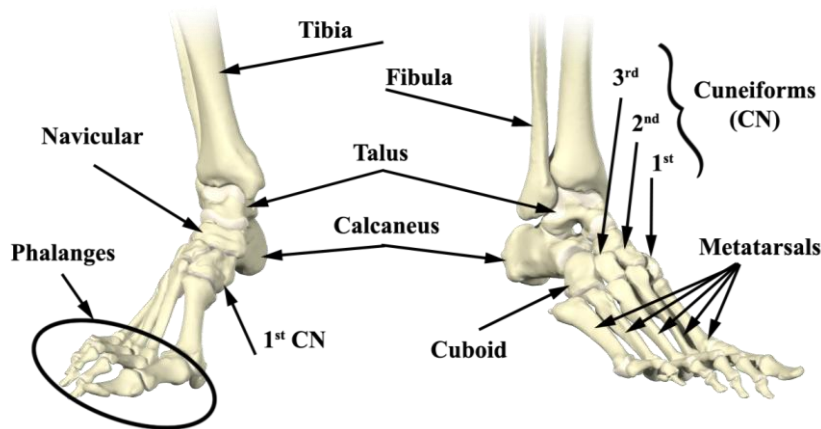


**Figure 2-2: Bones comprising the foot and ankle. LEFT: Anteromedial view. RIGHT: Anterolateral view.**

The calcaneus is the largest of the tarsal bones and not only transmits the most force into the ground, but also serves as the insertion for perhaps the most forceful muscle in the body, the triceps surae.<sup>23,24</sup> Its posterior aspect is dominated by the large calcaneal tuberosity onto which the Achilles tendon of the aforementioned triceps surae group inserts. Medially, a buttress of bone called the sustentaculum tali is cantilevered under the talus and supports the medial talocalcaneal articulation. Anteriorly, the calcaneus narrows before terminating in a small triangular saddle that articulates with the cuboid bone. Plantarly, the calcaneus is anchored to the ground only at the most posterior aspect. The anterior plantar surface is dominated by soft-tissue origins that draw the anterior foot posteriorly, much like a bow string drawing together the ends of a bow. More detail on this will be given in the following section. As a consequence of this, the calcaneus is pitched up anteriorly and does not bear much weight except in pathology. Taken together with the talus, these two bones form the hindfoot. [Figure 2-2]

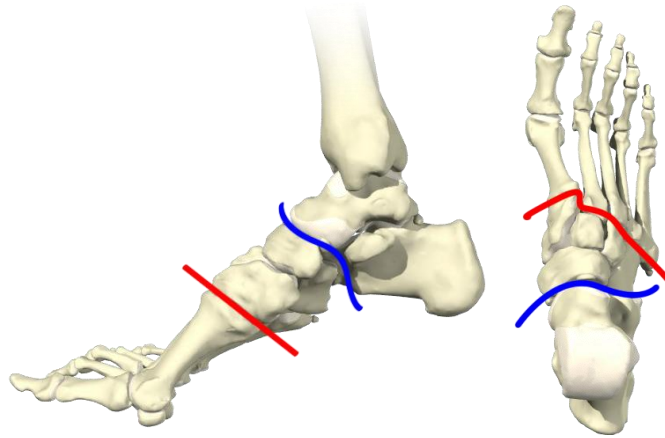


**Figure 2-3: Bony right foot showing the transverse tarsal (blue line) and tarsometatarsal (red line) joints. LEFT: Medial view. RIGHT: Dorsal view.**

Moving anteriorly into the midfoot, the calcaneus and talus articulate with the aptly named cuboid and navicular bones, respectively. This two joint complex is known as the transverse tarsal joint. [Figure 2-3] The talonavicular portion of the transverse tarsal joint is of particular interest to this work as it forms the superior border of the medial arch, and as such is the site where most flatfoot deformity will eventually manifest. In the healthy foot, the navicular bone is kidney shaped with a deep concavity on its posterior wall. This depression cradles and 'covers' the talar head. This orientation causes the talus to pitch plantarly and medially during pronation and toe off, thereby partially 'uncovering' the talar articular surface. Deformities such as flatfoot are evident when this uncovered state persists during stance alone or even during non-weight bearing. Anterior the navicular are the three cuneiform bones, numbered from medial to lateral, with the lateral most bone articulating with the cuboid. The 1st cuneiform is somewhat larger than the navicular and is roughly box shaped. The 2nd and 3rd cuneiforms are square on their dorsal aspects but taper to a wedge plantarly. The navicular, cuboid, and 1st, 2nd, and 3rd cuneiforms are collectively known as the midfoot.

Continuing anterior from the midfoot, the tarsal bones articulate with the five metatarsal bones, at the tarsometatarsal joint. [Figure 2-3] Of the metatarsals, the 1st and 5th are typically the largest and the center 2-4 are more slight. The anterior extents of all five metatarsals terminate with spheroid caps of bone that contact with the ground. Additionally, the first metatarsal will most often have two small sesamoid bones immediate plantar to its distal head. The five metatarsals together are collectively referred to as the forefoot. The anterior most portion of the foot is the phalanges. Metatarsals 2-5 are each extended by a series of three small phalanges, and the 1st metatarsals extended by just two. All together, the foot and ankle are comprised of 28 discrete bones.

Finally, just as the foot can be functionally divided along the coronal planes, i.e. the transverse tarsal and tarsometatarsal joints, so too can it be split from medial to lateral. For example, consider a portion of the body's force distributed from the calcaneus through the cuboid to the 4th and 5th metatarsals, and into the ground. This force is said to be transmitted down the lateral column of the foot, since the bones are so tightly bound in series. Likewise, force transmitted from the talus, through the cuneiforms, to the first three metatarsals is said to be carried by the medial column of the foot. [Figure 2-4] This designation further delineates the higher and more dynamic medial longitudinal arch, carried under the medial column, from the lower and more static lateral longitudinal arch, carried under the lateral column.

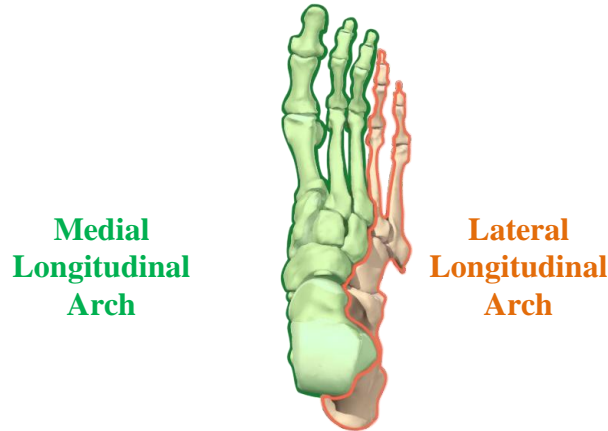


**Figure 2-4: Dorsal view of a right foot showing the bones comprising medial longitudinal arch (LEFT - green) and the lateral longitudinal arch (RIGHT - orange).**

## 2.2 LIGAMENTS

While the articulations of the foot are generally congruous, it is the ligaments that bolster and constrain the motion at all the joints. Some of these ligaments are just more aligned thickenings of joint capsule between adjacent bones while others are discrete, extracapsular structures spanning multiple articulations. In both cases, the function of the articulation(s), and ultimately the entire foot and ankle, is driven by the structure and organization of these tissues.

Beginning with the most mobile joint, the talocrural articulation is supported medially and laterally by a network of extracapsular collateral ligaments, (MCL and LCL). On the lateral side, these include the calcaneofibular (CaFi), and the anterior and posterior talofibular (TaFi-a, TaFi-p) ligaments.<sup>24-26</sup> Additionally, the superficial fibular retinaculum (SFR) is a functional restraint. [Figure 2-5] These tissues together work to guide talocrural joint motion and prevent excessive inversion. Notable ligament restraints in the vicinity of the lateral collaterals but with

differing functions include the lateral talocalcaneal (TaCa) and talocalcaneal interosseous (IOL) ligaments that support the subtalar joint.

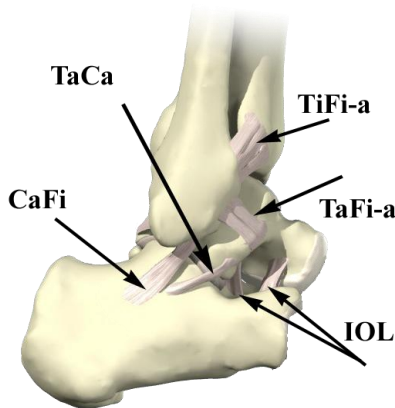


**Figure 2-5: Lateral view of right ankle and hindfoot ligaments. Clockwise from top: anterior tibiofibular (TiFi-a), anterior talofibular (TaFi-a), talocalcaneal (TaCa), calcaneofibular (CaFi), and talocalcaneal interosseous (IOL).**

On the medial side, those ligaments originating from the medial malleolus are collectively referred to as the deltoid ligaments. This complex is comprised of four major bands as well a number of minor bands and they act collectively to guide the talus in flexion extension relative to the tibia while limiting ankle eversion. The major bands are the anterior tibiotalar (TiTa-a) ligament, the tibionavicular (TiNa) ligament, and the tibiocalcaneal (TiCa) ligament. Minor bands, include the tibiospring (TiSp) that inserts onto the spring ligament complex (discussed below) and the posterior tibiotalar (TiTa-p) ligaments.<sup>23-28</sup> Ligaments with complementary function, but that do not originate on the tibia are often referred to generically as the medial collateral ligaments and include the medial and posterior talocalcaneal (TaCa-m, TaCa-p) ligaments. [Figure 2-6]

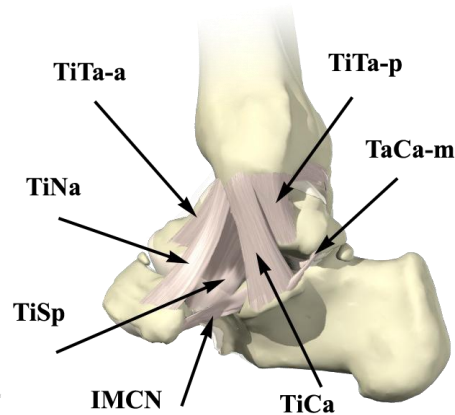


**Figure 2-6: Medial view of a right ankle and hindfoot ligaments. Clockwise from top: posterior tibiotalar (TiTa-p), medial talocalcaneal (TaCa-m), talocalcaneal (TaCa), inferomedial spring (IMCN), tibiospring (TiSp), tibionavicular (TiNa), and anterior tibiotalar (TiTa-a).**

Lying just inferior to the deltoid and medial collateral ligaments is the spring ligament complex. These tissues span anteriorly from the anteromedial calcaneus to the inferomedial navicular. Early anatomists described only the plantar most bands as being functionally supportive of the joint.<sup>23</sup> However, given its pertinence to midfoot pathologies such as flatfoot, intensive focus on the region has led to the identification of additional structures in the vicinity. Currently, the complex is understood to contain at least three distinct regions; the superomedial calcaneonavicular (SMCN), the middle calcaneonavicular (MCN), and the inferomedial calcaneonavicular (IMCN).<sup>29-31</sup> The SMCN originates on the medial border of the middle articular facet of the calcaneus and wraps medially with fibers inserting on the inferior, medial, and superior board of the navicular tuberosity. Often, these fibers interdigitate with those of the posterior tibial tendon at its insertion. The MCN originates just lateral the SMCN and travels obliquely anterior to insert on the inferomedial navicular between the tuberosity and beak. The

SMCN and MCN together create a sort of 'sling' in that the talar head rests. Interestingly, the constant compressive force of the talar head causes these ligaments to restructure somewhat, often to the extent that they develop articular cartilage and even sesamoid-like bones in their midsubstance. The third and final portion of the spring ligament, the IMCN, has discrete origins just inferior to the anterior articular facet of the calcaneus. The fibers then course anterior to insert on the inferior navicular, just lateral to the navicular beak. [Figure 2-7]

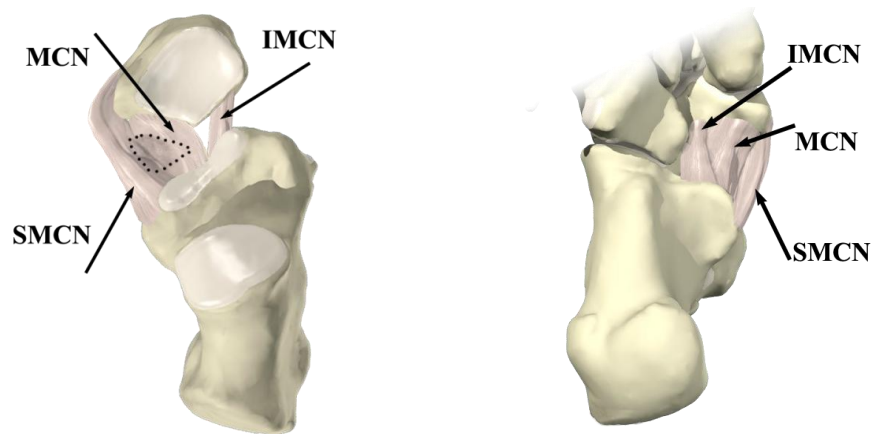


**Figure 2-7: Major divisions of the spring ligament complex. LEFT: Dorsal view. Outlined area indicates regions with articular cartilage. RIGHT: Plantar view.**

Moving into the mid- and forefoot, the deep dorsal and plantar aspects of the foot are dominated by a dense web of interosseous ligaments. The majority of these ligaments are short and exist as thickenings of the articular capsule. To generalize, most are aligned roughly perpendicular to the joint they cross and, with the exception of those ligaments crossing the transverse tarsal joint, do not allow much motion at their articulations. More specifically, these include the talonavicular (TaNa), calcaneonavicular (CaNa), calcaneocuboid (CaCu), naviculocuneiform (CnNa), naviculocuboid (CuNa), cuboidcuneiform (Cu#Cn), intercuneiform (INTCn), cuneometatarsal (CnMt), and intermetatarsal (INTMt) ligaments. [Figure 2-8]



On the dorsum of the foot, there are no substantial ligaments superficial to the deep interossei. From the plantar aspect however, there are two significant ligaments running longitudinally along the lateral half of the sole of the foot. [Figure 2-8] These are the long and short plantar ligament. The long plantar ligament originates at the anterior and plantar margin of the plantar fascia origin (discussed below) on the calcaneus. It travels slightly superiorly to insert on the proximal heads of the 2-5th metatarsals. The short plantar ligament sits just deep to the long and inserts more laterally just proximal to the peroneus longus' course under the cuboid. Both ligaments have the effect of drawing the forefoot closer to the hindfoot, thereby supporting the medial and lateral longitudinal arches of the foot.

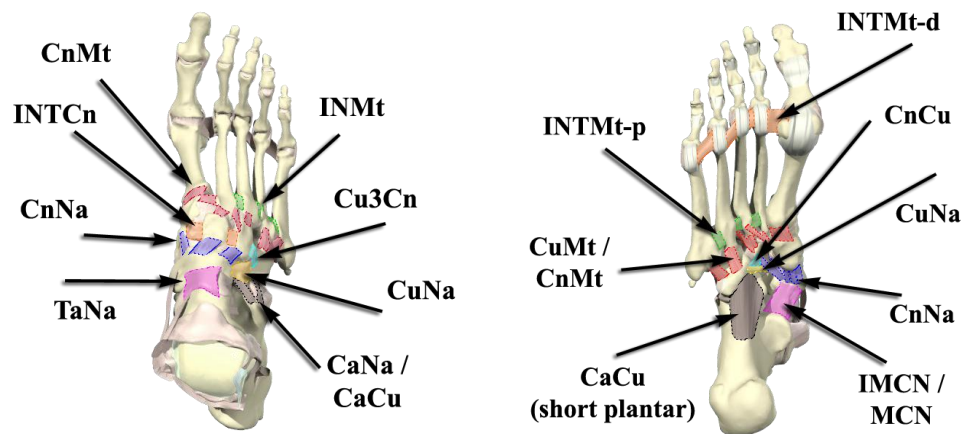


**Figure 2-8: Overview of the short interosseous ligaments of a right foot. LEFT: Dorsal view. RIGHT: Plantar view.**

A final passive soft-tissue support structure of note is the plantar fascia (PF). Though not a ligament, the plantar fascia is a broad stout tissue lying just deep to the plantar skin and fat. [Figure 2-9] The plantar fascia originates just anterior to the load bearing portion of the inferior calcaneus and courses anteriorly in two large segments. The larger of these segments is the central band which splits into five branches in the midfoot, with each branch extending to a distal

metatarsal head. By contrast, the lateral band remains mostly confined to one or two branches and inserts on the proximal 5th metatarsal. It is because of the plantar fascia's origin and line of action that the structure is often described as a functional extension of the Achilles tendon into the foot. As with the long and short plantar ligaments, the plantar fascia serves to draw the forefoot closer to the hindfoot, thereby bowing upward the lateral and especially the medial longitudinal arches.

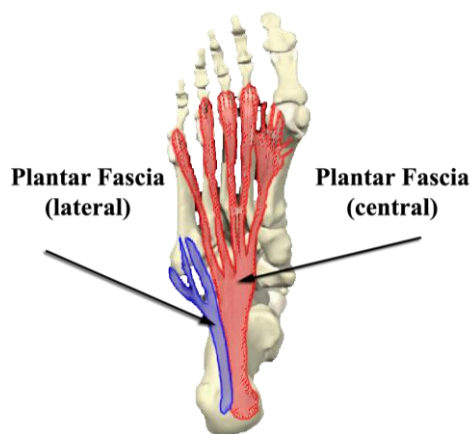


**Figure 2-9: Plantar view of a right foot showing the central (RIGHT - red) and lateral (LEFT - blue) bands of the plantar fascia.**

## 2.3 MUSCLE CONSTRAINTS

There are dozens of muscles, both intrinsic and extrinsic, that effect motion in the foot for maintaining balance or locomotion. However, within the scope of this work, there are five that are of special interest. The largest, already alluded to, is the triceps surae. This muscle complex occupies the posterior calf and is comprised of the medial and lateral gastrocnemius and the soleus muscles. These three heads coalesce into the stout Achilles tendon that inserts at the superoposterior calcaneal tuberosity. Through the Achilles, this muscle provides powerful

plantar flexion and slight inversion at the talocrural and subtalar joints, respectively. During normal gait, this action has the additional effect of bolstering the medial arch height by drawing tension into the plantar fascia during toe off, thereby raising talonavicular joint, a process known as the windlass mechanism. [Figure 2-10]

Arising out of the medial compartment of the lower leg, the posterior tibialis (PTT) is of unique concern to this work. This muscle arises from the posterior calf and turns anterior just behind the medial malleolus before inserting onto the navicular tuberosity. Given its physiologic cross sectional area, the (PTT) is uniquely advantaged to directly support the medial longitudinal arch through powerful inversion at the subtalar joint. Also arising from the posterior calf and traveling just deep to the PTT is the flexor digitorum longus (FDL). The main tendon dives plantarly and laterally just beyond the PTT insertion and splits into four branches that insert on the lateral four distal phalanges. The FDL's main actions are plantar flexion at the talocrural joint, flexion of the 2-5 toes, and support of the medial and lateral arches through a similar mechanism to that of the plantar fascia. While not as strong as the PTT, the FDL's proximity, course, and length make it an obvious candidate for tendon transfers in the foot. Finally, coursing deep to both the PTT and FDL, along the medial wall of the calcaneus is the flexor hallucis longus (FHL). This tendon also originates in the posterior calf, but it turns anteriorly under the sustentaculum tali and inserts on the distal phalanx of the great toe. Similar to the FDL, the FHL plantar flexes the talocrural joint, flexes the great toe, and supports the medial longitudinal arch. Also, the FHL is an obvious candidate for tendon transfers, perhaps more so than the FDL given its larger physiologic cross sectional area. [Figure 2-10]

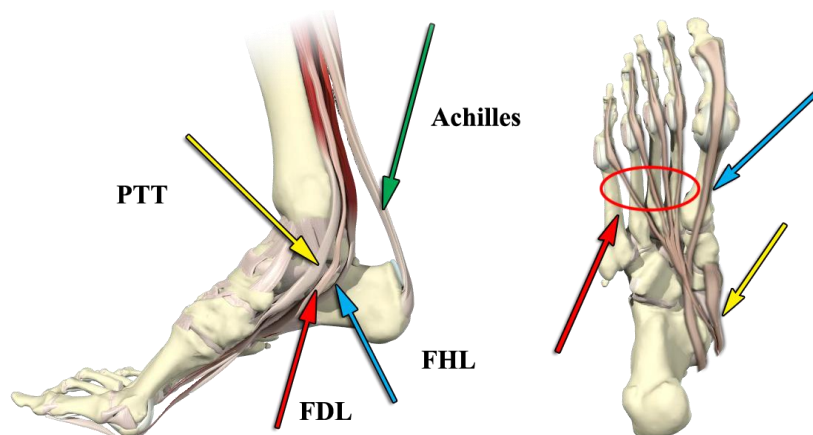


**Figure 2-10: LEFT: Medial view of a right foot showing inverter tendons. PTT (yellow); FDL (red); FHL (blue); Achilles (green). RIGHT: Plantar view.**

There are two large muscles of interest crossing the lateral aspect of the ankle joint as well. These are the peroneus longus (PL) and brevis (PB). The peroneus longus originates in the proximal lateral calf and coalesces into a neat cord-like tendon by the distal third of the shin. The tendon then turns sharply anteriorly behind the lateral malleolus and travels anteriorly and plantarly in tendon sheaths anchored to the lateral wall of the calcaneus. The tendon then turns medially and travels a sigmoid path under the cuboid before eventually inserting at the 1st metatarsal and cuneiform.<sup>25</sup> Given this circuitous path, it is not surprising that the muscle has numerous functions. Chiefly, the PL plantar flexes and everts the ankle; however, given its medial insertion, the PL also plantar flexes the 1st metatarsal.<sup>24,25</sup> The PB travels a similar course to the PL but its tendon becomes more tape-like at its bend around the lateral malleolus. The tendon then extends to insert at the base of the 5th metatarsal. The primary functions of the PB are to plantar flex the ankle at the talocrural joint and evert the foot. [Figure 2-11]

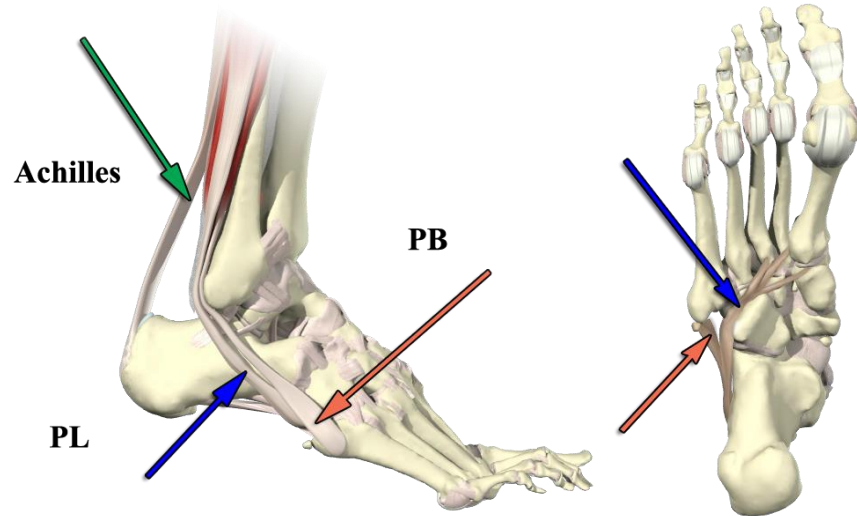


**Figure 2-11: LEFT: Lateral view of a right foot showing evertor tendons. PL (blue); PB (orange); Achilles (an invertor) also shown (green). RIGHT: Plantar view.**

### **3. ADULT ACQUIRED FLATFOOT DEFORMITY**

#### **3.1 CLINICAL PRESENTATION AND DIAGNOSIS**

Adult acquired flatfoot deformity (AAFD) is a chronic disease in which structural changes in the tendons and ligaments supporting the midfoot manifest as a drop in the medial longitudinal arch of the foot along with significant pain and discomfort. The incidence of flatfoot in the adult population is not well established partly due to the unknown prevalence of asymptomatic flatfoot. However, current estimates for symptomatic sufferers range from 2-5% of the adult population.<sup>32,33</sup> Diagnosis of flatfoot in these individuals depends on medical history, gross presentation, and x-ray analysis; though other imaging modalities including MRI, CT, gait analysis, pedobarography, and others are less often used to further characterize the deformity. Medical history associated with adult flatfoot includes childhood flatfoot, family history of adult flatfoot, female, postpartum, and/or post menopause.<sup>33,34</sup> Additionally, activity level, types of footwear, and obesity are known to accompany the disorder. Clinical presentation usually includes some or all of the following: grossly fallen medial longitudinal arch, valgus (outward) tilting of the hindfoot, and abduction of the forefoot relative to the hindfoot. [Figure 3-1] Pain may also be present upon palpation at the medial midfoot along the course and insertion of the PTT, at the talonavicular joint, and at the calcaneal origins of the plantar fascia.

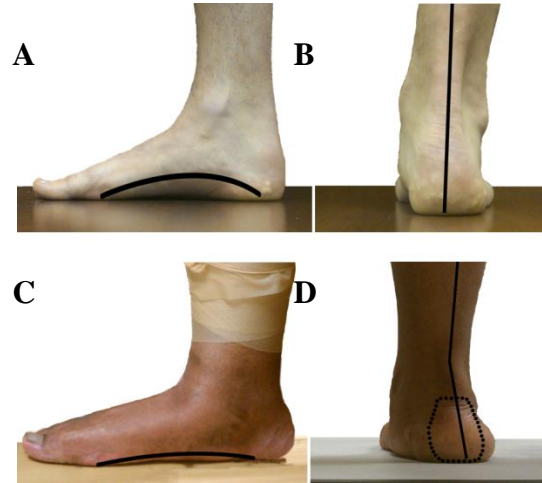


**Figure 3-1: ML (A,C) and PA (B,D) views of a normal foot (top) and an AAFD foot (bottom) from one of the study participants.**

### *3.1.1 Radiographic Evaluation*

Standing plane radiographs are routinely taken in the mediolateral (ML) and standard anteroposterior (AP) planes in order to quantify the joint changes in flatfoot sufferers. Once obtained, bony prominences are used to define axes of the various bones in the foot and to calculate joint angles. While use of these angular measures is more common and generally considered more robust, some investigators have also suggested various linear measurements as sensitive indicators of flatfoot, though technical difficulties associated with scaling and magnification can distort these measures.

In the ML view, the most widely utilized angular measures are the talo-1st metatarsal angle, calcaneal pitch angle, and the talocalcaneal angle.<sup>35-37</sup> [Figure 3-2:A-C] The most widely accepted distance measurements in the ML view are the 1st cuneiform height and the 1st cuneiform to 5th metatarsal distance, though both are generally considered to be inferior to the three angles discussed above.<sup>36-38</sup> [Figure 3-2:D] In AAFD afflicted patients, the talo-1st

metatarsal angle increases while the calcaneal pitch angle, talocalcaneal angle, and linear distances all decrease. Thus all four measures quantify the degree to which the medial longitudinal arch drops under load.

In the AP view, the most widely used angular measures are the talonavicular angle the talo-1st metatarsal angle.<sup>35-37</sup> [Figure 3-3:A,B] More recently, some authors have suggested the talonavicular uncoverage distance, though the robustness of this measure is not well established.<sup>39</sup> [Figure 3-3:C] Here, AAFD patient measures are larger than their unafflicted peers indicating that the forefoot is abducting relative to the hind foot when under load.

In addition to the eight measures described above, subsequent investigators have suggested numerous other radiographic angle and distance measures of AAFD. These include the ML calcaneal-1st metatarsal angle, ML talar declination relative to horizontal, and AP talo-2nd metatarsal angles, as well as the ML heights of the talus, navicular, cuboid, and 1st metatarsal.<sup>36,40-44</sup> To date, these have not been widely incorporated into clinical practice given the lack of supporting literature and unknown reliability. However, future studies may yet confirm their validity, and in so doing, supplant the existing measures.



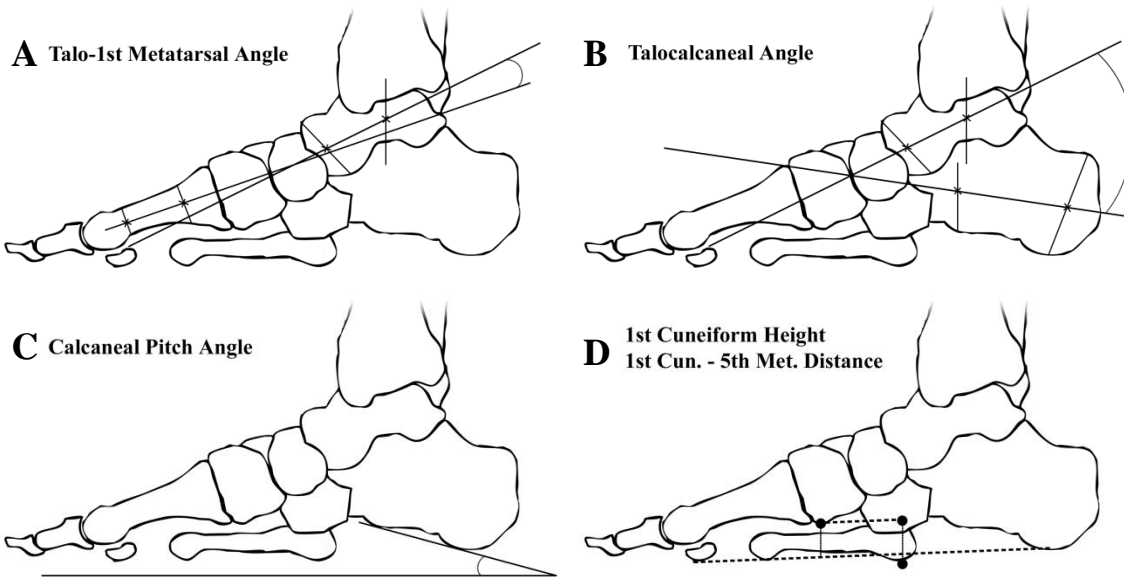


**Figure 3-2: Diagram of most often used AAFD measures in the ML view.**

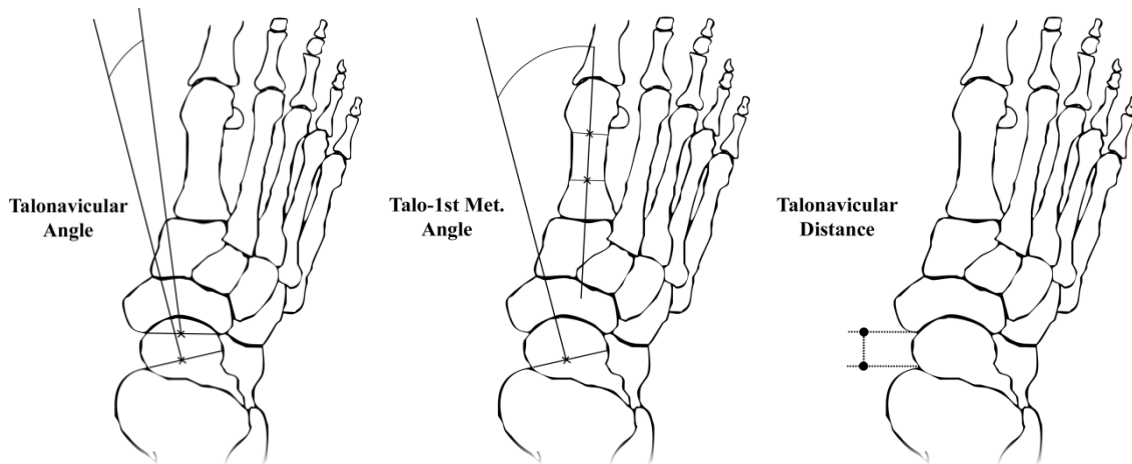


**Figure 3-3: Diagram of the most often used AAFD measures in the AP view.**

### *3.1.2 Soft-Tissue and Kinematic Evaluation*

Numerous investigators have also sought to characterize biomechanical behavior of AAJD patients beyond the angle and distance measures provided by plane radiographs. However, most of these techniques are employed only in non-research settings. Within the scope of the present work, the most relevant of these alternate methodologies are MRI and pedobarography or plantar pressure mapping.

MRI is most often used to investigate changes in tissue quality in the region of the midfoot as AAJD progresses. These tissues include the PTT, the capsule and ligaments supporting the talonavicular joint where the deformity manifests, and the plantar fascia which is often a site of pain in AAJD. Specifically, MRI allows for the visualization and quantification of properties such as fiber alignment, the presence and size of tears and/or fluid retention, and the increased deposition of lipids, fibrocartilage, or bone in the tissues. The relative correlation between these MR signs and AAJD is discussed in greater detail below. [Section 3.2.1-2]

In contrast, pedobarography is most often used to assess changes in kinematics associated with AAJD. Here, ink, plaster, pressure sensitive films, or more recently electronic resistive membranes are used to quantify the relative pressure carried by the sole of the foot. These contour outlines are then segmented into physiologically relevant regions in order to characterize how the load profile changes during activities such as walking or as the deformity progresses. Characteristic changes in plantar loading associated with flatfoot include increased medial metatarsal and hallux loading during stance and the toe-off portion of gait and an increase in the contact area of the medial arch.<sup>37,42,45-47</sup> Though not typically employed in a clinical setting, investigations of these changes in loading help explain the underlying pathomechanics of AAJD.

Furthermore, by analyzing changes in plantar loading both before and after surgical intervention, the success and mechanism of the surgery can be investigated.<sup>48–53</sup>

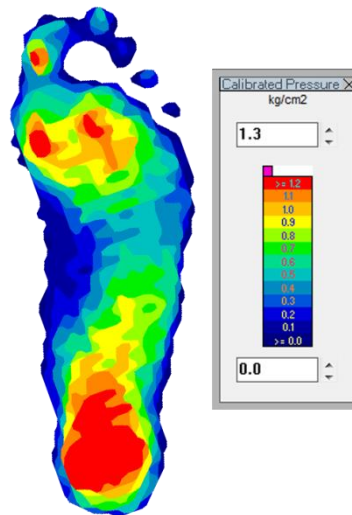


**Figure 3-4: Example of a plantar pressures contour map from one of the diagnosed AAFD patients in the cohort.**

### 3.2 ETIOLOGY

In their seminal 1974 paper, Goldner et al. codified what is the current understanding of AAFD etiology.<sup>54</sup> Here, the authors describe in detail how chronic tenosynovitis around the PTT leads to structural and cystic degeneration of the distal tendon along its course behind the medial malleolus and at its insertion on the navicular. Over time, this mechanical degradation hinders the subtalar inverting ability of the PTT and, if left untreated or aggravated by obesity, labor, or confounding pathologies, gradually shifts the burden of supporting the arch to the passive soft-tissues of the arch. The most often implicated of these are the superomedial and inferomedial spring ligament [plantar calcaneonavicular], the fibers of the deep deltoid ligament [talocalcaneal], and the talocalcaneal interosseous ligaments.<sup>55–57</sup> Though stout, these ligaments

slowly distend and disorganize manifesting as the medial subluxation or 'uncovering' of the talonavicular joint and a plantar/valgus tilt of the calcaneus, ultimately leading to a pronounced drop in the medial arch of the foot. [Figure 3-5] This drop further causes the inversion/eversion axis of the hindfoot to migrate medially under load such that the Achilles line of action becomes everting at the ankle. Finally, the under antagonized everters, e.g. the gastrocnemius/soleus and peronei muscles, contract and reorganize in a shortened state, thus fixing the foot in an overpronated state even when unloaded.<sup>58</sup>



**Figure 3-5: Anterior view of a study patient with AAFD. Note the valgus angulation of the hindfoot and medial splaying of the arch with associated talonavicular uncovering.**

### *3.2.1 Posterior Tibial Tendon Dysfunction*

The relatively hypovascular nature of the distal PTT is thought to be the underlying cause of most PTT disorders including AAFD. Specifically, while the enthesis of the tendon is well supplied with blood at its insertion onto the navicular tuberosity, the portion sitting just posterior to the medial malleolus is subjected to considerable compressive forces. These forces inhibit the diffusion-mediated exchange of nutrients and metabolites, exacerbated by the lack of

mesotendon distally, thus predisposing the tissue region to localized ischemia. In AAFD, this ischemia leads to tendonosis of the PTT from the level of the malleolus to the insertion at the navicular. Continued strain and tissue ischemia then progress to fluid accumulation in the tendon sheath, disorganization of the tendon, lipid deposition, and tears.<sup>56,59,60</sup> Upon inspection with MRI, these changes will typically appear as increased signal (white) along the course of the PTT in tissue that is nominally black in the afflicted patient's scan, as well as a markedly enlarged cross sectional area relative to adjacent tendons.<sup>60</sup> Mechanically, these changes result in a less stiff, more distensible tendon that inefficiently inverts the subtalar joint despite the proper function of the muscle itself, though there is some recent evidence that posterior tibialis muscle function may also be diminished in some AAFD sufferers.<sup>61</sup> EMG studies further suggest that the progression of AAFD will lead to amplification of PTT neuromuscular activity as the body attempts to retain PTT function.<sup>62-64</sup>

### *3.2.2 Ligamentous Changes*

In the intact foot, the passive support structures of the foot are stout collagenous structures with obvious banding and moderately high fiber alignment. On inspection using MRI, they appear as low signal (dark) tissues with minimal midsubstance signal or discontinuity.<sup>29</sup> However, like the PTT, MRI studies of the ligaments of AAFD patients have revealed chronic changes from the intact state.<sup>55-57</sup> Indeed, Deland et al offered a four-tiered grading of eleven soft-tissues in the foot for a cohort of 31 patients (31 feet) with AAFD secondary to PTT insufficiency. These tissues included the (1) PTT; the (2) superomedial and (3) inferomedial bands of the spring ligament; the (4) talocalcaneal interosseous ligaments; the (5) anterior, (6) posterior, and (7) deep deltoid ligaments; the (8) plantar naviculocuneiform ligament; the (9)

plantar cuneometatarsal ligaments; the (10) long and short plantar ligaments; and the (11) plantar fascia. While unable to distinguish the type of structural changes observed for a given tissue, they instead classified the amount of cross section of the tissue observed to have abnormal signal. Thus, their scheme separated intact (Grade 0), increased signal of less than 50% the cross sectional area (Grade I), increased signal greater than 50% (Grade II), partial tear of the structure demonstrated by signal discontinuity of less than 50% (Grade III), and tears greater than 50% (Grade IV). None of the patients in their cohort were observed to have full thickness ruptures in any tissues. They found that in addition to changes in the PTT, the superomedial and inferomedial spring ligament as well as anterior deltoid showed significant signal attenuation in their afflicted cohort, thereby suggesting that, like the PTT, there is a chronic degeneration of the structures of the medial foot in AAFD.<sup>56</sup>

### 3.3 STAGES OF AAFD

The progression of AAFD is functionally staged using the following two clinical tests. The first is the hallux dorsiflexion or 'Jack Test,' wherein the great toe of the weight bearing foot is dorsiflexed to its maximum extent. This action recruits the plantar fascia in order to re-establish the medial arch by means of the windlass mechanism.<sup>65,66</sup> Therefore, a positive Jack Test indicates a flexible or reducible flatfoot deformity.<sup>33,67</sup> The second test is the single leg heel raise. Here, the patient is asked to actively plantar flex at the ankle, bearing their full body weight on the afflicted limb, ultimately rising into maximum ankle plantar flexion with the hindfoot slightly supinated. A negative sign is observed when either significant pain or weakness prevent this action and is indicative of PTT pathology.<sup>34,68-71</sup> In the early stages of the

disease, the patient may be able to partially lift their heel, though the hindfoot will remain in valgus.

Beyond the initial clinical assessment, the first widely accepted classification system of flatfoot secondary to PTT dysfunction was put forth by Johnson and Strom in 1989. The classification incorporates a soft-tissue assessment and initially had just three stages to encompass the entire spectrum of PTT dysfunction, mobility of the hindfoot, pain, and functional weakness. These stages were: peritendonitis of the PTT with mild degeneration (Stage I), mild PTT elongation with a flexibly deformed mid- and hindfoot (Stage II), and PTT elongation with a rigidly deformed mid- and hindfoot (Stage III).<sup>70</sup> Subsequently, numerous authors have sought to further refine the very broad Stage II designation. The current grading scheme based on the works of Johnson and Strom, Myerson, Parsons et al, and Vulcano et al are shown below in Table 3-1.<sup>70-73</sup>

Of particular interest to this work are those patients who are classified as Stage IIb by the grading system outline in Table 3-1. At this level, patients present with a significant and debilitating deformity, but one that remains fully passively correctable.

**Table 3-1: Stages of AAFD**

| <b>Stage</b> | <b>PTT Condition</b>         | <b>Single Leg Heel Raise</b>                           | <b>Deformity</b>   |
|--------------|------------------------------|--|--|
| <b>I</b>     | Peritendinitis, degeneration | Normal, mild weakness                                  | None   |
| <b>IIa</b>   | Functional elongation        | Marked weakness  | Moderate, Flexible. <30% talonavicular uncoverage; <15° resting forefoot supination                      |
| <b>IIb</b>   | Functional elongation        | Inability or marked weakness, hindfoot remains everted | Severe, Flexible. >30% talonavicular uncoverage; >15° resting forefoot supination                        |
| <b>IIc</b>   | Functional elongation        | Inability or marked weakness, hindfoot remains everted | Severe, Flexible. >30% talonavicular uncoverage; >15° resting forefoot supination; not fully correctable |
| <b>III</b>   | Functional elongation        | Inability  | Severe, Rigid deformity. Involvement of talocrural, subtalar, and talonavicular joints.                  |
| <b>IV</b>    | -                            | Inability  | Severe, Rigid deformity not involving talonavicular joint. Ankle deformity.                              |

### 3.4 TREATMENT

In 1884, Ogston wrote of pes planus:

"[T]here are always great changes at the joint between the scaphoid [navicular] and the head of the astralgus [talus]... Here the relaxation is very great, so that by acting on this joint alone we can... rectify the faulty position of the foot." <sup>74</sup>

This view of the talonavicular joint as the principle source of flatfoot deformity has been largely validated by modern biomechanical research yet the question of what is the best course of



treatment for flatfoot has proved to be contentious even in contemporary orthopaedic practice. Likely underlying many disagreements concerning treatment is the fact that despite early recognition of the locus of the deformity, the first well substantiated classification system for flatfoot was not realized until Johnson and Strom's work in 1989.<sup>70</sup> Any discussion of treatment must therefore be done in the context of the disease's stage.

Conservative treatment is indicated as a first course of action for all early stage AAFD sufferers and as a first option for all flexibly deformed later staged patients. As early as 1888, Whitman proposed what can be considered one of the earliest orthotics specifically designed for the treatment of flatfoot. In his writing, Whitman describes taking a plaster cast of the patient's foot. His insight, however, was to have the patient supine (non-weight bearing) and manually manipulate the foot into subtalar neutral. The resulting casts were then used to create stiff, arch length steel plates which were then worn inside the shoes.<sup>75</sup> For modern patients, orthotics very similar to those proposed by Whitman are the foundation of conservative, non-surgical treatment of AAFD. Additional conservative treatment options include physical therapy to strengthen the posterior compartment muscles, namely the PTT, weight loss, and lifestyle changes in order to reduce the amount of time walking.

For patients that fail conservative treatment, surgical corrective is indicated. Perhaps the earliest successful surgical intervention may be again attributed to Professor Ogston who described what would be today considered the single and double arthrodesis of the talonavicular and talocalcaneal joints. Here, Ogston recounts that his purpose was

"...to denude as much of the cartilaginous surfaces of the astragalo-scapoid [talonavicular] joint as can conveniently be reached, to place the foot in the proper position, and secure its immobility by uniting the two bones by ivory pegs." <sup>74</sup>

Clearly ahead of its time, this treatment is still routinely performed today. Yet, while the contemporary surgeon may ultimately choose tarsal fusion to address chronic deformity, this approach is most often relegated to the end stages of AAFD where the deformity has become rigid and no longer passively correctable.<sup>76</sup>

For AAFD sufferers diagnosed as Stage IIb there is general consensus on the appropriate surgical route. Indeed, in a survey of 104 orthopaedic foot and ankle surgeons, Hiller and Pinney reported that 98% would perform a PTT augmentation through either a FDL (89%) or FHL (9%) tendon transfer combined with 73% reporting they would include a medializing calcaneal osteotomy (MCO). These responses corresponded to a plurality of surgeons (38%) performing an MCO with PTT augmentation.<sup>77</sup>

### *3.4.1 Tendon Transfer as PTT Augmentation*

As the responses to the Hiller and Pinney survey demonstrate, the distal tendon transfer is the most utilized soft-tissue reconstruction used in the treatment of Stage II AAFD. The biomechanical basis of this procedure is that by affixing a healthy muscle and tendon at the insertion of the deficient PTT, more normal subtalar inversion force can be restored. The two available flexor tendons in the medial compartment of the ankle are the FDL and the FHL and are activated through similar neuromuscular pathways as the PTT.<sup>54,69,78</sup> Both donors have yielded satisfactory clinical results in several reports.<sup>54,69,70,79,80</sup> Though, increasingly the FHL has gained in popularity as the preferred donor tendon given that anatomic analyses have shown

the physiologic cross-sectional area (PCSA), and thus the inversion torque, of the FHL to be twice that of the FDL.<sup>71,81-83</sup> Indeed, in an independent study by Murray et al, the maximum potential torque supplied by the PTT was 52 kg-cm acting against a maximum potential torque of the peroneus brevis of 38.5 kg-cm. For the AAFD patient, a FHL tendon transfer could impart a potential maximum torque of 40.4 kg-cm versus just 25.1 kg-cm for the FDL.<sup>84</sup> Thus, given these two donor options, the FHL may better compensate for lost PTT function and act antagonistically to the peroneus brevis.

When transferring either donor, the tendon is transected in the forefoot distal to the Knot of Henry at the crossing of the FHL and FDL just plantar to the naviculo-1st cuneiform joint. The loose end is then passed dorsally through a bony tunnel drilled in the navicular tuberosity. Subsequently, the foot is manipulated into full plantar flexion and an inverted position before the passed tendon is sutured to the PTT insertion on the navicular or looped back onto itself.

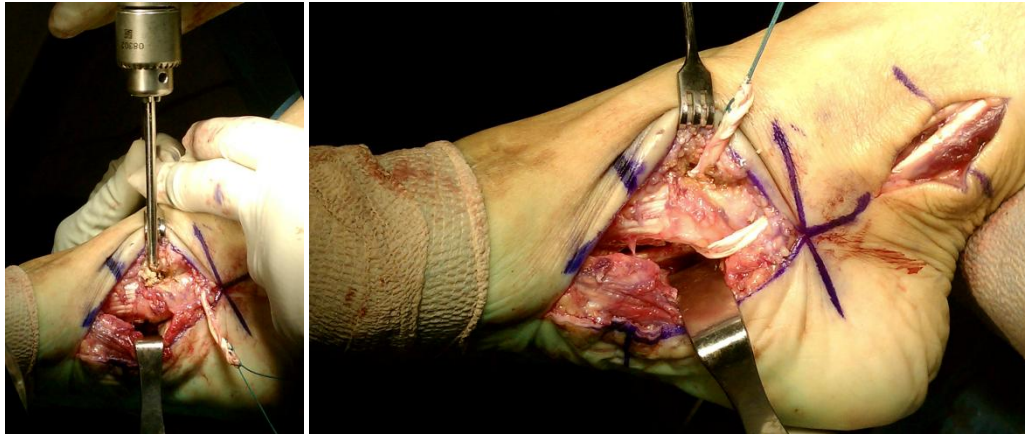


**Figure 3-6: Medial intraoperative view of FHL tendon transfer to bolster the PTT in one of the study patients. LEFT: Dorsoplantar tunnel drilled through the navicular. RIGHT: Anchoring of the transferred FHL in the navicular.**

With either tendon transfer, clinical and in vitro studies have demonstrated loss of flexion force in the toes of the transferred tendon but have not determined if this loss is clinically significant.<sup>50,53,85-87</sup> A tenodesis of the distal stump of the FDL or FHL tendon has been promoted to counter the loss but remains controversial.<sup>71,80,83,88</sup> With tenodesis there is increased risk to the surrounding neurovascular structures in the arch of the foot, namely the medial proper digital artery and nerve and the common digital arteries and nerves in the first and second webspaces.<sup>89</sup> Additionally, some clinicians dispute the necessity of tenodesis given some reports of consistent and substantive interconnections between the FHL and FDL distal to the typical transection level.<sup>25,71,83,89,90</sup>

Functionally, both FHL and FDL transfers cause an increase in plantar force measured under the metatarsal heads, though distal tenodesis tends to constrain this loading to the medial forefoot in the case of FHL transfers.<sup>50</sup> Neither transfer alone can correct the gross or

radiographic deformity associated with AAFD and thus other bony procedures are typically employed.<sup>71,79,88</sup>

### 3.4.2 *Medializing Calcaneal Osteotomy*

Of the candidate bony procedures to correct flatfoot deformity, the medializing calcaneal (MCO) or 'slide' osteotomy is the most common. Briefly, this procedure involves splitting the body of the calcaneus, including the Achilles insertions on the calcaneal tuberosity, from the anterior portions of the bone along a cut plane roughly orthogonal to the long axis of the calcaneus. This posterior fragment is then translated medially to the extent that taught soft-tissues of the sole of the foot permit; typically, this is 5-10mm.<sup>48</sup> This translation is designed to primarily address two underlying causes of AAFD. First, by moving the contacting portion of the calcaneus medially, the hindfoot valgus associated with AAFD is removed.<sup>48,49,91</sup> Second, the medial shift of the Achilles tendon insertion causes the previously everting gastrocnemius/soleus complex to subsequently invert the subtalar joint, thereby antagonizing the peronei muscles. The combined effects of addressing these two biomechanical factors is that the medial longitudinal arch is unloaded, leading to decreased forefoot abduction and increased talonavicular coverage.<sup>78,92,93</sup> An unfortunate side effect of the MCO is that with the correction of the forefoot abduction comes an increase in lateral forefoot plantar force. While AAFD sufferers do have typically higher medial metatarsal loading, and this shift ameliorates that somewhat, some clinicians and researchers have noted increased incidence of lateral column pain and early onset calcaneocuboid osteoarthritis with this shift in load, though the most serious reports reflect MCO in combination with other lateral column procedures.<sup>48,49,52</sup>

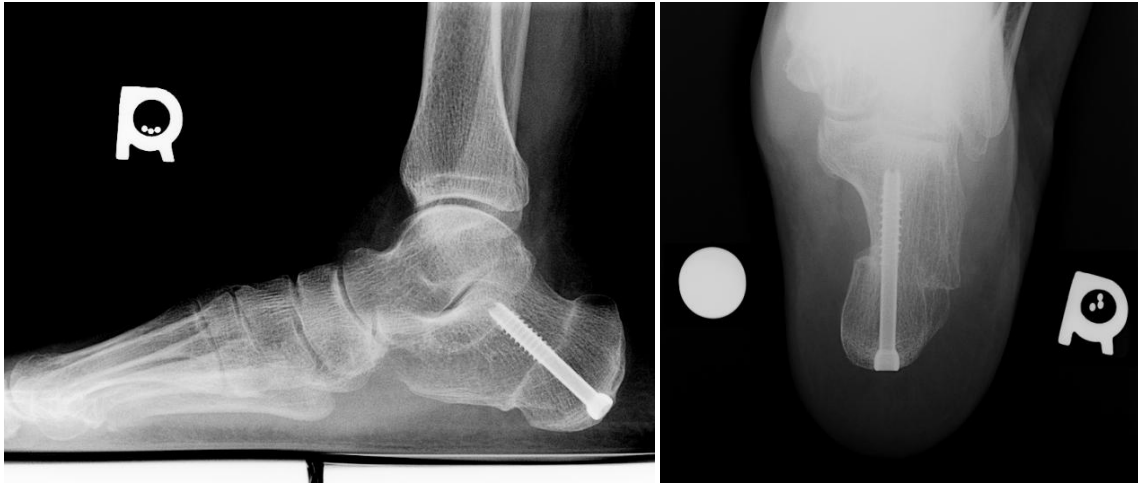


**Figure 3-7: Radiographs of MCO on a right foot. LEFT: ML view showing a single cancellous bone screw. RIGHT: Saltzman view of the transected calcaneus.**

## **4. STUDY DESIGN AND DATA ACQUISITION**

### **4.1 PATIENT RECRUITMENT**

With Institutional Review Board (IRB) approval, candidate flatfoot patients with scheduled surgeries for the treatment of clinically diagnosed AAJD were identified from the VCU Department of Orthopaedic Surgery by the collaborating surgeon, Dr. Robert S. Adelaar. These prospective patients were approached with a study flyer [APPENDIX D] and informed regarding the purpose, risk, and benefits of the study as outlined in the VCU IRB consent form. [APPENDIX E] In total, six women (aged 26-69 years, average 50years; body mass index 27.3-38.5, average 32.2) gave consent and were recruited to participate in the study. All six patients were clinically graded preoperatively as Stage IIb by the attending surgeon (RSA) indicating "flexible hindfoot deformity."<sup>70</sup> The patients further showed gross collapse of the medial arch and excessive forefoot abduction as well as an inability to perform single-leg heel raises; a ubiquitous functional test of the inverting power of the PTT.

Of these six patients, five were reevaluated postoperatively after being released from care by the attending surgeon (RSA) at a mean follow-up period of 12.9 months (range 12-15 months). One patient (#2) was lost to follow up. The preoperative and postoperative mean body mass index (BMI) of this cohort were 32.2 (range 27.3-38.5) and 34.0 (range 28.0-38.4), respectively.

## 4.2 X-RAY

With guidance from the VCU Department of Radiology, study patients were evaluated prior to surgery using hindfoot photographs, plane film radiographs, and MRI. Photographs were focused on the calcaneal tuberosity during single-leg stance to examine hindfoot valgus. Two radiographs of the foot were taken with the patient positioned in single-leg stance: a standard mediolateral (ML) (sagittal) view and the standard anteroposterior (AP) view wherein the x-ray emitter was angled obliquely anterior approximately 30° from the dorsoplantar direction focused at the navicular. [Figure 4-1;A,B]



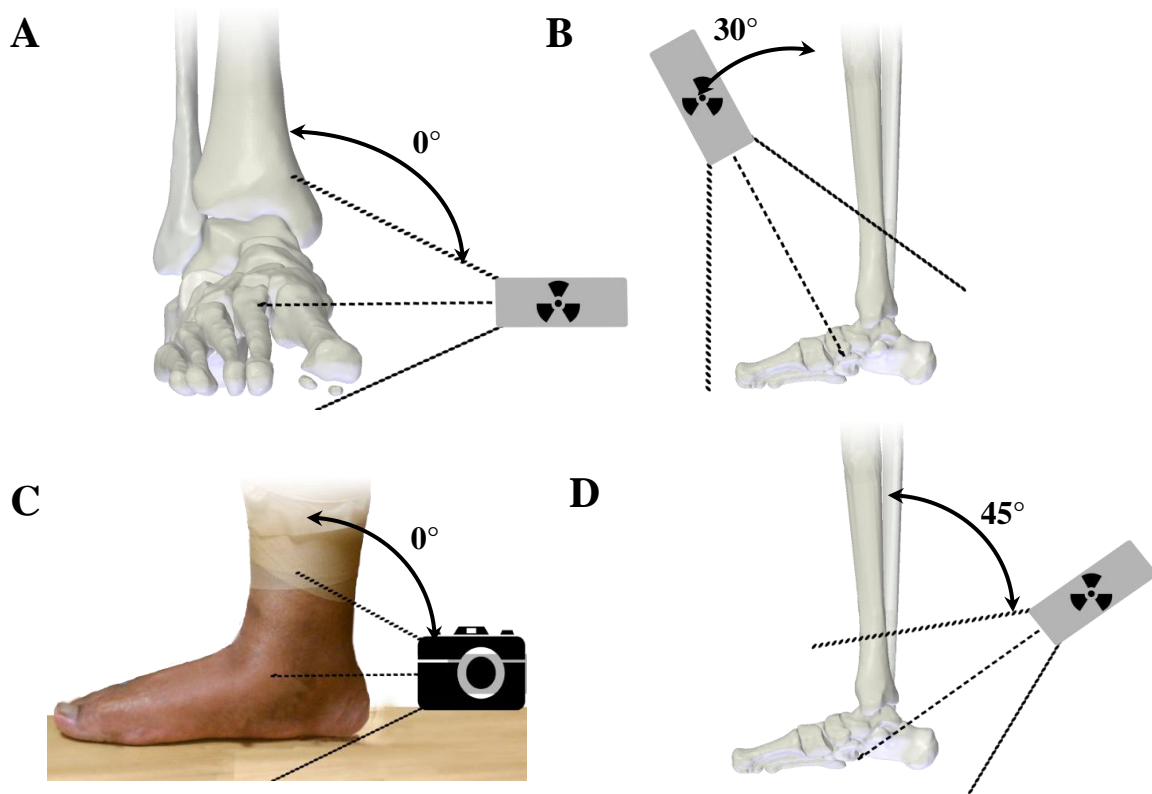


**Figure 4-1: Diagrams of the three x-rays taken for each patient. (A) Emitter position for ML view; (B) Emitter position for standard AP view; (C) Camera position for hindfoot view; (D) Emitter position for Saltzman view (PostOp. only).**

Postoperatively, the patients were again imaged using hindfoot photographs, ML and standard AP radiographs. Additionally, a revised Saltzman view radiograph was taken, wherein the emitter was angled obliquely posterior approximately 45° from the dorsoplantar direction focused at the subtalar joint.<sup>94</sup> [Figure 4-1;C] This third view was incorporated to supplement the postoperative ML radiograph in the quantification of the patient MCO. A nickel was placed in the field of view at the lateral margin of the surgical scar in order to calibrate the measurements and correct for any image distortion.

### 4.3 PLANTAR FORCE MEASUREMENTS

In order to assess the effect of surgical correction on plantar force distribution, plantar force measurements were recorded for each patient pre- and postoperatively using the HR Mat system Model 7101 E (TekScan, Boston, MA). For quiet stance data, patients were asked to stand barefoot on the recording mat for twenty seconds. The patients were then allowed to equilibrate themselves for ten seconds and after which force data was logged for ten seconds. Both two-leg and single-leg stance trials were recorded and patients were offered a chair back for balance if they desired. Once recorded, the plantar force contours were segmented into three regions; medial forefoot, lateral forefoot, and hindfoot in order to investigate course plantar load shifts following surgery. This segmenting is described in detail in Section 8.2.1.

While the scope of this work only considers the force distribution during stance, a companion thesis authored by Erika A. Matheis, M.S. analyzed the surgical effects in a more refined nine region plantar map during one and two foot stance, as well as during walking.<sup>95</sup>

### 4.4 MAGNETIC RESONANCE IMAGING (MRI)

In addition to radiographs, a protocol of five MRI sequences was developed in order to fully visualize the patients' anatomy. The first three were chosen to allow further scrutinization of the collagenous soft-tissues implicated in AAFD. These were a [1] transverse T2-weighted turbo spin echo (TSE) sequence with fat-suppression, [2] a transverse T1-weighted TSE sequence, and [3] a T1-weighted fluid suppressed turbo inversion recovery (TIRM) sequence. The final two were chosen based on their ability to capture the bony anatomy of the lower limb; these were [4] a T1-weighted TSE with fat suppression focused on the entire length of the tibia and fibula and [5] a sagittally sectioned dual echo steady state (DESS) sequence. [Table 4-1]

The DESS sequence was chosen as the most appropriate for delimiting articular margins of the bones in the foot and ankle given its high signal intensity for articular cartilage and low fluid and fat signals.<sup>96</sup> All sequences were captured using a 1.5 T MRI scanner (GE Healthcare Technologies, Waukesha, WI).

**Table 4-1: MRI sequence acquisition parameters.**

|                           |      | Sequence                 | Signal Bias | Scan Bias  | X (mm) | Y (mm) | Z (mm) | FOV (mm <sup>2</sup> ) | Image size (pixels) | # of Images |
|---------------------------|------|--------------------------|-------------|------------|--------|--------|--------|------------------------|---------------------|-------------|
| <b>Foot &amp; Ankle</b>   | T2   | Turbo Spin Echo          | Fat supp.   | Transverse | 0.6    | 0.6    | 3.0    | 180 x 180              | 256 x 218           | 32          |
|                           | T1   | Turbo Spin Echo          | -           | Transverse | 0.6    | 0.6    | 3.0    | 180 x 180              | 256 x 205           | 32          |
|                           | T1   | Turbo Inversion Recovery | Fluid supp. | Sagittal   | 3.0    | 0.3    | 0.3    | 200 x 200              | 256 x 215           | 20          |
|                           | DESS | Dual Echo Steady State   | -           | Sagittal   | 0.7    | 0.7    | 0.7    | 200 x 200              | 256 x 256           | 104         |
| <b>Tibia &amp; Fibula</b> | T1 † | Turbo Spin Echo          | Fat supp.   | Sagittal   | 4.0    | 0.8    | 0.8    | 380 x 380              | 256 x 205           | 29          |

† = Imaging from the tibial plateau to the subtalar joint. Did not use extremity coil.

In order to standardize the imaging protocol before recruiting live patients, a single fresh frozen left lower extremity (age, 58years), disarticulated at the knee, and free from any obvious deformity was scanned using these MRI sequences. The appendage was affixed to a purpose-built fiber board jig that allowed the ankle to be taped in neutral plantar / dorsiflexion and subtalar neutral. The appendage and jig were then positioned on the movable MRI table with the long axis of the tibia roughly aligned with the cylindrical axis of the MRI coil. A localizing "extremity coil" was placed around the appendage and jig with the toes allowed to extend just

out of the center of the coil as shown in Figure 4-2. The appendage was scanned using various settings for acquisition time, field of view, and sagittal slice thickness, until an optimum balance was determined; these are given in Table 4-1. Settings on the first three scans were left to the discretion of the radiologist, while the DESS sequence parameters were set to the scanner's minimum pixel size, minimum slice thickness, and condition of voxel isometricity. The DESS sequence thus had a voxel size of  $0.7\text{mm}^3$  and required an average of 13-14 minutes to capture.



**Figure 4-2: Cadaveric left lower extremity taped onto the imaging jig and positioned in the MRI extremity coil.**

Once live patients were recruited to participate in the study, each was imaged preoperatively using the same 1.5T MRI scanner and sequences as used on the cadaveric appendage. The only significant alteration made to the imaging protocol was the use of stiff foam pillows to wedge the participants' feet within the extremity coil in place of the fiber board jig and tape used during the cadaveric appendage scans. Subsequent low resolution 'localizer' scans were then used to verify neutral plantar / dorsiflexion and subtalar neutral alignment before high resolution image acquisition.

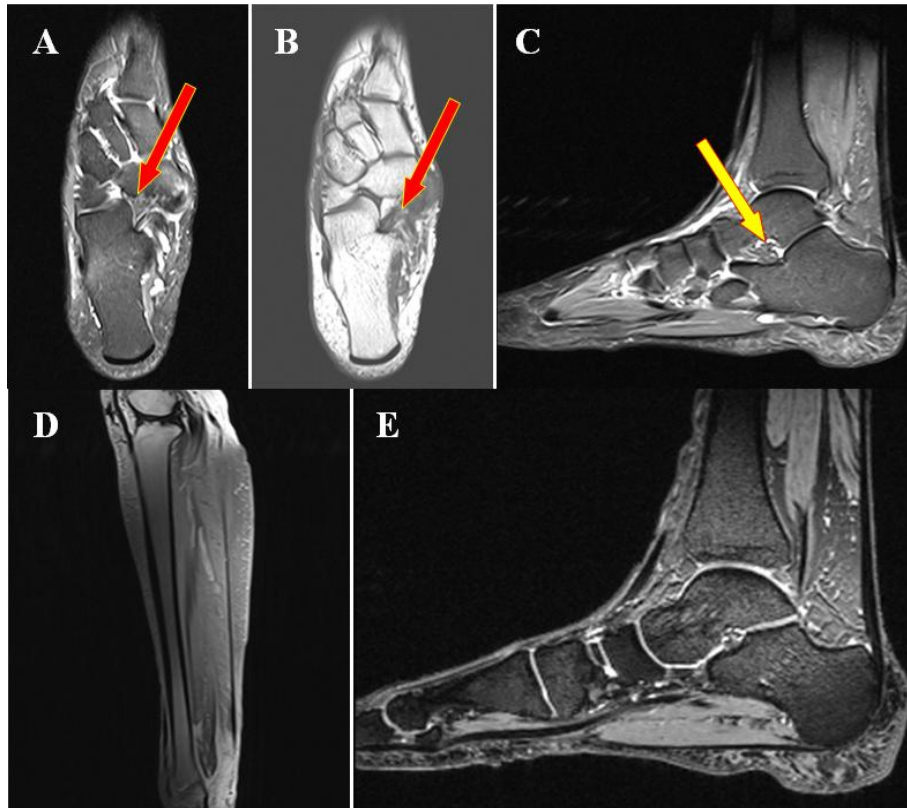


**Figure 4-3: Typical images for each of the five MRI sequences used. [A]: Transverse T2 TSE showing spring ligament (red arrow); [B]: transverse T1 TSE showing spring ligament (red arrow); [C]: sagittal T1 TIRM showing the talocalcaneal interosseous ligaments (yellow arrow); [D]: sagittal T1 TSE showing the distal leg; [E]: sagittal DESS scan with maximum resolution and higher cartilage signal.**

#### *4.4.1 Tissue Attenuation*

Dr. Curtis W. Hayes, the collaborating radiologist with expertise in AAFD, assessed the quality of eight soft-tissues most implicated in Stage II flatfoot and readily visualized with MR.

<sup>55,56,97</sup> These were the (1) PTT, (2) superomedial and (3) inferomedial bands of the spring

ligament, (4) anterior, (5) posterior, and (6) deep bands of the deltoid ligament, the (7) talocalcaneal interosseous ligaments, and (8) plantar fascia. Damage to these tissues was graded in accordance with a modified four-tier scale initially proposed by Deland et al. and given in Table 4-2.<sup>56</sup> The observed values for each of the tissues in given in Table 4-3.

**Table 4-2: Four-tiered grading scale of investigated soft-tissues.**

|             |   |
|-------------|---|
| <b>0:</b>   | Normal/Intact   |
| <b>I:</b>   | Signal attenuation without any (likely) macroscopic tears           |
| <b>II:</b>  | Signal attenuation with likely tears, but <50% tissue cross-section |
| <b>III:</b> | Signal attenuation with tears >50% tissue cross-section             |

**Table 4-3: Observed patient values for the four-tiered grading of the MRI signal attenuation. "NV" indicates the tissue could not be visualized.**

| <b>Tissue</b>                       | <b>Patient #</b> |          |          |          |          |          |
|-------------------------------------|------------------|----------|----------|----------|----------|----------|
|                                     | <b>1</b>         | <b>2</b> | <b>3</b> | <b>4</b> | <b>5</b> | <b>6</b> |
| Posterior Tibialis Tendon           | 1                | 2        | 2        | NV       | 1        | 2        |
| Superior Medial Spring Ligament     | 1                | 2        | 3        | NV       | 1        | 1        |
| Inferior Medial Spring Ligament     | 0                | 3        | 2        | 0        | 2        | 1        |
| Anterior Deltoid Ligament           | 1                | 2        | 3        | NV       | 2        | 2        |
| Posterior Deltoid Ligament          | 0                | 2        | 2        | 0        | 2        | 1        |
| Deep Deltoid Ligament               | 0                | 2        | 0        | 0        | 1        | 1        |
| Talocalcaneal Interosseous Ligament | 0                | 2        | 2        | 0        | 2        | 0        |
| Plantar Fascia                      | 1                | 2        | 1        | 0        | 0        | 1        |

#### 4.5 STUDY OBJECTIVES

The overall objective of this work was to gain a better understanding of the biomechanics underlying Adult Acquired Flatfoot Deformity through analysis of the kinematics of the symptomatic flatfoot. These data were collected through both analysis of in vivo patient x-rays and pedobarography, as well as computational rigid-body predictions of bone, ligament, and muscular behavior. Thus, our specific aims were:

- (1) To analyze the radiographic behavior of each patients' foot and ankle complex during single-leg stance both pre- and postoperatively and to further analyze the radiographic effect of surgical correction by FHL transfer and MCO.
- (2) To create patient-specific rigid-body computational models for each patient enrolled in the study using 3-D geometry extracted from each respective high resolution MRI scan and loaded according to physiologically accurate body weight, extrinsic muscle, and ligament loads. Once created, to validate each model against its respective patient x-rays.
- (3) To model the patient-specific surgical correction and predict operative changes for each patient and to compare these predictions against the patient x-rays to assess the models' accuracy. To further investigate changes in ligament strain and articular contact force to better elucidate the mechanism of flatfoot repair.
- (4) To use the infinitely adjustable nature of parametric modeling to vary the degree of surgical correction and separate the contributions of the tendon transfer and MCO on foot kinematics.

- (5) Finally, to suggest future modeling refinements, with the ultimate goal of using rigid-body modeling for prospective surgical planning.



## 5. MODEL CREATION

### 5.1 OVERVIEW

In order to replicate patient kinematics with a rigid body model, the bony architecture of the lower leg, ankle, and foot of each patient needed to be faithfully reproduced in the computer design space. This has been a common requirement of all rigid-body models created by our laboratory given the driving effect that underlying bony structure has on all aspects of joint function.<sup>5,7,98–102</sup> Furthermore, the small bone size and numerous highly congruous articulations within the foot and ankle depend on this faithful reproduction more so than any other joint complex in the body save for the wrist. However, unlike previous modeling efforts in our laboratory, the added goal of scrutinizing the quality of patient-specific soft-tissues associated with AAFD precluded the use of computed tomography (CT) as an imaging modality, given its relatively poor performance differentiating soft-tissues. As a consequence, magnetic resonance imaging (MRI) was chosen as the ideal modality to both capture the bony geometry of the foot and ankle, but also to provide a means by which the quality of soft-tissue support structures could be evaluated.

## 5.2 MASK CREATION AND THRESHOLDING

In order to extract the bony geometry for each patient, the six preoperative DESS MRI scans were each individually loaded into the medical imaging software MIMICS<sup>®</sup> (v12.0, Materialise's Interactive Medical Imaging Control System, Materialise, Ann Arbor MI). Herein, the MRI scanner sequences were ultimately transformed from the arrayed stacks of 2-D DICOM (Digital Imaging and Communications in Medicine) images into tessellated 3-D bodies. The general workflow for extracting these geometries was as follows. First, the DICOM image stacks representing the DESS scan were imported into MIMICS from the VCU Department of Radiology provided media with the MRI scanner relative coordinate system intact. This was done using the manual import tool within MIMICS and allowed a 1:1 mapping of each image pixel between the two programs; no reduction in resolution, filtering, or offsetting was used. These image stacks were then coarsely cropped such that patients' tissue was closely bound by the limits of the workspace.

Next, sets of selection rules known as "masks" were created wherein each pixel on each image slice was designated either active (bright) or inactive (dark) corresponding to a desired region of interest, e.g. a single bone.<sup>103</sup> In previous modeling work that relied on CT, this grayscale value depended on the Hounsfield Unit (HU) of the pixel and corresponded directly to the radiopacity of the tissue and was relatively specific. However, because the current work relied on MRI, similar grayscale values were often shared by disparate tissue types and thus the threshold value was selected and dynamically updated by inspection. In general, the values used to identify bone ranged from approximately -850 to -1000 HU for the DESS scans.

For each patient scan, variable numbers of masks were created, but generally there were around thirty. These were typically a 'whole scan' mask that coarsely selected all the bony tissue, a 'whole cropped' that windowed the mask to just bound the bony portions of the foot, and then at least

two masks (before and after scaling) for each of the 14 discrete bones of the foot, excluding the phalanges. An example of these masks is shown in Figure 5-1. Additionally, the same process was used to extract the bony geometry for the entire length of the tibia and fibula from the coarser T1 TSE scans that were later incorporated into the models order to represent the whole lower leg.

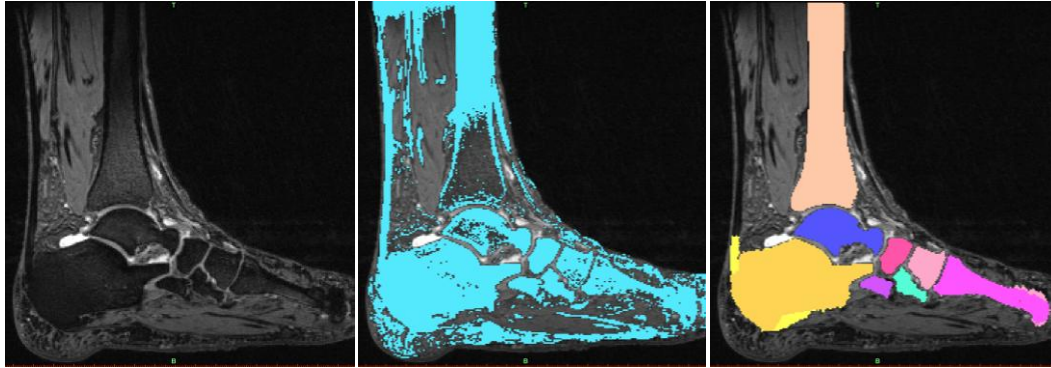


**Figure 5-1: Example of masks created to isolate bones from the DESS scans. LEFT: the unmasked DESS scan with bone demonstrating low signal (dark); MIDDLE: the initial mask with extracorporeal noise removed; RIGHT: 14 discrete masks for each of the bones in the foot, excluding the phalanges.**

### 5.3 PREPROCESSING

The MRI sequences used to scan each participant gave very high resolution images of the bones of the foot and ankle such that articular margins were obvious to the trained eye. However, because MRI signal intensity (brightness) is related to a number of factors that may be shared across tissues, e.g. water content or cell-level alignment, each DESS scan required extensive manipulation using automatic and manual tools in order to separate bones from soft-tissues in cases when their HU

threshold values were similar, i.e. they were the same shade of gray. These manipulations involved a number of tools native to the MIMICS package as described below.

### *5.3.1 Morphology Operations*

The first and most coarse mask adjustment were made using the "region-growing" and "crop" tools. The region-growing tool was used to duplicate a mask wherein only those selected pixels that bordered another selected pixel were preserved. In this way, single pixel or speckled noise was eliminated while preserving contiguous regions of bone. Subsequently, the newly filtered mask was separating into 14 additional masks with one mask per bone within the foot, excluding the phalanges, using the crop tool which simply windowed the selected pixels around a selected volume. Following these coarse adjustments, each bone was then meticulously filled using the "flood-fill" tool wherein the center of a bony region was selected and the selection would grow outwards into like-colored pixels based on the total mouse travel, with dissimilar shaded cartilage surfaces providing a boundary to the filled area.<sup>103</sup> Finally, each bony mask required extensive manual editing along its articular surface using a simple paintbrush-like tool in order to fill in surface gaps and irregularities. These steps were repeated across the 100+ image slices in each DESS scan for all 14 bones modeled, and for all six patients.

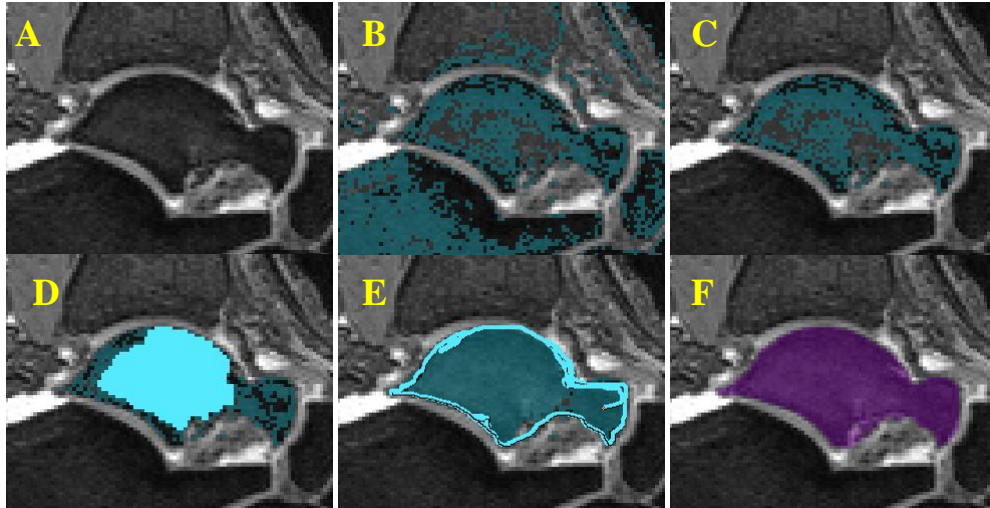


**Figure 5-2: Typical workflow for masking an individual bone (talus) from the (A) initial image through (B) thresholding, (C) region-growing and cropping, (D) flood-filling, (E) manual editing, to (F) the final mask.**

With the masks for all modeled bones created and based on previous modeling experiences, it was apparent that the interarticular distance between bones was sufficiently large to cause significant laxity to develop in the capsular and ligament elements (Ch. 6.6 - Ligament ) once the models were allowed to equilibrate under load. Therefore, it was decided that a scaling factor should be used to preserve the relative distances between bone centroids while maintaining joint congruity. The scaling was implemented at the mask level using the "dilate" tool within MIMICS.<sup>103</sup> Here, each bone mask was uniformly expanded to the eight adjoining unselected pixels in a given slice image. This had the effect of growing the bones by a single pixel (0.7mm) in all directions unless doing so with cause interference with another mask. Thus, since the interarticular space was 2-3 pixels thick for most areas of the foot, the scaling effectively closed the gap between bones while preserving the bony shape throughout. [Figure

5-3] Importantly, because all bones received the same scaling factor, the relative sizes of all bones was preserved.

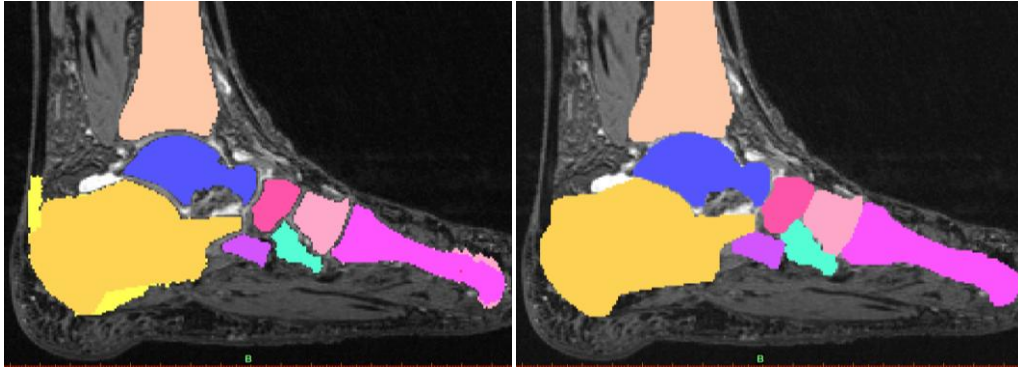


**Figure 5-3: Example of (LEFT) before and (RIGHT) after scaling the masks of all modeled bones using the "dilate" tool. Scaling resulted in a 0.7mm expansion in all directions. Note the reduction in interarticular space around the talus (blue).**

The final step in preparing each bone mask was to use the "smooth mask" tool which reduced surface irregularities between adjacent slices of a given mask. Similar in effect to the "erode" tool described earlier, this function ensured physiologic contours between slices, i.e. in the spaces not directly imaged by the MRI.

#### 5.4 STEREOLITHOGRAPHY (STL) FILES

Once all bones of the foot and ankle were represented by finalized masks, solid bodies were created using the 3-Matic plug-in native to MIMICS. This toolbox allowed the space between sequential slice images to be interpolated orthogonal to the imaging plane. These 3-D volume meshes are known as stereolithography (STL) files and are widely used in CAD packages as they offer excellent 3-D fidelity in a numerically simple and relatively small file format. Specifically,

each resulting tessellated body was described by a continuous mesh of right isosceles triangles, each of which is completely described by four sets of Cartesian coordinates, three to describe the triangles vertices and a fourth describing the outward end of a unit normal to the triangle.<sup>104</sup>

The mesh is created from the underlying highlighted pixels within each mask such that the coordinates for any given triangle vertex are located at the centroid of adjacent highlighted pixels. Triangular vertices on adjacent slices are then linearly interpolated to create volumetric meshes. As a consequence of enforcing isovolumetricity in the MRI scan parameters, the initial edge length of every triangular facet was 0.7mm in the coronal, sagittal, and transverse planes. As a final check to ensure that nothing outside of the intended bony surface was created, the "shell reduction" tool was used. This function acts as a filter that retains only the single (user-defined) largest volumetric body(ies), discarding any small noise related artifacts that may still be present in the mask. An example schematic illustrating how MIMICS creates tessellated surfaces from the bony masks is given in Figure 5-4.

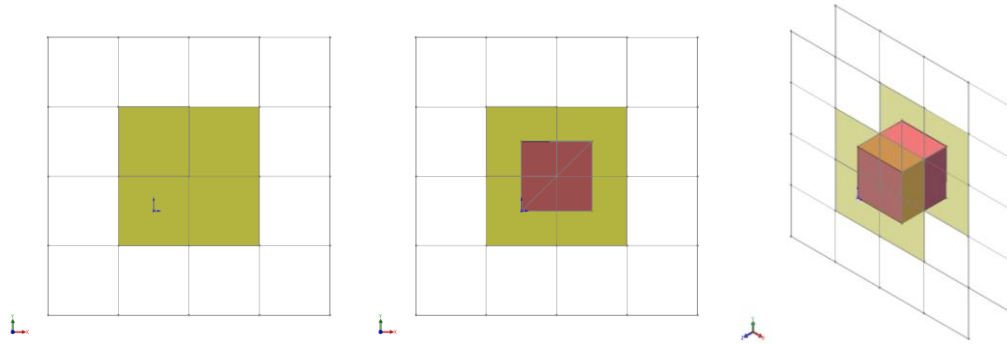


**Figure 5-4: Representation of how masks are tessellated. (LEFT) An array of 16 pixels with the center four selected. (MIDDLE) The centroids of adjacent selected pixels are connected to create complementary right isosceles triangles. (RIGHT) Triangle vertices on adjacent slices are linearly interpolated to define the body volume between slices.**

#### 5.4.1 Mesh Quality

Through the meshing process, the bony masks from each patient were transformed into 3-D STL solid bodies. In total, there were 16 bodies created for each patient: 14 high resolution bones in the foot derived from the DESS sequence scans and two somewhat coarser models of the tibia and fibula created from the T1 TSE scan. However, despite the sub millimeter resolution of the MRI image files, each body was nonetheless sharply and unphysiologically faceted, especially in areas of high curvature such as the articular surface. Thus, following tessellation, each bony solid body was further refined using a number of surface modification techniques described below. The quality of the manipulated meshes was analyzed according to the "R-in / R-out shape quality measure" native to 3-Matic. Herein, the mesh tetrahedral elements, i.e. the volumetric triangles, were graded according to the ratio of the radius of the largest inscribed sphere to the radius of the smallest ascribed sphere. For an ideal mesh comprised of uniformly sized equilateral triangles, this ratio is  $\sqrt{3}:3$ . The



parameter was normalized such that a mesh of equilateral triangles would have an R-in/R-out value of 1.<sup>104</sup> An example of this shape measure is given in Figure 5-5.

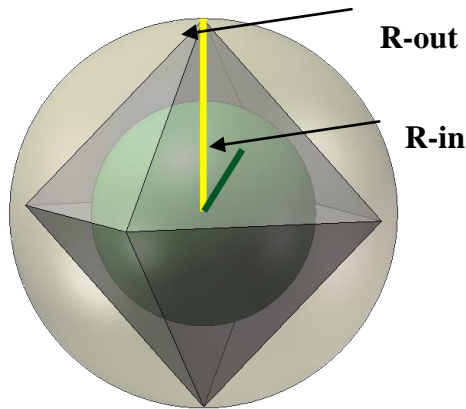


**Figure 5-5: Example of the R-in/R-out shape quality metric demonstrated on an ideal tetrahedron with sides of equilateral triangles. The inscribing sphere radius (R-in) is shown in green; the ascribing sphere radius (R-out) is shown in yellow.**

#### 5.4.2 *Smoothing*

The first step in improving the initial mesh quality was through smoothing. To do this, the "smoothing" tool native to MIMICS was used. This function uses the equipotential method to solve a 2nd order Laplacian equation where the initial vertices ( $v_i$ ) are provided by the pixel coordinates from the MRI scanner. These vertices are then iteratively moved to in order to create even nodal spacing while still maintaining the mesh continuity. This was done by weighting the validity of any new vertex ( $v^*$ ) position relative to the positions of all adjacent

vertices ( $v_k$ ) with Cartesian coordinates of  $v_k = \{x_i, y_i, z_i\}$ .<sup>104-106</sup> For triangular meshes, this equates to six adjacent triangles and the weighting functions become:

$$\sum_{i=1}^6 W_i(x_i - x) = 0 \quad (1)$$

$$\sum_{i=1}^6 W_i(y_i - y) = 0 \quad (2)$$

$$\sum_{i=1}^6 W_i(z_i - z) = 0 \quad (3)$$

The influence that each adjacent vertex has on  $v^*$  is dictated by the "Smoothing-Factor." The 3-Matic program allows values from 0-1 for this parameter where one indicates that the new vertex will be evenly spaced between the existing vertices irrespective of the original position of  $v^*$  and zero indicates that  $v^*$  should not be moved at all. For all STL meshes created, a smoothing factor of 0.7 was used.<sup>104</sup> These weighting equations were then iterated throughout the entire mesh according to amount prescribed. For all bone meshes created, there were typically less than ten iterations required to reach convergence.

#### 5.4.3 Triangle Reduction

In addition to surface smoothing, the total number of triangular facets in each bony model was also modified using the "quality preserving triangle reduction" tool. Based on previous efforts using tessellated surfaces, it was known that extremely fine surface meshes can be computationally intensive for the purposes of rigid body modeling. Thus, the purpose of using the triangle reduction tool was to reduce the computational load of these surfaces while still preserving as much physiologically relevant detail as possible. The unmodified STL files had varied numbers of facets depending on the size of the bone (number of pixels) and its level of

curvature; typically, these initial meshes had 18-50k triangular facets. Through trial and error, it was discovered that the CAD modeling package, Solidworks 2007, could not import STL files with greater than approximately 25k triangular facets. Thus, a target mesh size of 20-25k facets was chosen in order to maximize the surface fidelity of each bone while working within the constraints of the CAD modeling package. Other than selecting the mesh, there were just three adjustable parameters in the quality preserving triangle reduction tool. These were the "shape quality threshold," the "maximum geometrical error," and the "number of iterations." As stated previously, the "R-in/R-out" shape measure was used to quantify mesh quality and a threshold of 0.8 was set as a lower limit for triangle quality. The maximum geometrical error and number of iterations were set to the 3-Matic defaults of 0.05 and 3, respectively.

Finally, the surfaces of all bone STLs were filtered for highly acute "sliver" triangles. Though the smoothing and triangle reduction steps typically produced very high quality meshes with most facets being close to ideal equilateral triangles, there were often a small number of facets, typically less than 50, that would remain in areas of high curvature. These were removed using the "filter sharp triangles" tool. Specifically, a lower angle limit of  $15^{\circ}$  was set, below which any highly acute triangle would be deleted and the adjacent edges connected.

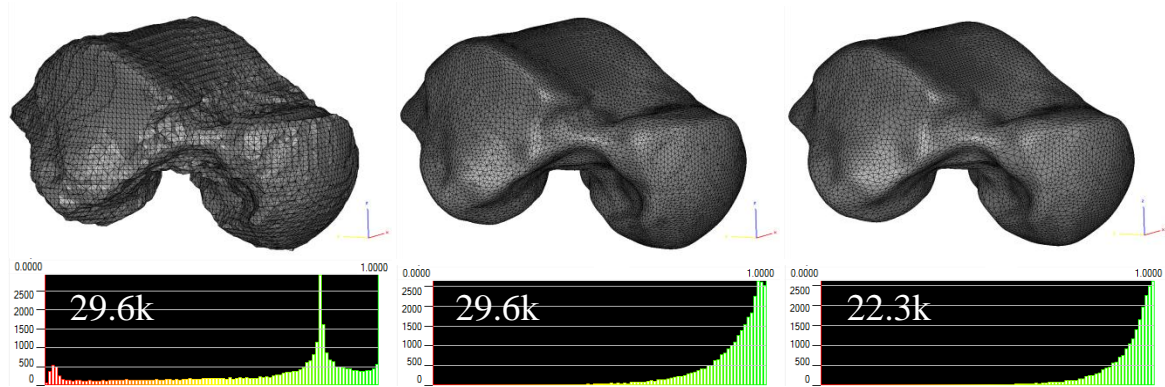


**Figure 5-6: Example STL body of a talus. (LEFT) The original body with shape quality histogram below and number of triangular facets in thousands; (MIDDLE) following only surface smoothing; (RIGHT) with smoothing and triangle reduction. Note that a histogram value = 1, indicates an ideal, equilateral triangle.**

A concern with any smoothing or mesh reduction is that the manipulated volume will be significantly smaller than the input volume. Given the modest smoothing and reduction parameters used, it was not anticipated that there would be significant volume change. This was later verified for all bone STL meshes in the six models created wherein the volume of the finalized bodies was reduced by an average of less than 0.2% from the initial tessellations. [APPENDIX B] This is under the volumetric error inherent to either MRI or CT imaging with voxel sizes of approximately  $0.7\text{mm}^3$  and thus not likely a significant source of error in the modeling process.

Interestingly, neither Solidworks documentation nor technical support offer any definitive limit on the mesh size import limits of the software. Based on our previous work, meshes of around 10k facets were the limit on a 32 bit installation of Solidworks 2007, run on a computer

with 4 gigabytes of RAM. The current work approximately doubles the mesh size at around 25k facets on a 64 bit installation of the same software and a computer with 32 gigabytes of RAM. This is an eight-fold increase in memory for just a two-fold increase in mesh size. This exponential increase in computational cost and the fact that many of the meshes for the smaller tarsal bones were able to be imported at the native resolution of the MRI scanner suggest that there remains little additional computational or physiological value in further increasing the size of the surface meshes without accompanying increases in scanner resolution.

## 5.5 CHARACTERIZING THE MODELS

### 5.5.1 *Long Bone Axes*

The ability to impose a uniform coordinate system was critical for accurately comparing kinematic behavior amongst the models. Further, it was equally important that such a coordinate system be anatomically relevant, so that observations regarding relative bony motions could be easily interpreted in the context of their clinical relevance. To that end, the geometry fitting toolbox native to the 3-Matic program was used to calculate the best-fit long axis of the tibia and all metatarsals for each of the six models. This was accomplished by first importing the bone geometry of interest into the 3-Matic workspace. Next, the proximal and distal most points were identified and their separation distance recorded. The bones' diaphyses were then identified as the middle 75% of the total bone length. Finally, a 3-D best-fit line was fit to this middle 75% selection using the geometry fitting tool. The equation for the fitting routine used is given below where:

$$D = \sum_i^N \frac{d(\vec{x}, x_i)^2}{N} \quad (4)$$

Here the deviation (D) is summed across all the control vertices ( $i=1,2,...N$ ) and the position of the fit geometry resulting in the lowest deviation value is considered the best fit.<sup>104</sup>

Following the diaphyseal long axis calculation, the tibia and fibula models of each patient were further characterized by adapting the anatomic coordinate system proposed by Wu et al on behalf of the International Society on Biomechanics.<sup>107</sup> Here the medial and lateral malleoli were identified on the tibia and fibula, respectively, and the center point of a line connecting the two was designated. The transverse plane (z-x) was defined as being normal to the best-fit diaphysis at the level of that intermalleolar (IM) point. The sagittal plane (y-x) was defined as perpendicular to the transverse plane and containing both the diaphyseal axis and the IM point. The coronal plane (z-y) was then mutually perpendicular to both the transverse and sagittal planes. The intersection of these planes was then defined as the origin (O) for the entire foot and ankle complex with +Y directed superiorly, +X directed anteriorly, and +Z directed to the right. [Figure 5-7]

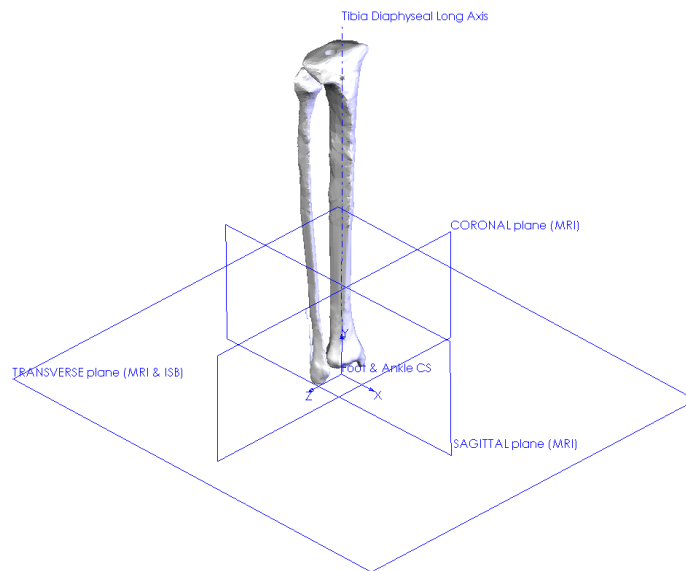


**Figure 5-7: Isometric view showing the best-fit tibia diaphyseal long axis and the derivative ISB coordinate system for a right lower extremity.**

### 5.5.2 Talar Dome

While care was taken to position the patients' feet in neutral plant/dorsiflexion during their MRI scans, all patient models nonetheless deviated slightly from the intended 90° angle between the tibial diaphyseal long axis and a line connecting the heel pad and the metatarsal head in each patient scan. This deviation averaged  $2.3^\circ (\pm 2.3^\circ)$  away from neutral across the six patients imaged. Thus, in order to initially position each of the models in neutral plant/dorsiflexion, the tibiotalar axis was approximated as a hinge joint with a rotation axis defined by the cylinder fit of the superior talar articular surface.

Unlike with the long axis fits described above, the rotation about the tibiotalar joint required fitting a cylinder to just the superior talar articular surface. When initially developing

the models, the then most current version of MIMICS (v12.0) lacked the functionality to fit geometries to an open contour. That is to say, MIMICS v12.0 was unable to fit a cylinder only to the superior articular surface, while excluding the more distal parts of the talus. To address this, a small custom computer program was developed that could fill this gap in functionality.

The custom geometry fitting program was developed in Matlab® (2010b, The MathWorks, Natick, MA, USA) using the vertex coordinates of the superior talar articular surface as inputs. These vertices were selected by inspection in 3-Matic and exported as a comma delimited file (\*.csv). When initialized, the Matlab program prompted the user for an input, at which time the superior talar articular surface file was selected. Once imported, the data were parsed into a 3-D array where the 'x' (sagittal) position of every input vertex corresponded to the slice position from which that pixel was derived. In this way, there were many vertices with unique 'y,z' positions that shared a common 'x' value. The routine was designed to exploit this feature of the dataset in order to derive the best fit cylinder. Specifically, the routine would first check that a given slice contained at least "N" coordinates. Initially, "N" was set to equal four 'y,z' coordinates as that is the minimum number of points that can be input for a least-squares minimization problem. If the slice did not meet this condition, the program would step to the next sequential slice. If the slice did have at least "N" points, a best fit circle was calculated using the least-squares minimization described in Equation (4). The resulting 'y,z' coordinate of this circle center was then stored for a given 'x' slice and the routine stepped to the next slice location. In this way, the best fit circle was calculated for all slices represented in the input data; this was typically 75-85 slices for each patient. Once all the circle inputs had been calculated, a best fit 3-D line was fit to this array its position reported to the user. Finally, in



order to control for different numbers of vertices on a given slice, the minimum required number of vertices ("N") was iteratively increased from four to the maximum number observed across the data set and a new 3-D line calculated for each iteration. A stop condition (value of "N") was designated for when the angle of the 3-D line was changed by less than  $1^{\circ}$  in an iterative step. Across the six patients, this convergent number of vertices was found to be between 15-20 in a given slice.

Interestingly, in the course of the three years following initial development of the Matlab tibiotalar axis fitting routine, MIMICS went on to introduce an open contour surface fitting toolbox within their software. While this addition arrived too late to be incorporated into the now developed models, it did provide a means to benchmark the custom program. So, given the same input files, the MIMICS (v14.14) tool box calculated the tibiotalar 3-D axis within  $1.5^{\circ}$  for all six patients. None of the axes were identical however, indicating that the internal stop condition for the MIMICS tool was slightly different than that for the custom program. An example of the custom program and its later-implemented MIMICS counterpart are shown in Figure 5-8.

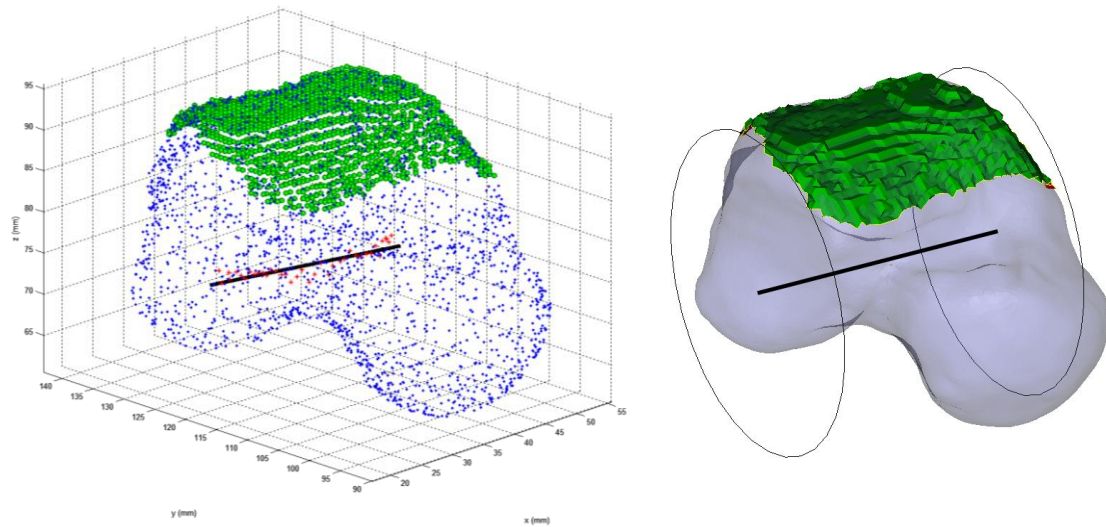


**Figure 5-8: Isometric view of superior articular surface of the talus (green) shown in the context of the rest of the talar surface (blue) with the best-fit tibiotalar flexion/extension axis (black line). LEFT: Custom Matlab program output; RIGHT: MIMICS native shape fitting tool introduced in a later version.**

## 5.6 ANATOMY RECONSTRUCTION

Given the constraints of isovolumetricity and resolution in the MRI DESS scans, it was not possible to capture the entire lower extremity below the knee in a single scan field of view. Therefore, it was decided that the entire foot and ankle complex be captured in the field of view of the DESS sequence while a second coarser MRI scan would capture the proximal and middle tibia and fibula. As a result of this imaging protocol, it was necessary to reconstruct and amalgamate the geometries for bones that were outside of the field of view or were captured in more than one scan. Broadly, this meant reconstructing the 5th metatarsal diaphysis on four of the six patient DESS scans as well as connecting the proximal low resolution tibia and fibula models to the higher resolution DESS scans for all six patients.

### *5.6.1 5th Metatarsals*

For three of the six patients' MRI scans of the foot and ankle, the lateral limits of the field of view excluded the lateral most portions of the 5th metatarsal bone. Additionally, in a fourth patient, a metatarsal fracture fixation plate from a previous surgery caused the MRI field to scatter, thereby obscuring the underlying 5th metatarsal anatomy. Thus, in four of the six patients, it was necessary to reconstruct the distal 5th metatarsal bone models.

In all four cases, the proximal articular surface and proximal metatarsal tuberosity were retained along with the medial most margin of the distal metatarsal head. However, the interstitial bone was partially to completely missing across the four patients. As there are no ligamentous or extrinsic muscle attachments along the diaphysis of the metatarsals, the interstitial bone morphology was not critical for model function. By contrast, the distal metatarsal head has numerous muscle, ligament, and fascial attachment points, especially on the plantar aspect. Moreover the distal metatarsal head's position and orientation has pronounced effects on the lateral load distribution of the foot. Thus, the most critical aspect of the reconstructions was the faithful reproduction of the distal metatarsal head shape, positional, and orientation.

Given the 5th metatarsals' complex organic shape and the lack of information necessary to model the distal head entirely from user-generated drawings, a scaled duplicate of the respective patients' 4th metatarsal head was instead used as a surrogate. Specifically, the 4th metatarsal bone mesh was copied and cropped at the distal margin of the diaphysis perpendicular to the diaphyseal long axis. This bone was then scaled down to 95% of its original size based on size comparisons of the distal metatarsal head sizes for the two patients with complete scans.

Next, a sphere was fit to the medial most portion of the 5th metatarsal and its anterior articular margin marked with a point in each of the four patients' MRI scans. Likewise, a sphere was fit to the scaled 4th metatarsal duplicate for each patient and the centers of the two sphere fits were made coincidental, ensuring that the surrogate metatarsal head did not extend anteriorly past that of the native head. The orientation of the 4th metatarsal head was preserved in creating the 5th metatarsal head surrogates.

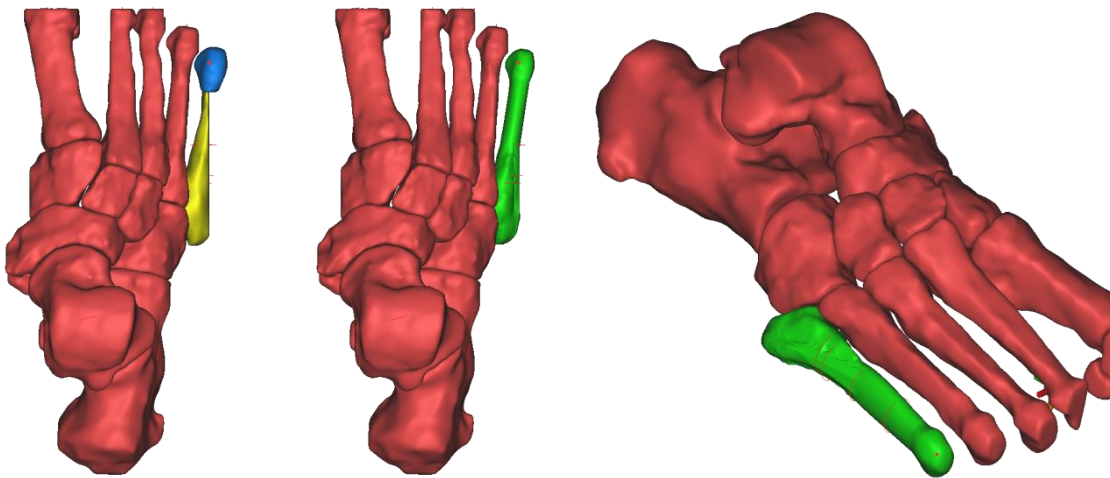


**Figure 5-9: Typical reconstruction of the 5th metatarsal bone. LEFT: Dorsoplantar view of the native 5th metatarsal (yellow) with the scaled duplicate of the 4th metatarsal head in place (blue). MIDDLE: Dorsoplantar view of the reconstructed 5th metatarsal (green). RIGHT: Isometric view of the reconstructed bone with loft contours and sphere-fit center of the distal metatarsal head (red lines).**

With the distal metatarsal head reconstructed, the interstitial bone had to be created. As three of the four cropped scans did capture most of the medial margin of the 5th metatarsal diaphysis, a series of circles constrained to the coronal plane were fit around the portions of the masks still present by inspection. These circles were then used as contours through which the

distal head could be lofted to the proximal metatarsal base. The medial diaphyseal margin could not be discerned in Patient 4 due to the MRI scatter caused by a metal fracture fixation plate and as such the body of her 4th metatarsal was incorporated as a framework for recreating the 5th metatarsal diaphysis. As stated previously, these diaphyseal recreations did not contain any soft-tissue attachment points and did not have any adjacent bone or ground contact and were thus mostly aesthetic.

### *5.6.2 Proximal Tibia and Fibula*

As we desired to create a rigid body model of the entire lower limb distal to the knee, it was necessary to recreate unified tibia and fibula models assembled from the high resolution DESS and lower resolution T1 TSE scans obtained for each patient. In order to accomplish this, the disparate coordinate systems within each mesh, which were a consequence of using different imaging coils in the MRI scanner, needed to be reconciled. Since the relative positions of the tarsal bones was critical for later stages of model development, the lower resolution T1TSE tibia and fibula STLs were mapped to their higher resolution DESS scan derived counterparts using the STL registration tool within 3-Matic. Specifically, the lower resolution tibia and fibula STLs were imported into the higher resolution DESS workspace for each respective patient. Next, each was manually positioned in the approximate vicinity of the higher resolution scan by inspection. This manual position then served as an initial guess for the iterative least-squares mapping of the low resolution scan to the high described above in Equation (4).

Once mapped to the desired bone, both the high and low resolution STL files were imported into the CAD package Solidworks 2007 with their updated coordinated systems. A plane roughly orthogonal to the diaphysis of the bone was then created and used to trim the

superior margin of the high resolution bones and the inferior borders of the low resolution bones such that the two meshes did not overlap and were separated by approximately 50mm. This separation was then filled by lofting the outer profile of the high resolution cut surface to that of the low resolution surface using a similar methodology as outlined for the 5th metatarsal reconstructions. An example of how these two bony STL meshes were joined is shown below.

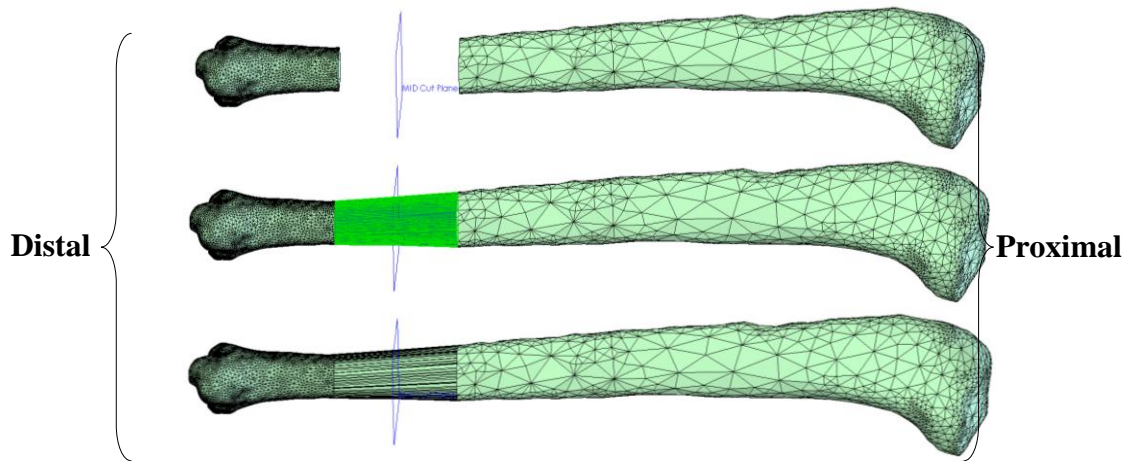


**Figure 5-10: Example tibia model constructed from the least-squares fit of the high resolution STL mesh (left) to the low resolution STL mesh (right) with the lofted connection shown in bright green.**

## **6. RIGID-BODY KINEMATIC SIMULATIONS**

### **6.1 OVERVIEW**

Once the 3-D lower leg geometry of all six patients had been faithfully recreated from the MRI scans, the models were imported into the commercial CAD package Solidworks (v2007, Dassault Systèmes SolidWorks Corp., Waltham, MA, USA). Using this design suite, the patient bones were able to be reassembled and oriented according to the ISB coordinate system outlined in Section 5.5. Once imported, Solidworks provided a means of recreating tendons paths as they wrap bony geometry and tracking soft-tissue origins and insertions in 3-D space. The Solidworks add-in COSMOSMotion was further used to incorporate the relative positions of these soft-tissue as inputs in force-displacement equations that defined the tensile function of the passive capsuloligamentous constraints and active muscle contraction in the lower leg. Additionally, the COSMOSMotion add-in was used to impart body weight perturbations and define the boundary conditions for calculating bone-to-bone as well as bone-to-ground contact. Thus, all six patient-specific computational rigid body models were able to be reconstructed in three dimensions and constrained only using physiologic articular contact, active muscle contraction, passive soft-tissue tension, body weight perturbations, and ground contact.

### **6.2 DEFINING NEUTRAL PLANTARFLEXION**

As prefaced in Section 5.5.2, it was important that all six models be initially positioned in neutral plantar/dorsiflexion so that equivalent portions of stance could be evaluated. Thus, while

each patient was imaged as close to neutral as possible, all six models required slight adjustments in their initial position. These adjustments were made within Solidworks in the following manner. First, the ML radiographs, corrected for magnification, were used to determine the thickness of the loaded metatarsal and heel fat pads. The difference in these two thicknesses was then incorporated into the model loading bases as a stepped riser under the calcaneus. The relative heights of the fat pads for each patient are given below in Table 6-1.

**Table 6-1: Fat pad thicknesses measured on the loaded ML X-rays and the derived loading base heel offset values for all six patients.**

|              |   | <i>Met. Fat Pad</i> | <i>Heel Fat Pad</i> | <i>Base Riser (<math>\Delta</math>)</i> |
|--------------|---|---------------------|---------------------|---|
|              |   | (mm)                | (mm)                | (mm)                                    |
| Patient<br># | 1 | 6.0                 | 10.2                | 4.2                                     |
|              | 2 | 2.0                 | 5.0                 | 3.0                                     |
|              | 3 | 4.0                 | 8.0                 | 4.0                                     |
|              | 4 | 3.0                 | 9.0                 | 6.0                                     |
|              | 5 | 5.0                 | 11.0                | 6.0                                     |
|              | 6 | 4.0                 | 7.0                 | 3.0                                     |

Second, the inferior most point on the calcaneus and in the metatarsal heads was identified. Given different levels of forefoot collapse, the most plantar point in the forefoot differed among the patients but was most often in the 1st or 5th metatarsal head. Next, all bones of the foot were fixed relative to the talus for each model so that rotation about the best-fit talar plantar/dorsiflexion axis calculated above would cause the entire foot to rotate relative to the tibia and fibula. Finally, the loading base with patient-specific heel riser was incorporated into each Solidworks model assembly such that its surface was orthogonal to the tibia diaphyseal long axis and thus parallel to the ISB transverse plane. Further, the inferior most points of the



forefoot and heel in each model were made coincident with the loading base surface, thereby inducing the requisite rotation about the tibiotalar plantar/dorsiflexion axis. This procedure is outline graphically in Figure 6-1.

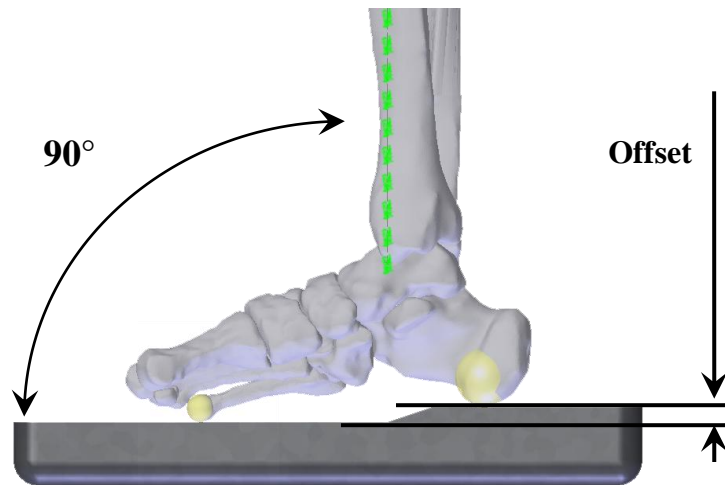


**Figure 6-1: Neutral plantar/dorsiflexion enforced by orienting the loading base with patient-specific heel riser orthogonal to the tibia diaphyseal long axis (green). Coincidence of the inferior most points on the heel and forefoot (yellow).**

With the extremity aligned to the base, it was then necessary to insure that each patient's full body weight was applied perpendicular to this base. To accomplish this, a simple loading pin and collar assembly were incorporated into the proximal end of each tibia similar to those used previously for loading of cadaveric extremities in the Orthopaedic Research Laboratory.<sup>48–50,108</sup> Specifically, a 12.7mm (1/2") diameter rod was centered about the tibia diaphyseal axis that extended approximately 100mm (~4") above the tibial plateau. Additionally, a small rectangular key channel was modeled into the proximal half of the rod and oriented such that it was parallel to the sagittal plane defined by the ISB coordinate system outlined above. Lastly, a cantilevered

segment was modeled extending posterior from the center of the rod in order to provide an origin for the posterior compartment muscle vectors. A collar was then created with a channeled hole through its center, mimicking the cross-sectional shape of the rod. When centered around the rod, the collar allowed a fixed point of reference from which to apply the body weight loading to the rod. Further, the channel in the posterior portion of the collar ensured that there was no internal or external rotation of the tibia during loading. An example of the loading assembly can be seen below.

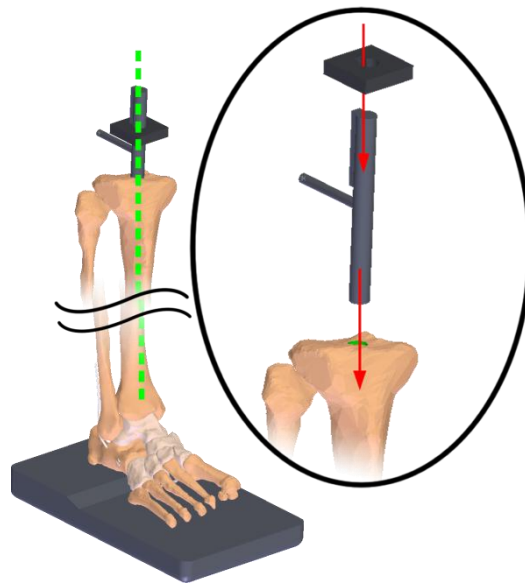


**Figure 6-2: Isometric view of the loading pin aligned collinear with the tibia diaphyseal axis and the collar parallel to the base. INSET: Exploded view of the loading apparatus.**

### 6.3 ORIGINS AND INSERTIONS

In order to ensure that the passive soft-tissue constraints were consistently represented across the six patient models, the origins and insertions of all tissues were marked and fixed relative to their attaching bone. Specifically, every attachment was represented by a unique 3-D

sketch point, wherein the origin or insertion was said to be coincident with a neighboring triangular facet vertex or edge midpoint in agreement with anatomic literature, atlases, cadaveric dissection, and patient osteology.<sup>24-31,88,109,110</sup> For broad or fan-shaped tissues with large areas of attachment, multiple points were used to describe the structure, with most ligaments being described by at least two pairs of origins and insertions at the lateral margins of the tissue, and most capsular structures being described by equally distributed arrays of five to ten pairs of points. Thus, the lines of action for all passive soft-tissues of the foot were initially described by one or more straight line vectors connecting the tissue origin to insertion. These vectors and their separation distance provided the basis inputs for the calculation of corresponding tissue strain and force.

#### 6.4 COSMOSMOTION

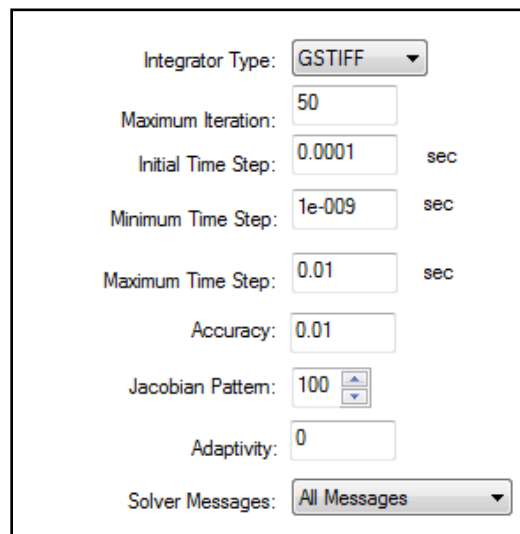
The COSMOSMotion rigid body simulation package is fully integrated into the Solidworks work space. This add-in provides the ability to apply a wide variety of force perturbations and mechanical constraints to geometries created in Solidworks. Further, the add-in incorporates a number third-party differential equation solvers that can be used to numerically solve the kinematic equations describing the system.

The first step in using this add-in was designating which geometries were grounded and which were subject to perturbations. For the six patient models, only the base and the loading collar were considered fixed. The tibia was constrained to vertical displacement along its diaphyseal long axis only, as dictated by the loading pin apparatus described above. All other bodies were free to move in all six degrees of freedom and were constrained only by their bone or ground contact, ligament tension, and muscle force, which are described in detail below.

#### 6.4.1 Solver Parameters

At the core of the COSMOSMotion rigid body motion suite is the Automated Dynamic Analysis of Mechanical Systems (ADAMS) (v2007, MSC Software Corp., Santa Ana, CA, USA) solver package.<sup>111,112</sup> This set of algorithms uses the Solidworks derived geometries and traditional solid mechanics equations of motion to predict the kinematic behavior of objects subjected to user-defined forces, torques, displacements, and between-body contacts. More specifically the ADAMS suite incorporates the robust and widely used "Gear Stiff" (GSTIFF) numerical integrator to maximize computational efficiency while solving higher order differential equations with very disparate rates of change. This is particularly appropriate for multibody systems wherein both high frequency (e.g. rigid body-body contact) and low frequency (e.g. force vectors and springs) terms can influence a body's behavior. Efficiency is maximized, and computational time minimized, by allowing the GSTIFF integrator to automatically adjust the size of the integrator time intervals, or 'steps', based on a user-defined threshold of the truncated error experienced by the integrator. That is to say, during periods where the function solution is varying slowly, i.e. at a low frequency, the integrator will take larger steps and thus the system will be approximated with fewer intervals in a given second. An example of this scenario might be two separate bodies being pulled together by a 'soft' spring or ligament. Conversely, under conditions with very high frequency changes in the components, such as when two rigid bodies come in to contact while still being constrained by springs, the error will likely be outside of the acceptable threshold. The GSTIFF integrator will then retreat and repeat the last integration with a smaller time interval, repeating as necessary until the system can proceed with sub-threshold error. This "predict, compare, correct" methodology thus

provides the fastest means of solving for the kinematic behavior of stiff multibody systems while accruing minimal error.<sup>113,114</sup> The user-defined inputs for this solver are shown in Figure 6-3 and represent the software limits of minimum and maximum time steps and number of iterations. The values used for the "Jacobian Pattern" and "Adaptivity" terms specify that the Jacobian matrix for the entire system is recalculated for every iteration instead of being assumed constant, allowing for sparse and/or intermittent contact between bodies.



The screenshot shows a software interface for configuring solver conditions. It contains the following elements:

- Integrator Type:** A dropdown menu with "GSTIFF" selected.
- Maximum Iteration:** A text input field containing the value "50".
- Initial Time Step:** A text input field containing "0.0001" followed by a unit label "sec".
- Minimum Time Step:** A text input field containing "1e-009" followed by a unit label "sec".
- Maximum Time Step:** A text input field containing "0.01" followed by a unit label "sec".
- Accuracy:** A text input field containing the value "0.01".
- Jacobian Pattern:** A text input field containing "100" with up and down arrow buttons.
- Adaptivity:** A text input field containing the value "0".
- Solver Messages:** A dropdown menu with "All Messages" selected.

**Figure 6-3: COSMOSMotion interface for input of ADAMS solver conditions.**

#### 6.4.2 *Contact parameters*

The overarching goal of this work was to develop kinematic models whose function was influenced only by physiologic constraints and perturbations. In relation to joint and ground contact, this required that no artificial or mechanical approximations be used. As such, all contact within the models was accomplished using the process of penalty regularization. This rigid body contact technique allows the ADAMS algorithms to numerically solve non-idealized,

intermittent, 6 DOF contacts. Generally, this method involves calculating the volumetric overlap between any two bodies for a given time step. A force vector originating at the centroid of this volume is then automatically applied and oriented along the shortest path to the overlapped surface, thereby acting to separate the two bodies. The magnitude of this restoring force is thus contingent on the stiffness of the materials and amount of overlap. For cases of rigid body contact, where the deformations of the constituent bodies can be considered infinitesimal relative, the stiffnesses used in the penalty regularization method are chosen to be very large, thereby minimizing the amount of overlap required for the bodies at equilibrium. Finally, while this method does not preclude the incorporation of frictional contacts, friction was neglected in all 3-D contact in the models. This assumption was made given the extremely low frictional coefficients observed for hyaline cartilage covered synovial joints in the human body.<sup>115–117</sup> A generic example of the penalty regularization method is given below.

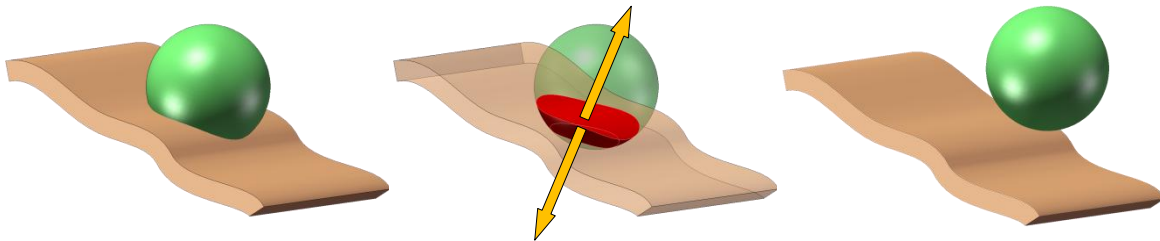


**Figure 6-4: Diagram of the penalty regularization approach used to solve for rigid body contact within the model. LEFT: two overlapping bodies; MIDDLE: the common volumetric overlap and associated restoring force is calculated; RIGHT: the bodies no longer in contact.**

The first step in implementing this methodology using COSMOSMotion, is to designate all allowable contacts within the software. Initially, all contact permutations were allowed

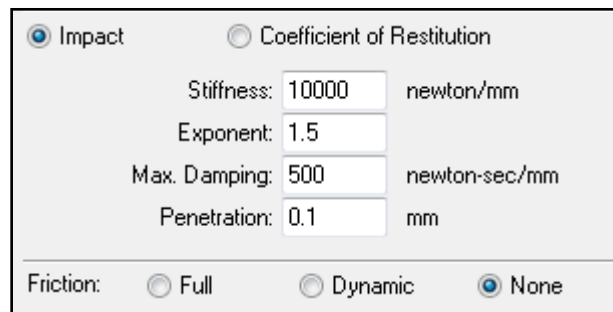
within each model. With 15 solid bodies in each model (14 bones and 1 base), this meant there were 105 possible pairwise contact sets. That is to say, the talus contacting the 1st metatarsal and the tibia touching the base were allowable contacts. While computationally expensive, this initial setup allowed verification that all bodies within the six models were well restrained and not moving in a grossly unphysiologic manner, e.g. the talus did not contact a metatarsal. Subsequently, all joint contact sets were redefined, incorporating only their nearest neighbors. Thus, for example, the talus was allowed to contact the tibia, fibula, calcaneus, navicular, and the cuneiforms, but not the metatarsals. Base contact was permitted between any bone of the foot and the base; base contact with the tibia and fibula was not permitted.

With the contact sets defined, the next step was to define the terms dictating the force opposing body-body contact expression used in the penalty regularization method. Within COSMOSMotion, this expression is

$$F_n = k * g^e - Step\left(\frac{dg}{dt}, 0, 0, c_{max}, d_{max}\right) \quad (5)$$

Where  $F_n$  is the separating force vector applied to both contacting bodies. This vector originates at the centroid of the overlapped volume and projects outward along the shortest path toward the margin of the overlapped surfaces, the penetration distance ( $g$ ). Therefore, for any volumetric overlap between bodies, there is a pair of force vectors with shared origins and directions, but opposite signs acting to move the two overlapping bodies apart. The other terms influencing  $F_n$  are the material stiffness ( $k$ ) and an exponent ( $e$ ). Given the goal that all contact within the models result only from physiologic soft-tissue forces and that there is minimal deformation of the bones during normal stance contact, the values for  $k$  and  $e$  were maximized such that kinematic equilibrium could be achieved while minimizing the penetration distance term ( $g$ ). As a consequence, the overlap of any two contacting bodies was infinitesimal compared to the volume of the entire bone(s).

In addition to the material stiffness and penetration distance, a damping term with modest coefficients was included to address large spikes in  $F_n$  that can sometimes result from intermittently contacting bodies colliding at relatively high velocities. Thus, for body-body overlap with colliding velocities ( $\frac{dg}{dt}$ ) greater than zero, the restoring force ( $F_n$ ) was attenuated by a damping function with stepped coefficients based on user specified values of maximum damping force ( $c_{max}$ ) and overlap distance at which maximum damping force is achieved ( $d_{max}$ ). The COSMOSMotion interface and user-defined values are given below.



|   |  |
|---|--|
| <input checked="" type="radio"/> Impact | <input type="radio"/> Coefficient of Restitution   |
| Stiffness:                              | 10000 newton/mm  |
| Exponent:                               | 1.5  |
| Max. Damping:                           | 500 newton-sec/mm  |
| Penetration:                            | 0.1 mm   |
| Friction:                               | <input type="radio"/> Full <input type="radio"/> Dynamic <input checked="" type="radio"/> None |

**Figure 6-5: COSMOSMotion interface for defining the contact conditions between bones within all models.**

## 6.5 BODY WEIGHT AND MUSCLES

In addition to passive soft-tissues such as ligaments, capsule, and plantar fascia, patient-specific body weight and the extrinsic plantar flexors of the foot were also incorporated in the six models. Given the goal of investigating single leg stance in AAHD sufferers, each model incorporated the respective patient full body weight acting down the tibia collinear with the tibia diaphyseal axis. In order to avoid impulse loading an already stiff rigid body system, only 20N



were initially imposed on the tibia, with the remainder of the body weight force ramping on over the first two seconds of simulation time. Likewise, muscle loading associated with the posterior, medial, and lateral compartments of the calf were incorporated. These included the gastrocnemius/soleus complex, the FHL, the FDL, the PL, and the PB. Each of these extrinsic muscles was prescribed a steady-state tension effected along the course of the tendon with magnitude scaled relative to the patient-specific body weight.

The relative contributions of each of the extrinsic muscles modeled were initially adapted from works by Murray though the values reported are similar to those reported by many other authors.<sup>84,97,118–122</sup> In the case of Murray, the plantar flexion force was measured using a tensiometer fastened to the forefoot in a single patient with unilateral gastrocnemius/soleus excision. Using the intact contralateral limb as a control, the relative contributions of the gastrocnemius/soleus, FDL, FHL, PB, and PL were calculated based on the surgical side reduction in force, physiologic cross sectional area, and tendon moment arm. These reported values have been subsequently validated by other authors incorporating additional muscle parameters such as fiber lengths, pennation angles, and electromyography.<sup>97,118,119,121</sup> The contributions of each muscle scaled relative to body weight are given in Table 6-2.

**Table 6-2: Muscles incorporated into each of the six models, their force scaling relative to body weight, and the number of vectors used to represent each muscle.**

| Compartment | Muscle(s)               | Abbreviation | % BW  | # of vectors |
|-------------|-------------------------|--------------|-------|--------------|
| Posterior   | Gastrocnemius / Soleus  | Achilles     | 50.0% | 4            |
| Medial      | Flexor Digitorum Longus | FDL          | 6.0%  | 4            |
|             | Flexor Hallucis Longus  | FHL          | 10.5% | 1            |
| Lateral     | Peroneus Brevis         | PB           | 8.8%  | 3            |
|             | Peroneus Longus         | PL           | 10.0% | 4            |

#### 6.5.1 *Achilles Tendon Course*

The gastrocnemius/soleus complex in the posterior calf was incorporated as an array of four plantar flexing elements oriented along the line of the Achilles tendon and inserting on the calcaneus. Given the in vivo origin of the complex has attachments on the femur and that this bone was not incorporated into the bony models, the origin for all four elements was set on the cantilevered portion of the loading rod described in Section 6.2. The insertion of the elements was evenly distributed along the posterosuperior ridge of the calcaneal tuberosity. Though the gastrocnemius/soleus muscle complex is capable of effecting large excursions of the Achilles tendon, there is no significant nonlinearity to the Achilles line of action, especially during the stance phase of gait. As such, Achilles force was approximated as the straight line tension from the calcaneal insertions to the loading pin as shown in Figure 6-6. The 50% BW force designated to the Achilles was apportioned equally among the four tissue elements.

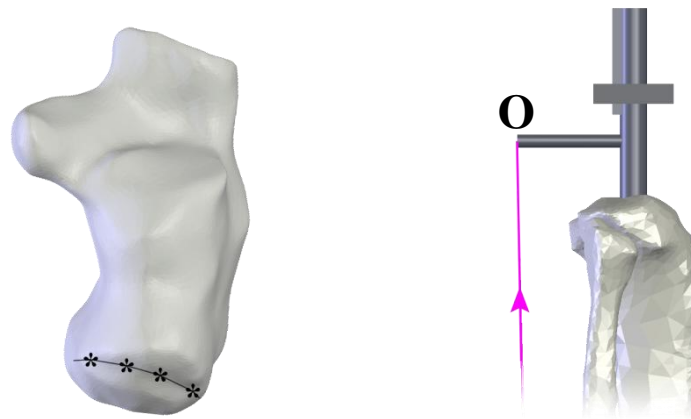


**Figure 6-6: LEFT: Dorsoplantar view of a calcaneus demonstrating the four insertion points of the Achilles tendon elements. RIGHT: Lateral view of the Achilles origin.**

#### 6.5.2 *FHL Tendon Course*

The flexor hallucis longus (FHL) tendon path was modeled as follows. Because the in vivo tendon travels inferiorly behind the talus before turning sharply anterior under the sustentaculum tali, its effects cannot be modeled as simple straight line tensile vectors from origin to insertion. However, COSMOSMotion constrains force elements to operate in just this straight line manner. Thus, a system of interstitial bead elements was devised to allow the tendon path to wrap the calcaneus geometry. First, the anteroposterior extents of the talocalcaneal tunnel through which the FHL travels were marked as reference on the medial calcaneal wall. Two ellipsoidal beads were then created to serve as attachment points between the two segments of FHL element. These beads were then constrained to travel along a spline approximating the talocalcaneal tunnel. Subsequently, the proximal half of the FHL element had its origin placed at a point offset from the posterior aspect of the distal tibia in agreement with published and patient-specific anatomy and inserted on the proximal bead. The distal half of the

FHL element then originated from the distal bead and inserted at the distal 1st metatarsal head.

As the two elements are in series, the full 10.5% BW tensile force ascribed to the FHL was assigned to both elements.

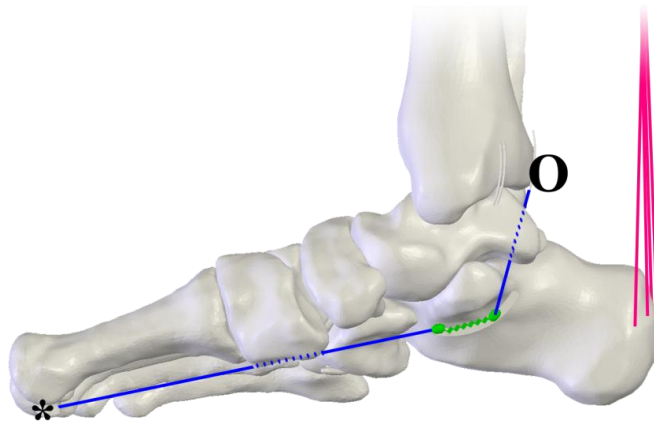


**Figure 6-7: Right foot model equilibrated under load showing the course of the FHL (blue) with interstitial beads (green), other soft-tissues are hidden for clarity.**

The advantages of modeling the FHL in this way are twofold. First, the non-linear line of action of the FHL could be faithfully modeled within the constraints of the modeling software. Second, the native FHL's effect of supporting the medial longitudinal arch by pulling the 1st metatarsal toward the calcaneus was preserved. The most substantial disadvantage of this technique is the added computational cost and instability imparted by having minimally constrained small bodies subjected to large forces.

### *6.5.3 FDL Tendon Course*

Like the FHL, the flexor digitorum longus (FDL) also courses non-linearly from its origin on the tibia to its insertion on the distal 2-5th metatarsals. Moreover, just as the FHL supports the medial arch by drawing the 1st metatarsal closer to the calcaneus, the FDL supports the arch

by pulling superiorly on the plantar surface of the navicular, thereby indirectly reinforcing the talonavicular articulation. Therefore, in order to faithfully represent both the direct plantar flexing action of the FDL as well as its indirect support of the arch, a similar system of interstitial beads was employed. Specifically, the center of a single ellipsoid bead was confined to a plane defined by the inferior most points of the navicular tuberosity, navicular beak, and the sulcus between them. It is likewise constrained by physical contact with the navicular above it.

Once implemented, the proximal segment of the FDL was made to originate at the posterior tibia where the tendon first crosses the talocrural joint. The element then travels a straight line path to insert on the bead as described above. From here, the element is split into four bands, each inserting discretely at a point approximately 1/8" from the plantar surface of the 2-5th metatarsal heads. This small offset was incorporated to mimic the tendon thickness as they pass anteriorly beyond the metatarsal heads and into the toes. The full 6.0% BW tensile force was implemented for the proximal FDL band, and equally apportioned across the distal four bands.

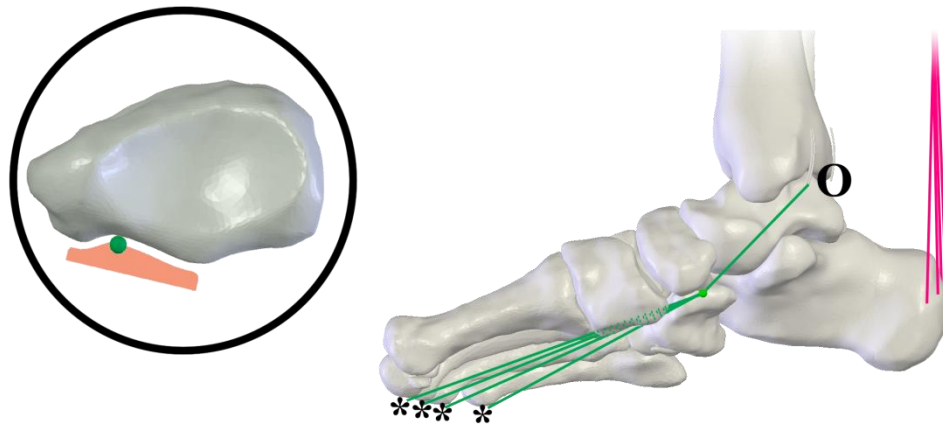


**Figure 6-8: Right foot model equilibrated under load showing the course of the FDL (green) with interstitial bead, other soft-tissues are hidden for clarity. INSET: Detail of the bead (green) constrained by a plane and the navicular surface.**

#### 6.5.4 *Peronei Tendon Courses*

The final muscle elements incorporated into the model are the peroneus brevis (PB) and peroneus longus (PL). Functionally, these muscles act antagonistically to the FHL and FDL in that they are powerful subtalar everters with the PL providing some additional plantar flexion of the 1st metatarsal. However, like both the FHL and FDL, these muscles travel a tortuous path down the posterior calf, bending sharply anterior from behind the lateral malleolus, before becoming tethered to the lateral calcaneal wall by the inferior peroneal retinaculum. From this tethering, the PB courses directly anterior and plantar to insert broadly on the base of the 5th metatarsal. The PL exits this retinaculum and again turns sharply into the plantar peroneal tunnel tethered to the underside of the cuboid.<sup>24,25</sup> The tendon then leaves the plantar cuboid surface and courses anteromedially to insert substantially on the base of the 1st metatarsal with a small slip of tendon also inserting on the 1st cuneiform.<sup>25</sup>

In order to replicate this complex path, a number of interstitial elements were incorporated into each of the models. Beginning proximally, both tendon paths were recreated in Solidworks as rigid 3-D splines. These spline paths allowed easy visualization of the tendon course and provided an anatomically relevant site for the tensile vector origin. Moving distally, two small solid bodies were incorporated into the lateral calcaneal wall, offset from the bony surface by the approximate width of each of the tendons. These interstitial bodies served as insertions for the 8.8% and 10.0% BW tensile vectors of the PB and PL, respectively. In addition to helping approximate the tendons' non-linear course, these calcaneal bodies also caused the muscle function to directly affect the position of the calcaneus, just as the lateral peroneal retinaculum does in vivo.<sup>25</sup> From here, the PB tendon force was apportioned into three vectors of equal magnitude inserting broadly on the proximal 5th metatarsal head. Finally, the PL tensile elements leaving the lateral calcaneus inserted on a final interstitial cuboid body. As with the calcaneal bodies, this 3-D spline followed the anatomic course of the peroneal tunnel and allowed a non-linear pull but also direct PL affect on the cuboid. Leaving the medial margin of the cuboid, the 10% BW PL force was apportioned into four elements, three inserting on the base of the 1st metatarsal and one on the base of the 1st cuneiform.

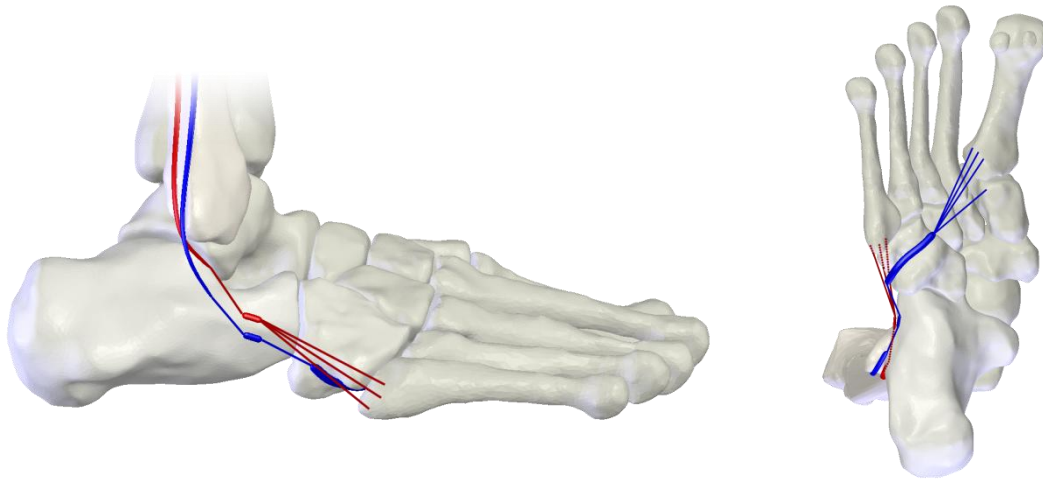


**Figure 6-9: Right foot model showing the course of the PL (blue) and PB (red), other soft-tissues are hidden for clarity. LEFT: Lateral view. RIGHT: Plantar view.**

## 6.6 LIGAMENT CONSTRAINTS

The classification, arrangement, and application of the modeled ligament elements draws heavily from the excellent earlier work of Iaquinio and Liacourus.<sup>4,7,99,123</sup> These authors described the first rigid-body foot and ankle models with non-idealized joint definitions wherein relative bony motion was constrained instead only by the passive soft-tissues in the foot. Thus, while the ligaments generate less force than any of the muscles, the function of the models was utterly dominated by the properties and arrangements of these ligaments elements. The ligaments elements are somewhat similar to the muscles described above inasmuch as the ligament elements were approximated as tension-only vectors coursing from origin to insertion. However, unlike the muscles, the magnitude of ligament tension was not related to BW but instead enforced as a function of the element length, in situ strain, and tissue stiffness. In this way, increased relative motion between two connected bones resulted in increased tensile restraint, just as in the native tissue.



### 6.6.1 *Ligament Arrangement and Properties*

As previously stated, the ligament elements spanned from origin to insertion with the majority of ligaments being represented by 2-5 discrete elements approximating the various constituent bands. These attachment sites were identified by inspection of the patient-specific anatomy and in consultation with anatomic literature, and personal dissection. Moreover, the very high quality scans and denser meshes described in Section 5.4.1 allowed for more precise identification of the small traction bumps indicative of ligament attachment than had been previously possible. In this way, a total of 56 ligaments in the lower leg, ankle, hind-, mid-, and forefoot were represented by 146 discrete passive tension elements. These were coarsely grouped into the following regions: the tibiofibular ligaments, including the interosseous membrane, deltoid complex, medial collaterals (MCL), lateral collaterals (LCL), the dorsal interossei, deep plantar interossei, and superficial plantar ligaments. Abbreviations and linear stiffness values for each ligament element are given in Appendix C.

The tibiofibular ligaments included the proximal attachment of the fibular head just distal to the lateral tibial plateau (PROX-TiFi). Given the minimal motion permitted at the joint in vivo and based on prior modeling work, this articulation was supported by six elements arranged circumferentially about the joint each with an assigned linear stiffness of 200N/mm.<sup>99,123</sup> Moving distally, the large interosseous membrane (IOM-TiFi) of the lower leg was modeled using seven elements equally spaced and oriented roughly horizontally in the first third of the diaphysis and shifting to obliquely distolateral from the tibia to fibula in the lower two thirds of the bones.<sup>124</sup> These bands were collectively modeled as 880N/mm based on force-elongation

measures described for the forearm interosseous membrane and used previously; this corresponded to 126N/mm per element.<sup>99,125,126</sup> [Figure 6-10]

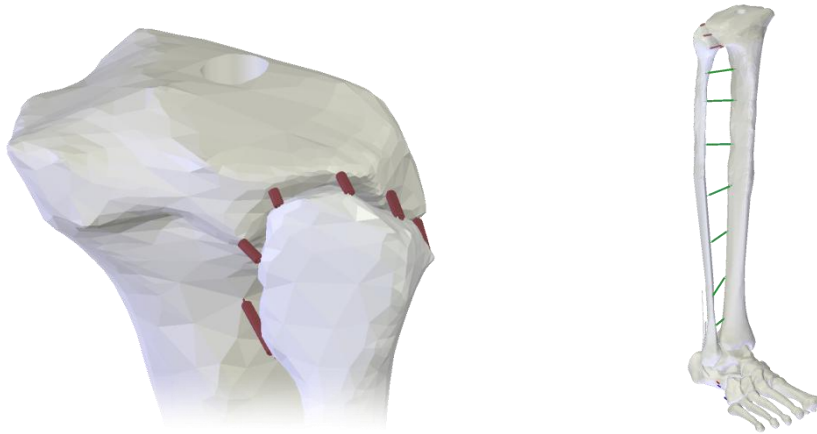


**Figure 6-10: Right foot model showing (LEFT) posterolateral view of proximal tibiofibular elements and (RIGHT) anterolateral view of the interosseous membrane.**

The distal tibiofibular ligaments, a subset of the lateral collateral ligaments, were incorporated as three elements, two anterior bands and one posterior band (LCL\_TiFi-A1,-A2,-P). Other soft-tissue structures modeled in the lateral ankle included two bands of the posterior fibulocalcaneal (LCL\_CaFi-1,-2), two bands of the posterior and one of the anterior fibulotalar (LCL\_TaFi-A,-P1,-P2), one band of the lateral talocalcaneal (LCL\_TaCa-L), and two bands representing the superficial fibular retinaculum (LCL\_SFR-1,-2). Linear stiffnesses for these ligaments ranged from 90-240N/mm based on the works published by Siegler et al. and Attarian et al., and validated previously by Iaquinto and Wayne.<sup>4,99,127,128</sup> Additionally, the talocalcaneal interosseous ligament (IOL\_TaCa-1,-2,-3) was incorporated as three bands each with an intact stiffness of 90N/mm. [Figure 6-11, LEFT]

The represented ligaments in the medial ankle were predominately from the deltoid group. These included the tibiocalcaneal (DEL\_TiCa-1,-2), the tibionavicular (DEL\_TiNa-1,-2),

the tibiospring (DEL\_TiSp-1,-2), the anterior and posterior tibiotalar (DEL\_TiTa-1,-P1,-P2), and the medial and posterior talocalcaneal (MCL\_TaCa-M,-P1,P2). These linear stiffnesses for these ligaments ranged from 80-400N/mm, again based on the work of Siegler et al and previous validation.<sup>4,99,128</sup>

The numerous short interosseous ligaments of the dorsal and plantar midfoot were each modeled using 2-3 bands as described by Iaquinto.<sup>99</sup> Unfortunately, there are few studies directly investigating the biomechanical behavior of these small structures, likely due to their small size, large interpersonal variance, and the mechanical testing challenges that they present. As such, these ligaments were all assigned between 90-270N/mm based on the relative size of the modeled structure and previous validation.<sup>99</sup>



**Figure 6-11: Right foot model showing passive soft-tissue elements. LEFT: Lateral view. RIGHT: Medial view.**

Given the involvement of the spring ligament complex in AAJD, the element arrays used in the current modeling work were expanded somewhat over those first envisioned by Iaquinto. Here, the initial definition of four bands was expanded to better approximate the in vivo

arrangement. Specifically, these tissues were modeled according to the dissection and MRI work by Davis et al., Rule et al., Taniguchi et al., and Schneck et al. with additional bands approximating the inferomedial calcaneonavicular (PLAN\_SPRING\_IMCN-1,-2), the middle calcaneonavicular (PLAN\_SPRING\_MCN-1,-2), and the superomedial calcaneonavicular (PLAN\_SPRING\_SMCN-1,...,-4).<sup>27,29-31</sup> Nonetheless, the total linear stiffness of the complex, 200N/mm, was maintained from the early work by Iaquinio and was apportioned across more elements. [Figure 6-12]

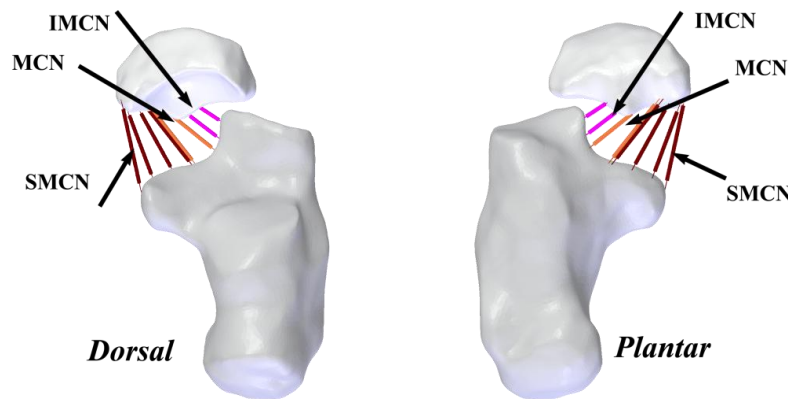


**Figure 6-12: Right model showing spring ligament bands: Inferomedial (IMCN); Medial (MCN); Superomedial (SMCN). LEFT: Dorsal view. RIGHT: Plantar view.**

The final groups of soft-tissues modeled in the foot were the long ligaments and fascia of sole of the foot. These structures lay just superficial to the short interossei described above and included the plantar and inferior bands of the short plantar ligament (PLAN\_CaCu-1,...,-6), the long plantar ligament (PLAN\_LPL-1,...,-6), and the plantar fascia (PLAN\_FASCIA-1,...,-5). [Figure 6-13] In the case of the long plantar ligament and plantar fascia, the native tissue bands extend anteriorly from the plantar surface of the calcaneus and wrap the cuboid before inserting on the proximal and distal metatarsals, respectively. In order to preserve this wrapping and thus

approximate a more physiologic line of action, an interstitial body was incorporated into each of these structures as was done for the medial and lateral flexor tendons described above in Section 6.5.2-3. In both cases, this body was modeled as a narrow bar approximately 25mm across and initially oriented roughly mediolaterally by inspection. The linear stiffness of the long plantar ligament was derived from the work of Huang et al. while plantar fascia values were taken from the work of Kitaoka et al.; both were in agreement with Iaquinto.<sup>99,129,130</sup>

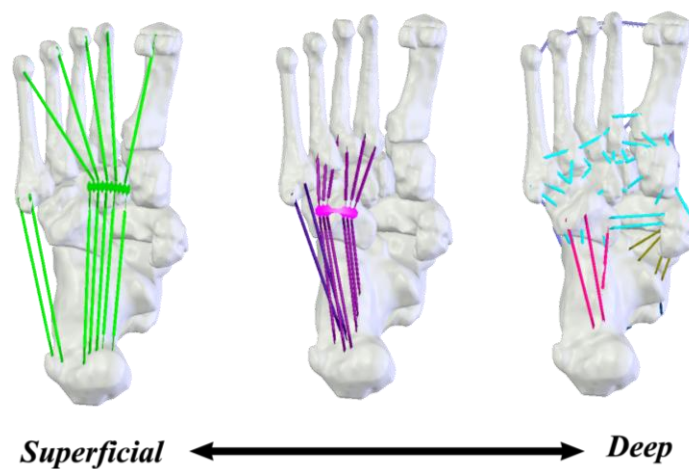


**Figure 6-13: Right foot model showing plantar tissues. LEFT: Plantar Fascia central and lateral bands; MIDDLE: Long Plantar Ligament central and lateral bands; RIGHT: Other short interosseous ligaments.**

### 6.6.2 Mechanical Modeling

The mechanical behavior of each of the 146 soft-tissue elements described above were constrained to tensile only behavior dictated as a function of the elements' published linear stiffness and the straight line element length relative to their resting length. In agreement with the in vitro observations of Song et al. and the modeling work of Iaquinto and Wayne, an initial 4% in situ strain was further imposed on all ligament tissues as an initial estimate of the

physiologic resting tension in the tissues of the unloaded foot and ankle.<sup>4,5,99,131</sup> Thus, the stress free lengths ( $L_0$ ) for all tissues were derived from the bone positions and orientations in the neutrally aligned MRI scan and shortened to reflect that 4% in situ strain value. One caveat to this process was that the ankle collateral ligaments were measured after adjusting the models for neutral plantar/dorsiflexion as described in Section 6.2. The stress free length,  $L_0$ , was therefore defined by

$$L_0 = \frac{L(t_0)}{1 + \varepsilon} \quad (6)$$

where  $L(t_0)$  is the straight line length of any given element in the MRI scan position and  $\varepsilon$  is the desired in situ strain, i.e. 4%. As each of the model simulations progressed, the total strain of the tissue, inclusive of the  $t_0$  in situ strain, was calculated for every time step. Thus, for all  $t > t_0$

$$\Delta L = L(t) - L_0 \quad (7)$$

Finally, a condition of tension only was set for all soft-tissue elements. Thus the generalized discontinuous tension expression for all 146 elements in each model is given in Equation (8).

$$T[L(t)] = \begin{cases} 0, & \Delta L = L(t) - L_0 < 0 \\ 0, & \Delta L = L(t) - L_0 = 0 \\ -S * \Delta L, & \Delta L = L(t) - L_0 > 0 \end{cases} \quad (8)$$

### 6.6.3 FORTRAN Expressions

In order to input the prescribed mechanical soft-tissue behavior into each of the models, COSMOSMotion required that the equations be expressed using the native FORTRAN function set. Therefore, for a given tension element,  $i$ , the passive soft-tissue mechanical behavior

expression was written linearly and adapted using the required operators. The tension in that  $i^{th}$  element was thus:

$$T_i = IF(DM(O_i, I_i) - L_{i,0} : 0,0, -S_i * (DM(O_i, I_i) - L_{i,0}) - 0.15 * VR(O_i, I_i)) \quad (9)$$

where  $O_i$  and  $I_i$  are the origin and insertion of the element, respectively. DM is the FORTRAN operator designating the straight-line distance magnitude. Thus corresponding with Equation (8), the tension in any given element is given by the positive strain beyond  $L_{i,0}$  multiplied by its linear stiffness,  $S_i$ . Strains less than or equal to zero result in zero element tension.

As with the rigid body contact parameters given in Equation (5), an additional damping parameter was included in the FORTRAN expression shown in Equation (9). The term, VR, is the resultant velocity of the two element attachment points relative to one another. This addition was incorporated to address instability in the model caused by the sudden onset of large tensile forces that can cause the models to become unstable at the moment of initial body-body contact. Here, the tension in any element is attenuated as a function of VR, and thus as a function of time.<sup>111,112</sup> The damping coefficient was 0.15 N\*s/mm multiplied times this velocity term in mm/s. It must be noted that while this damping term does add time dependence to the ligaments, it is not meant to reflect in vivo viscoelastic tissue behavior. Indeed, since every element in the model received the same damping coefficient and all models were evaluated only after the simulation reached equilibrium where the relative velocities between any origin/insertion pair trend toward zero, the tension developed in any given element was independent of the damping coefficient used.

## **7. PREOPERATIVE MODEL/PATIENT AGREEMENT**

### **7.1 OVERVIEW**

Once all six rigid-body models were fully assembled, we sought to predict and compare the preoperative kinematics for each of the recruited AAFD patients. In this we chose to confine the scope of our investigation to foot function during stance as this is most amenable to quantification on routinely acquired clinical x-ray. Specifically, we chose to single-leg stance which allows the afflicted arch to drop to the maximum extent possible as allowed by the degree of the patient-specific AAFD affliction. Single-leg stance further prevents the patient from offloading their body weight onto the contralateral side thereby confounding the loading conditions prescribed in the model.

The ultimate goal of this study was to validate our modeling methodology using clinically relevant radiographic measures in three planes. Then to subsequently characterize the nature of the model predictive error as well as test for any bias that may be present.

### **7.2 METHODS**

#### *7.2.1 Tissue Grading*

As prescribed in Chapter 4, the collaborating radiologist, Dr. Cutis Hayes, investigated the MR signal changes of eight tissues known to be affected in AAFD. Briefly, these were the (1) PTT, (2) superomedial and (3) inferomedial bands of the spring ligament, (4) anterior, (5) posterior, and (6) deep bands of the deltoid ligament, the (7) talocalcaneal interosseous



ligaments, and (8) plantar fascia.<sup>55-57,97</sup> Damage to these structures was graded on a four-tier scale adapted from the work of Deland et al and spanned from intact (Grade 0) to severe tears (Grade III) of the tissue.<sup>56</sup>

### 7.2.2 Model Loading

In order to mimic single-leg stance, each model was loaded against a rigid base with the foot in neutral flexion and inversion/eversion as described in Section 6.2. Briefly, this involved applying a patient-specific body weight acting vertically through the tibial plateau. In addition, active muscle contraction was included as fixed tension vectors for five muscles. The Achilles (gastrocnemius/soleus complex), FHL, PL, PB, and FDL tendons were assigned static loads of 50%, 10.5 %, 10%, 8.8%, and 6% of body weight, respectively, in agreement with standing electromyography (EMG) measures and in vivo maximum plantar flexion force.<sup>84,120</sup> [Table 7-1] The PTT was excluded from the models' loading scheme as its dysfunction is the hallmark of Stage IIb AAFD.<sup>56,70,132</sup> Finally, the extrinsic dorsiflexors and the anterior tibialis were excluded from the model given their secondary role in maintaining stance and the lack of supporting EMG data in the literature.

**Table 7-1: Preoperative muscle loading (N) scaled relative to patient BW.**

|          | %BW<br>(# vectors) | Patient # |        |        |        |        |        |
|----------|--------------------|-----------|--------|--------|--------|--------|--------|
|          |                    | P1        | P2     | P3     | P4     | P5     | P6     |
| BW (lbs) |                    | 147.60    | 194.00 | 209.20 | 160.00 | 204.00 | 192.50 |
| BW (N)   |                    | 656.67    | 863.10 | 930.73 | 711.84 | 907.59 | 856.43 |
| Achilles | 50% ( /4)          | 328.33    | 431.55 | 465.36 | 355.92 | 453.80 | 428.21 |
| FDL      | 6.0% ( /4)         | 39.40     | 51.79  | 55.84  | 42.71  | 54.46  | 51.39  |
| FHL      | 10.5% ( /1)        | 68.95     | 90.63  | 97.73  | 74.74  | 95.30  | 89.93  |
| PB       | 8.8% ( /3)         | 57.79     | 75.95  | 81.90  | 62.64  | 79.87  | 75.37  |
| PL       | 10% ( /4)          | 65.67     | 86.31  | 93.07  | 71.18  | 90.76  | 85.64  |

### 7.2.3 Measurements and Validation

Once equilibrated under the applied loading, diagnostic ML, standard AP, and hindfoot views associated with AAFD were recreated within each model. Subsequently, nine angular joint measures often used to characterize flatfoot were compared between the models and their respective patient x-rays and photographs; five in the ML x-ray plane [Figure 7-1], three in the standard AP x-ray plane [Figure 7-2] and one in the hindfoot PA photographic plane.

<sup>36,37,40,42,43,133</sup> Additionally, six distance measures were compared between the patient and model; five in the ML x-ray plane and one in the standard AP x-ray plane. <sup>36,38,39,44,134</sup>

Comparisons of patient radiographic data to published normative and AAFD population means and standard deviations were done using one sided  $z$  tests with differences considered significant for  $p < \alpha = 0.05$ . Two sided  $z$  tests were not used given that the direction of change from normal to AAFD afflicted is well established in the literature and each patient was diagnosed based on their gross clinical presentation of deformity. Thus the probability of detecting a difference in population means in the direction away from AAFD afflicted was minimized. Comparisons between patient radiographic data and model predictions were interpreted using Bland-Altman equity and means-difference plots; maximum expected methodological error was captured by 95% limits of agreement for any given measure. <sup>135</sup>

Goodness of fit of the models are reported in terms coefficients of determination,  $R^2$ , for each measure. Coefficients close to zero suggest the modeling methodology accounts for little of the observed variance between patients and their respective models, while values close to one indicate the methodology is able to predict much of the observed variance. The model predictions were checked for fixed bias relative to their patient-matched observations using one

sample  $t$  tests of the measure deviation against the expected null values; fixed bias was indicated for  $p < 0.05$ . Proportional bias was investigated by linearly regressing the patient and model differences against their means; proportional bias was indicated for  $R_{\text{BIAS}}^2 > 0.5$ .

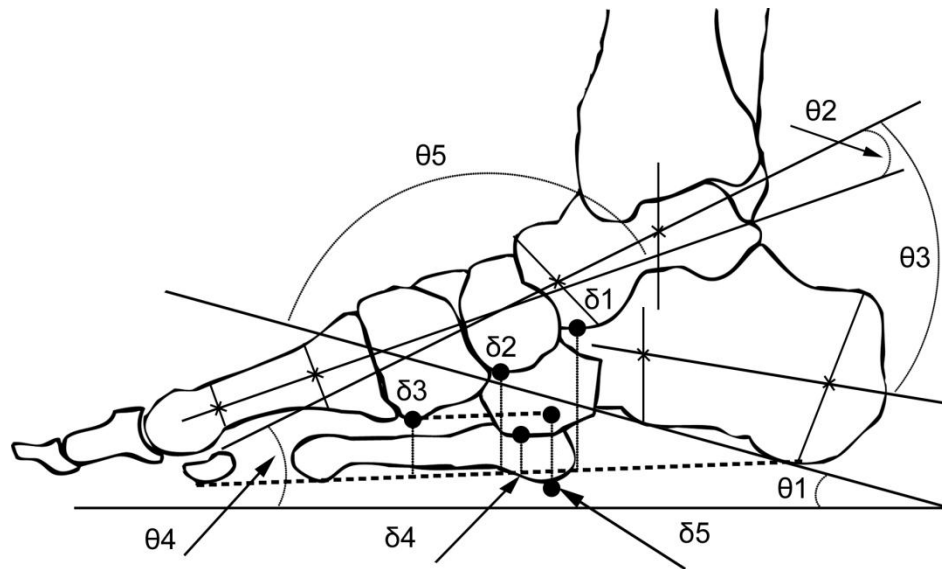


**Figure 7-1: Measurements for ML view. ANGLES:** The calcaneus axis is formed by a line passing through the midpoints of the widest portion of the anterior and posterior aspects. The talar axis is formed by lines connecting the superior most point on the talar dome to the lateral process and across the anterior margins of the talar neck; the axis bisects these two lines. The 1st metatarsal axis is formed by bisecting lines across the width of the proximal and distal diaphysis.<sup>37,40,133</sup>  **$\theta 1$ :** The calcaneal pitch angle (ML-CP) is measured between a line tracing the inferior calcaneal border and the horizontal.  **$\theta 2$ :** The intersection of the talar axis and the 1st metatarsal axis forms the ML talo-1st metatarsal angle (ML-T1MT).  **$\theta 3$ :** The intersection of the talar axis and the calcaneal axis forms the talocalcaneal angle (ML-TC).  **$\theta 4$ :** The talar declination angle (ML-Tdec) is measured between the talar axis and the horizontal.<sup>40,136</sup>  **$\theta 5$ :** Finally, the calcaneal 1st metatarsal

angle (ML-C1MT) is measured between the calcaneal pitch axis and the 1st metatarsal axis.<sup>42</sup> DISTANCES:  $\delta 1$ : Talar height (ML-Tal-h),  $\delta 2$ : navicular height (ML-Nav-h),  $\delta 3$ : 1st cuneiform height (ML-1CN-h), and  $\delta 4$ : cuboid height (ML-Cub-h) were measured from the inferior most point to a line connecting the inferior calcaneus to the medial sesamoid.<sup>36,38,43,44</sup>  $\delta 5$ : The 1st cuneiform to the 5th metatarsal height (ML-1CN/5MT) was measured from the inferior cuboid to the inferior base of the 5th metatarsal.<sup>36,137</sup>

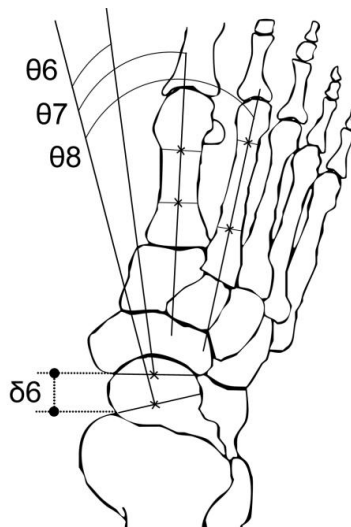


**Figure 7-2: Measurements for standard AP view.** ANGLES:  $\theta 6$ : The talonavicular angle (AP-TN) is measured between the talar and navicular AP axes.<sup>133</sup> These axes are defined as the orthogonal projections of lines spanning the medial and lateral margins of the respective articular surfaces. The axes of the 1st and 2nd metatarsals are by lines bisecting the proximal and distal widths of the diaphyses.<sup>40,42</sup>  $\theta 7$ : The talar 1st metatarsal (AP-T1MT) and  $\theta 8$ : talar 2nd metatarsal angles (AP-T2MT) are formed between the talar axis and the axis of each respective metatarsal. DISTANCES:  $\delta 6$ : The talonavicular uncoverage distance (AP-TNuncov) was measured according to the technique described by

**Chadha as the AP distance separating the medial margins of the talar and navicular articular surfaces.**<sup>137</sup>

## 7.3 RESULTS

### 7.3.1 *Population Characteristics*

All six patients demonstrated MRI signal attenuation of the PTT, though none were observed to have a greater than 50% thickness tear ( $\leq$  Grade II). Further, the anterior deltoid showed the greatest attenuation (avg. 2.0), followed closely by the superomedial and inferomedial spring ligaments (avg. 1.6 and 1.3) in agreement with the observations of Deland et al. and Williams et al. for patients with PTT insufficiency.<sup>56,57</sup> [Table 7-2] The most afflicted patient, based on the sum of all attenuation grades, was Patient #2 (17); the least afflicted patient was Patient #4 (0).

**Table 7-2: Modified four-tiered grading of the MRI signal attenuation investigated. "NV" indicates the tissue could not be visualized. Grade 0 = intact, Grade I = tendinosis without tears, Grade II = observable tear <50% thickness, and Grade III = observable tear >50% thickness.**

| <b>Tissue</b>                      | <b>Patient #</b> |           |           |          |           |          | <b>AVG</b> |
|------------------------------------|------------------|-----------|-----------|----------|-----------|----------|------------|
|                                    | <b>1</b>         | <b>2</b>  | <b>3</b>  | <b>4</b> | <b>5</b>  | <b>6</b> |            |
| Posterior Tibialis Tendon          | 1                | 2         | 2         | NV       | 1         | 2        | <b>1.6</b> |
| Superior Medial Spring Lig.        | 1                | 2         | 3         | NV       | 1         | 1        | <b>1.6</b> |
| Inferior Medial Spring Lig.        | 0                | 3         | 2         | 0        | 2         | 1        | <b>1.3</b> |
| Anterior Deltoid Lig.              | 1                | 2         | 3         | NV       | 2         | 2        | <b>2.0</b> |
| Posterior Deltoid Lig.             | 0                | 2         | 2         | 0        | 2         | 1        | <b>1.2</b> |
| Deep Deltoid Lig.                  | 0                | 2         | 0         | 0        | 1         | 1        | <b>0.7</b> |
| Talocalcaneal Interosseous Lig.    | 0                | 2         | 2         | 0        | 2         | 0        | <b>1.0</b> |
| Plantar Fascia                     | 1                | 2         | 1         | 0        | 0         | 1        | <b>0.8</b> |
| <b>Most Affected Patient (SUM)</b> | <b>4</b>         | <b>17</b> | <b>15</b> | <b>0</b> | <b>11</b> | <b>9</b> |            |

In addition to the graded observations noted in Table 7-2, the collaborating radiologist also noted other radiological changes in the patient sample. These secondary findings included significant edema in the sinus tarsi of two patients (#2,#5), edema at the medial navicular in one patient (#1), and two patients with large accessory navicular bones (Type II) at the PTT insertion site (#5,#6).<sup>25</sup> A large fracture fixation plate on the 5th metatarsal of Patient #4 produced sufficient metal artifact to partially obscure the MR signal in the regions of the distal PTT, anterior deltoid, and superomedial spring ligament. Additionally, this patient was observed to have a previous MCO stemming from a prior foot surgery unrelated to AAFD, though the hardware had been removed.

Patient angular measures were significantly different from published values in normal populations for eight of the nine angles investigated; talar declination was not significantly

different. The largest difference was observed for the ML calcaneal-1st metatarsal angle which was 21.0° larger in our sample. Generally, our sample means were closer to the AAFD population with only two of the nine angles differing significantly from the published values, though ML talo-1st metatarsal angle approached significance. Calcaneal pitch and calcaneal-1st metatarsal angles were significantly different in the direction of increased severity of deformity for our patient sample. [Table 7-3]

**Table 7-3: Patient radiographic angle means compared to published values (stdev).**

**Literature sources indicated by superscripts: <sup>40</sup> Thomas et al. (n=100); <sup>37</sup> Coughlin and Kaz, (n=56 normal, 39 AAFD); <sup>41</sup> Bruyn (n=25); <sup>42</sup> Murley et al. (n=31); <sup>36</sup> Younger et al. (n=21). Significance indicated by \*.**

| Angle Measure<br>(°)            | Patient<br>Sample | Normal<br>Population | Test Against<br>Normal   | AAFD<br>Population | Test Against AAFD       |
|---------------------------------|-------------------|----------------------|--------------------------|--------------------|-------------------------|
| <b>ML-CP</b> <sup>37,40</sup>   | 12.6 (3.5)        | 19.7 (6.5)           | $z = 2.68, p < 0.01^*$   | 16.3 (3.6)         | $z = 2.52, p < 0.01^*$  |
| <b>ML-T1MT</b> <sup>37,40</sup> | 13.2 (8.1)        | 3.3 (4.7)            | $z = 5.16, p < 0.001^*$  | 17.5 (6.4)         | $z = 1.64, p = 0.050$   |
| <b>ML-TC</b> <sup>37,40</sup>   | 34.9 (2.9)        | 45.1 (7.6)           | $z = 3.29, p < 0.001^*$  | 36.2 (30.5)        | $z = 0.11, p = 0.458$   |
| <b>ML-Tdec</b> <sup>40,41</sup> | 26.8 (5.7)        | 25.6 (3.4)           | $z = 0.89, p = 0.186$    | 32.4 (8.3)         | $z = 1.64, p = 0.050$   |
| <b>ML-C1MT</b> <sup>42</sup>    | 153.8 (6.1)       | 132.8 (4.0)          | $z = 12.86, p < 0.001^*$ | 141.7 (6.7)        | $z = 4.42, p < 0.001^*$ |
| <b>AP-TN</b> <sup>37</sup>      | 24.2 (6.1)        | 10.4 (4.2)           | $z = 8.03, p < 0.001^*$  | 22.3 (6.7)         | $z = 0.918, p = 0.179$  |
| <b>AP-T1MT</b> <sup>36,40</sup> | 13.8 (5.9)        | 7.1 (6.6)            | $z = 2.50, p < 0.01^*$   | 12 (10)            | $z = 0.45, p = 0.327$   |
| <b>AP-T2MT</b> <sup>40,42</sup> | 24.1 (4.7)        | 15.6 (7.5)           | $z = 2.77, p < 0.01^*$   | 27.5 (10.2)        | $z = 0.822, p = 0.206$  |
| <b>PA-HFV</b> <sup>37</sup>     | 98.3 (3.7)        | 95 (3)               | $z = 2.70, p < 0.01^*$   | 99 (4)             | $z = 0.424, p = 0.336$  |

All six distance measure means were significantly different from published normative values, with the largest mean difference observed for ML talar height which was 17.5mm shorter in our sample. Only one of the six distance measures was significantly different from published

AAFD means with 1st metatarsal to 5th metatarsal distance being significantly larger. [Table 7-4]

**Table 7-4: Patient radiographic distance means compared to published values (stdev).**

Literature sources indicated by superscripts: <sup>44</sup> Saltzman et al. (n=100); <sup>43</sup> Krans et al. (n=22); <sup>134</sup> Bryant et al, (n=30); <sup>37</sup> Coughlin and Kaz, (n=56 normal, 39 AAFD); <sup>36</sup> Younger et al. (n=21). Significance indicated by \*. NA=Not Available

| Distance Measure (mm)      | Patient Sample | Normal Population | Test Against Normal     | AAFD Population | Test Against AAFD       |
|----------------------------|----------------|-------------------|-------------------------|-----------------|-------------------------|
| ML-Tal-h <sup>44</sup>     | 29.6 (3.8)     | 47 (7)            | $z = 6.10, p < 0.001^*$ | NA              | NA                      |
| ML-Nav-h <sup>43,134</sup> | 20.1 (4.8)     | 31.3 (7.3)        | $z = 3.77, p < 0.001^*$ | 19.0 (6.0)      | $z = 0.429, p = 0.334$  |
| ML-1CN-h <sup>37</sup>     | 13.1 (3.7)     | 19.8 (2.7)        | $z = 6.12, p < 0.001^*$ | 11.4 (4.3)      | $z = 0.94, p = 0.173$   |
| ML-1CN/5MT <sup>37</sup>   | 9.4 (5.8)      | 15.5 (4.0)        | $z = 3.73, p < 0.001^*$ | 4.2 (5.2)       | $z = 2.45, p < 0.007^*$ |
| ML-Cub-h <sup>36</sup>     | 8.5 (2.3)      | 12.0 (3.7)        | $z = 2.34, p < 0.01^*$  | 8.8 (7.2)       | $z = 0.12, p = 0.454$   |
| AP-TN-uncov <sup>36</sup>  | 14.8 (2.0)     | 11.0 (4.0)        | $z = 2.30, p < 0.05^*$  | 16.5 (5.0)      | $z = 0.85, p = 0.197$   |

### 7.3.2 Radiographic Validation - Preoperatively

The average absolute difference observed between the patient and model x-ray angle measures ranged from 1.9° (calcaneal pitch) to 6.7° (AP talo-1st metatarsal angle). The maximum absolute difference in our sample was 15.0° for a single AP talo-1st metatarsal angle. The average absolute difference between the patient and model x-ray distance measures ranged from 1.2mm (1st cuneiform height) to 3.6mm (talar height). The maximum absolute difference in our sample was 10.3mm for a single talar height measure.



Coefficients of determination ( $R^2$ ) between patient and model angular measures ranged from 0.215 to 0.750 for hindfoot valgus and ML talo-1st metatarsal angles, respectively. Further, 95% confidence limits of agreement ranged from  $\pm 5.2^\circ$  (talocalcaneal angle) to  $\pm 10.2^\circ$  (AP talo-1st metatarsal angle).  $R^2$  agreement between patient and model distance measures ranged from 0.174 to 0.885 for talar and navicular heights, respectively. [Table 7-5]

**Table 7-5: Model to Patient agreement for all radiographic measures. Fixed model bias tested using one sample  $t$  tests of differences; significance set at  $\alpha=0.05$ .**

| Measure                     | Avg.  DIFF  (stdev) | Max Diff. | $R^2$ | 95% Limits of Agreement | Fixed Bias? |
|-----------------------------|---------------------|-----------|-------|-------------------------|-------------|
| <b>ML-CP</b> ( $^\circ$ )   | 1.9 (3.1)           | 5.3       | 0.541 | $\pm 5.5$               | -           |
| <b>ML-T1MT</b> ( $^\circ$ ) | 3.8 (6.0)           | -9.0      | 0.750 | $\pm 9.1$               | -           |
| <b>ML-TC</b> ( $^\circ$ )   | 2.2 (3.3)           | -4.9      | 0.289 | $\pm 5.2$               | -           |
| <b>ML-Tdec</b> ( $^\circ$ ) | 2.6 (3.7)           | 5.9       | 0.659 | $\pm 6.7$               | -           |
| <b>ML-C1MT</b> ( $^\circ$ ) | 4.5 (7.3)           | -11.7     | 0.670 | $\pm 9.5$               | -           |
| <b>AP-TN</b> ( $^\circ$ )   | 3.0 (5.4)           | -8.6      | 0.631 | $\pm 7.7$               | -           |
| <b>AP-T1MT</b> ( $^\circ$ ) | 6.7 (5.7)           | 15.0      | 0.443 | $\pm 10.2$              | +6.7        |
| <b>AP-T2MT</b> ( $^\circ$ ) | 3.6 (4.8)           | 8.5       | 0.382 | $\pm 8.8$               | -           |
| <b>PA-HFV</b> ( $^\circ$ )  | 4.0 (5.2)           | -6.6      | 0.215 | $\pm 8.4$               | -           |
| <b>ML-Tal-h</b> (mm)        | 3.6 (6.3)           | 10.3      | 0.174 | $\pm 8.4$               | -           |
| <b>ML-Nav-h</b> (mm)        | 1.4 (3.3)           | 5.6       | 0.885 | $\pm 5.1$               | -           |
| <b>ML-1CN-h</b> (mm)        | 1.2 (2.4)           | 4.0       | 0.846 | $\pm 3.5$               | -           |
| <b>ML-1CN/5MT</b> (mm)      | 3.4 (3.2)           | 6.3       | 0.704 | $\pm 6.2$               | -           |
| <b>ML-Cub-h</b> (mm)        | 2.9 (3.6)           | 5.1       | 0.339 | $\pm 4.4$               | -2.9        |
| <b>AP-TN-uncov</b> (mm)     | 2.7 (3.2)           | 4.7       | 0.293 | $\pm 3.4$               | -2.7        |

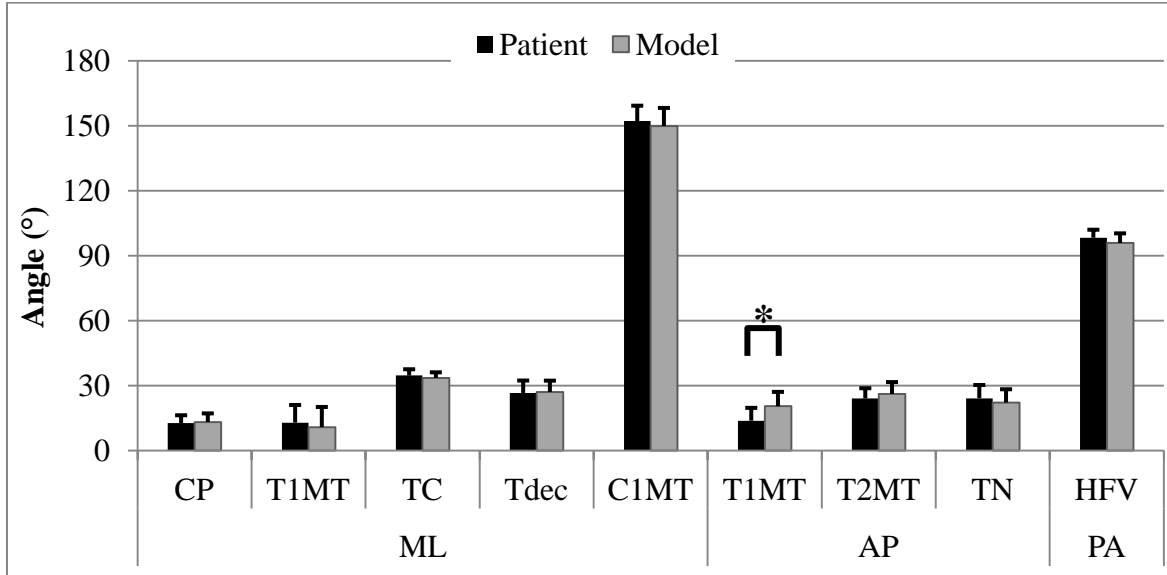


**Figure 7-3: Plot of model mean ANGLE predictions versus patient observations ( $\pm$ stdev). \*:**

**Model prediction demonstrates a fixed bias ( $p < 0.05$ ).**

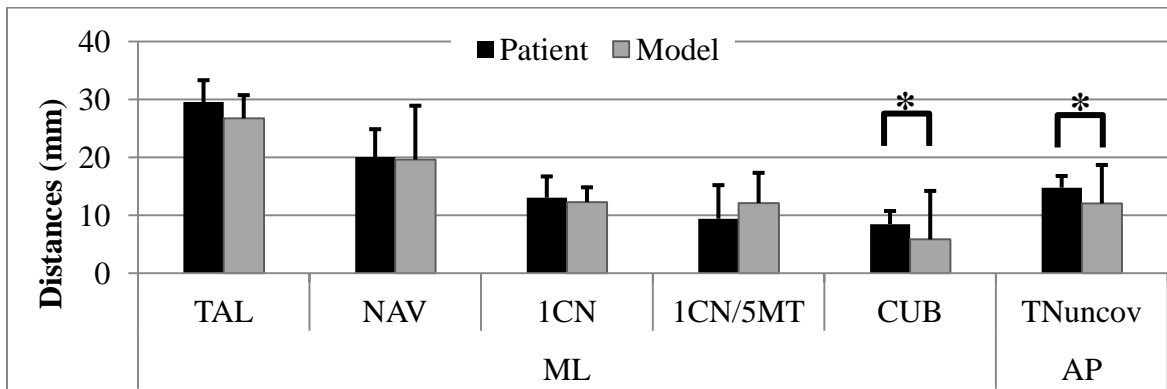


**Figure 7-4: Plot of model mean DISTANCE predictions versus patient observations**

**( $\pm$ stdev). \*: Model prediction demonstrates a fixed bias ( $p < 0.05$ )**

The AP talo-1st metatarsal angle was the only angular measure to reflect a static bias between model and patient measures, with an average absolute model deviation of  $+6.7^\circ$  over patient values. Cuboid height and AP talonavicular uncoverage distance showed statistically significant static bias with the model underestimating patient values, and thereby

underestimating the medial column collapse and forefoot abduction, by an average absolute deviation of -2.6mm and -2.7 mm, respectively. None of the model measures demonstrated any significant proportional bias ( $R^2_{\text{BIAS}} < 0.5$ ). Bland-Altman plots used to visualize correlation ( $R^2$ ) and possible bias is shown for the clinically favored ML talo-1st metatarsal angle (ML-T1MT), talonavicular coverage angle (AP-TN), and 1st cuneiform height (ML-1CN) are shown below.

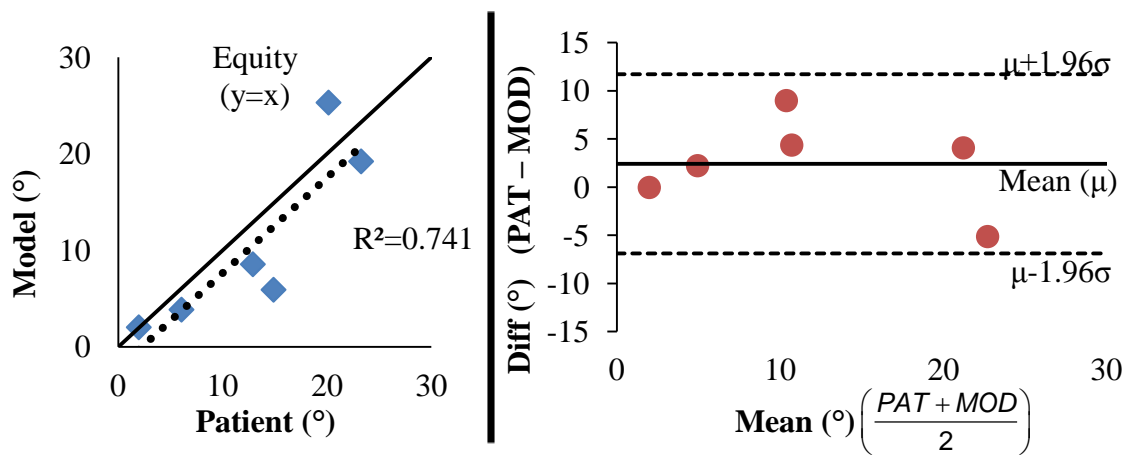


**Figure 7-5: Bland-Altman style equity (LEFT) and mean-difference (RIGHT) plots for the ML talo-1st metatarsal angle (ML-T1MT) measure.**

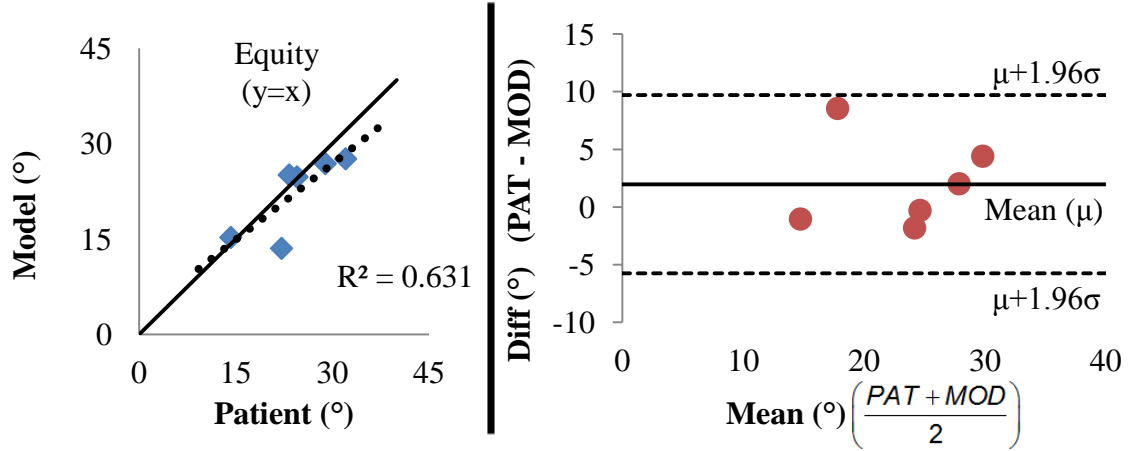


**Figure 7-6: Bland-Altman style equity (LEFT) and mean-difference (RIGHT) plots for the AP talonavicular angle (ML-TN) measure.**

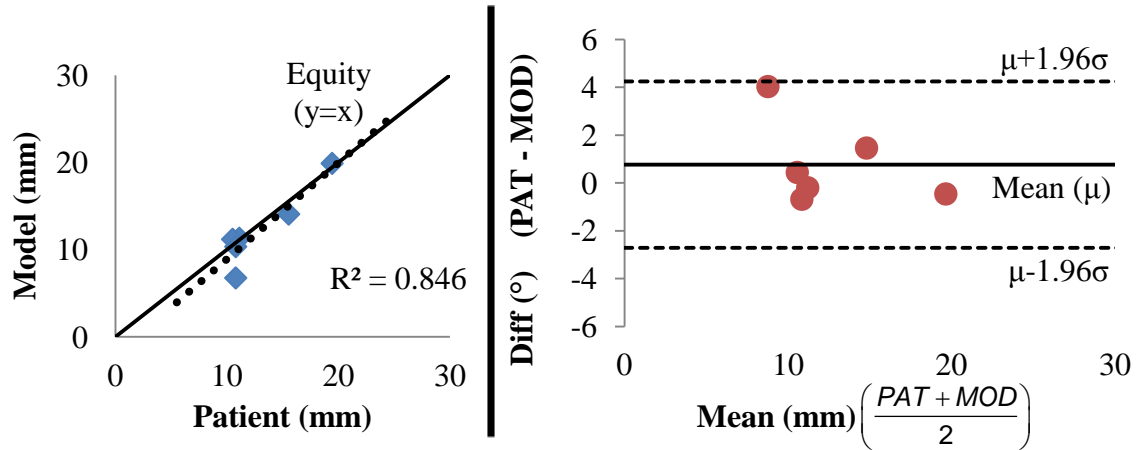


**Figure 7-7: Bland-Altman style equity (LEFT) and mean-difference (RIGHT) plots for the ML 1st cuneiform height (ML-1CN) measure.**

## 7.4 DISCUSSION

The six patients modeled in this study were typical of Stage IIb AAFD sufferers. Radiographically, their joint angles differed from normal<sup>37,40,42</sup> as did their distance measures<sup>36,38,133,137</sup>, and all in the direction of increased AAFD deformity. Conversely, the patient measures were more comparable to AAFD values presented in the literature.

In general, the rigid-body models were able to accurately recreate the position and orientation of the respective patient joints. Model to patient agreement ranged depending on the measure with an average absolute deviation of less than  $7^\circ$  across all angular measures and less than 4mm across all distance measures. The angular measure with the best agreement ( $R^2=0.75$ ), the ML talo-1st metatarsal angle, is of particular interest as numerous authors have noted that increases in this angle are a sensitive x-ray indicator of decreasing medial arch height and the most diagnostic measure of flatfoot in the ML view.<sup>36,37</sup> Admittedly, since this measure relies on the axes of two discrete mobile bodies, it would be possible for the models to demonstrate high correlation without being particularly accurate in the absolute orientation of either bone. However, the less confounded talar declination angle, which uses the fixed horizontal as a reference, also had moderate to strong correlation ( $R^2=0.66$ ), indicating that the absolute orientations of the model tali were indeed similar to the patients. The most robust distance measure ( $R^2=0.89$ ) was the navicular height, closely followed by the first cuneiform height ( $R^2=0.85$ ). These observations indicate that the model mimicked the patient deformity in both orientation and magnitude of medial column deformity in agreement with clinically relevant radiographic measures.<sup>38,133</sup>

In the standard AP view, the talo-navicular coverage angle exhibited the greatest model to patient agreement ( $R^2=0.63$ ). Again, the robustness of this measure is of interest as the talo-navicular coverage angle is often cited as a sensitive indicator of valgus deformity in the AP plane, though it is less reliably measured between observers.<sup>36,37,39</sup> Interestingly, the closely related talonavicular uncoverage distance showed much less robust agreement ( $R^2=0.293$ ) as well as a model static bias of -2.7mm from patient values.

Unexpectedly, the least correlated angular measure between model and patient was noted for the hindfoot valgus angle ( $R^2=0.22$ ), one of the most clinically apparent manifestations of AAFD.<sup>37,69,70</sup> We believe that the source of much of this apparent incongruity stems from our use of hindfoot photographs as x-ray analogues in the posteroanterior view. By using photographs, the true sagittal axis of the posterior calcaneus was obscured by soft-tissue and not as readily registered to the bony solid models. While, this was a necessary concession given the radiopacity of the anterior foot obscures posteroanterior x-rays, it is nonetheless a source of error for this measure. Further, this angle only differs by  $<5^\circ$  between normal and AAFD populations.

The most significant weakness of this study is the small sample size. This led to low statistical power and an over sensitivity of the coefficients of determination to the magnitude of any single observation. The effect of this is apparent in the wide 95% confidence intervals observed for even well-correlated measures. Nonetheless, the measure standard deviations in our patient sample were very similar to those reported for much larger AAFD patient populations indicating our sample had similar variance to these published works. Another source of error in our study are the radiographic parameters themselves. Specifically, some authors have noted poor to mediocre inter- and intra-observer variability in identifying certain bony landmarks used to define the axes of bones in the foot.<sup>36</sup> The ambiguity of these features was especially apparent in the standard AP view, where the axes of the talus and navicular relied on just two points at the thin margins of the articular surface.<sup>36,37,133</sup> Very small changes in the position of these reference points had large effects on the measure in contrast to axes that were defined by four or more reference points, such as the axes of the metatarsals or calcaneus. A possible solution to this problem would be to compare model predictions to 3-D bony positions and

orientations using biplane fluoroscopy or weight-bearing computed tomography. While either technology could provide more confidence in the accuracy of patient measures than 2-D x-rays, both are cost intensive, incur higher radiation exposure levels, and are not commonly collected during the diagnosis of AAFD.

Additionally, a consequence of our sub-millimeter scan resolution was a reduction in the MR field of view such that the phalanges were not captured for all of patients and were thus excluded from our models. We believe this to be an acceptable approximation given the limited toe loading observed during quiet stance. Indeed, in our own assessment of plantar pressures using digital pedobarography for these six patients, less than 2.5% of body weight was attributed to toe loading.<sup>138</sup> Finally, assumptions were made regarding the soft-tissue loading and properties that would likely affect the model position and subsequently the angles and distances reported. With respect to tendon loading, the anterior tibialis, the extrinsic dorsiflexors, as well as all of the intrinsic muscles of the foot were neglected from the model. These omissions primarily reflect the paucity of EMG data in the literature from which normalized stance loading could be extrapolated. Yet, while anterior tibialis in particular would have an apparent inverting effect on the foot, the smaller intrinsic muscles would likely not impact the measures investigated as they tend to act synergistically with larger, more activated, muscles that are represented in our models. The deformable metatarsal and heel pads were also excluded from the models. While these fatty tissues are very low modulus compared to the bony, ligamentous, and tendinous soft-tissues of the foot, their contributions to the relative heights of the calcaneus and metatarsal were compensated for using small risers on the rigid base under the calcaneus. The heights of these risers were derived from the difference in heel and metatarsal pad

thicknesses as viewed in the patient-specific standing ML radiographs. Finally, all ligaments are represented by linearly elastic passive tension elements. We believe this to be a valid approximation of in vivo ligament function as normal weight-bearing should produce loads within the linear portion of the ligaments' functional range, though we appreciate that ligaments under very low physiological strain may experience nonlinear behavior in the toe region of the tissues' stress-strain curve.

In conclusion, we were able to demonstrate good agreement in the angles and distances predicted by our computational rigid-body models constrained only by joint contact and anatomic soft-tissue elements relative to their patient-matched controls. In particular, these models showed very good predictive power for the clinically favored talo-1st metatarsal angle, navicular height, and medial cuneiform height in the ML view, as well as the talonavicular coverage angle in the standard AP plane. Thus, we believe this methodology offers a promising avenue for predicting in vivo kinematic function for patients with AAFD. Future refinement of these models and validation beyond plane x-ray may allow for non-invasive investigation of physiologic parameters such as joint contact force and soft-tissue strain that are difficult or impossible to measure clinically.



## **8. POSTOPERATIVE MODEL/PATIENT AGREEMENT**

### **8.1 OVERVIEW**

Following initial model validation of the preoperative state, we sought to use the model cohort to predict the postoperative kinematics of the five AAFD patients available for follow up in order to quantify the effects of surgical correction in each patient. Here again, each model was loaded according to patient-specific body weight, extrinsic muscle loading, and passive soft-tissue constraints; however, each postoperative model also included an FHL tendon transfer and patient-specific MCO. Each model's radiographic measurement predictions were again compared to their respective patient. In addition to this, the plantar force changes resulting from surgical correction were also compared between patient and model.

Thus, the objective of the postoperative analysis was to again validate our modeling methodology, this time to the postoperative state, while further investigating the surgical effects on the kinematics of the AAFD afflicted foot. In addition, we also sought to investigate alterations in biomechanical parameters known associated with AAFD, including medial and plantar soft-tissue strain, medial and lateral column joint contact force, and plantar force contours.

## 8.2 METHODS

From the radiographic angle and distance analyses discussed in Chapter 7, it was noted that the cohort demonstrated preoperative radiographic pathology that was significantly different from normal in eight of nine angular measures and six of six distance measures.<sup>22</sup> These significant deviations included decreased calcaneal pitch and talocalcaneal angles, increased talo-1st metatarsal angle in both the ML and standard AP views, increased talonavicular coverage angle, and decreased medial column height measured at the navicular and 1st cuneiform. Further, these deviations from normal were all in the direction of increased flatfoot deformity and representative of published radiographic AAFD populations.

All six patients received a PTT augmentation through FHL tendon transfer to the navicular tuberosity combined with distal tenodesis to the FDL, a Strayer gastrocnemius recession, and an MCO in accordance with accepted surgical practice. Postoperatively, all patients were fit with a non-weight bearing cast for six weeks, followed by a cam boot or walking cast for an additional six weeks.

### 8.2.1 *X-ray and Plantar Force Data Collection*

In order to characterize foot function before and after surgical correction, the patients were imaged preoperatively using MRI, and both pre- and postoperatively using plane film x-ray, and plantar force measurements as described in Chapter 4. Furthermore, the same x-ray protocol described in Chapter 7 was again used to characterize the postoperative state. Briefly, this consisted of two radiographs of the foot taken with the patient in single-leg stance; one in the ML and a second in the AP view. Subsequently, eight angular joint measures used to characterize flatfoot were compared between the models and their respective patient x-rays; five

in the ML plane [Figure 8-1] and three in the standard AP plane [Figure 8-2].<sup>36,37,40,42,43,133</sup>

Additionally, six distance measures were also compared between the patient and model; five in the ML plane and one in the standard AP plane.<sup>36,38,39,44,134</sup>

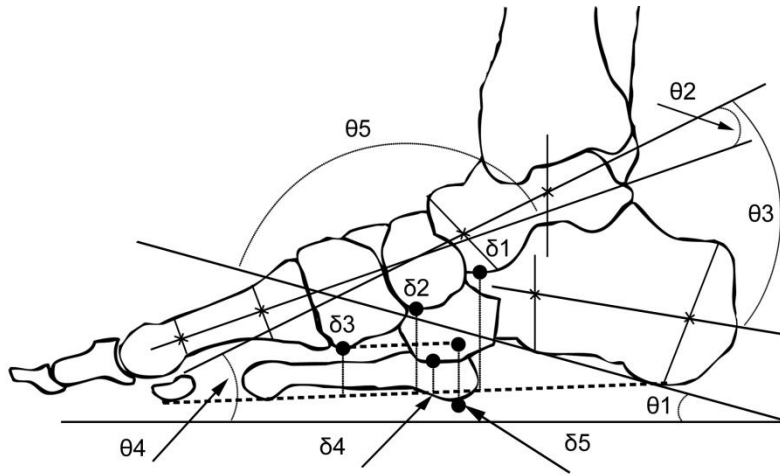


**Figure 8-1: Measurements for ML view. ANGLES:  $\theta 1$ : ML-CP;  $\theta 2$ : ML-T1MT;  $\theta 3$ : ML-TC;  $\theta 4$ : ML-Tdec; and  $\theta 5$ : ML-C1MT.<sup>40,42</sup> DISTANCES:  $\delta 1$ : ML-Tal-h;  $\delta 2$ : ML-Nav-h;  $\delta 3$ : ML-1CN-h;  $\delta 4$ : ML-Cub-h; and  $\delta 5$ : ML-1CN/5MT.<sup>36,38,40,43,44</sup>**

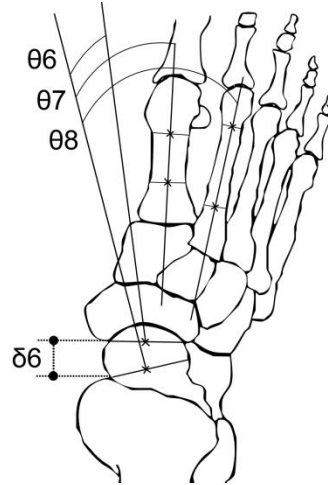


**Figure 8-2: Measurements for standard AP view. ANGLES: 06: AP-TN; 07: AP-T1MT; 08: AP-T2MT. <sup>40,42,133</sup> DISTANCES: 06: talonavicular uncoverage distance. <sup>137</sup>**

One alteration from the earlier protocol was the omission of the hindfoot valgus angle (09). This was the only measure derived from photographs and was excluded from analysis given the difficulty in identifying the patient calcaneal axis and the subsequently poor agreement between patient observations and model predictions.

Finally, MCO translation magnitudes were measured postoperatively through an oblique posteroanterior x-ray focused at the calcaneus and corrected for magnification as described by Saltzman et al.<sup>94</sup> [Figure 8-5]

As described in Section 4.3, plantar force contours were captured for each patient during quiet stance. Once captured, each plantar force profile was averaged over the entire ten second collection window and masked into three discrete regions of loading for each trial. <sup>138</sup> [Figure 8-3] The three regions were created by first dividing the anteroposterior length of the foot at the posterior margin of the 5th metatarsal as visualized on the ML x-ray. The anterior foot,

exclusive of the toes, was subdivided into medial (1) and lateral (2) regions by a line bisecting the metatarsal and heel widths at their widest points. The hindfoot (3) region was thus inclusive of all loading posterior to regions 1 and 2. [Figure 8-4]

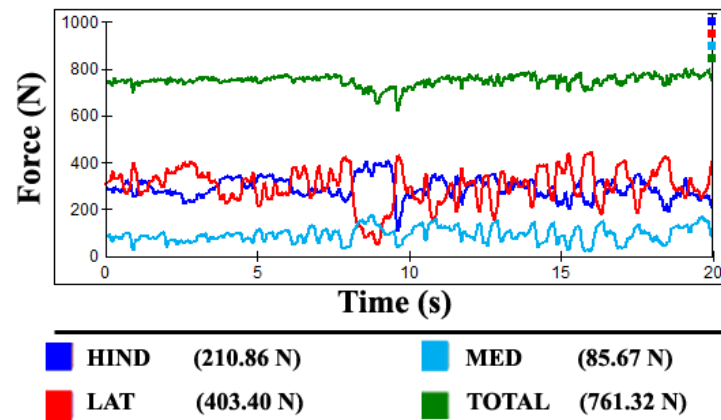


**Figure 8-3: Example of plantar force profile obtained from HRMat® software.**

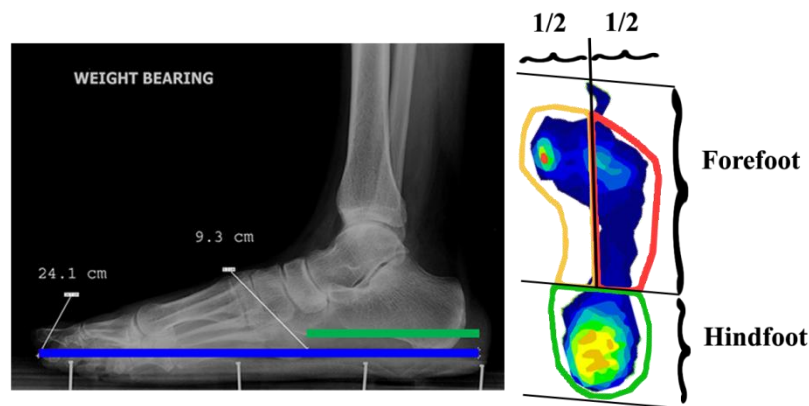


**Figure 8-4: Creation of three region plantar force mask. LEFT: Patient matched ML x-ray used to identify forefoot-hindfoot separation. RIGHT: Medial forefoot (Region 1, GOLD); Lateral forefoot (Region 2, RED); Hindfoot (Region 3, GREEN).**

### 8.2.2 *Model Creation and Loading*

Foot function was investigated through our cohort of five patient-specific computational models developed previously.<sup>22</sup> Briefly, these models were created by first recreating patient bony anatomy in silica, as acquired through MRI and processed in the medical image processing package MIMICS 14.1. Herein, all bones of the foot and ankle, excluding the phalanges, were separated from the surrounding soft-tissues and exported as discrete solid-bodies to the CAD software package SolidWorks as done previously.<sup>4,5,100</sup> All bones were constrained only by physiologic joint contact, ground contact, and soft-tissue influence; no idealized joints or motions were imposed. The COSMOSMotion rigid-body solver was used to prescribe soft-tissue constraints indicative of passive ligament tension, active muscle contraction through the FDL, FHL, PL, PB, and Achilles tendons, and full axial body weight for each patient-specific model. Ligamentous function was dictated by tissue length, linear stiffness, and in situ strain during stance with properties derived from patient-specific anatomy, previous dissection, and published anatomic literature.<sup>25,27,28,127,128,139,140</sup> For the eight tissues graded by the radiologist, observed degeneration was incorporated as a proportional loss in stiffness as done previously.<sup>4,5,22</sup> The relative level of attenuation was not altered from the preoperative assessment of the tissues under the assumption that there would not be any significant tissue reorganization in the short postoperative follow up period, though a second MRI was not performed to verify this assumption.

**Table 8-1: Postoperative loading (N) applied to each of the muscles scaled relative to patient BW along with the change over preoperative loading.**

|                      | %BW<br>(# vectors) | Patient # |    |         |         |         |         |
|----------------------|--------------------|-----------|----|---------|---------|---------|---------|
|                      |                    | P1        | P2 | P3      | P4      | P5      | P6      |
| BW (lbs)             |                    | 164.40    |    | 208.80  | 164.20  | 222.60  | 211.00  |
| BW (N)               |                    | 731.29    |    | 928.79  | 730.52  | 990.17  | 938.58  |
| $\Delta$ from PreOp. |                    | (+11.4%)  |    | (-0.2%) | (+2.6%) | (+9.1%) | (+9.6%) |
| Achilles             | 50% ( /4)          | 365.64    |    | 464.39  | 365.26  | 495.09  | 469.29  |
| FDL                  | 6.0% ( /4)         | 43.88     |    | 55.73   | 43.83   | 59.41   | 56.31   |
| FHL                  | 10.5% ( /1)        | 76.79     |    | 97.52   | 76.70   | 103.97  | 98.55   |
| PB                   | 8.8% ( /3)         | 64.35     |    | 81.73   | 64.29   | 87.14   | 82.59   |
| PL                   | 10% ( /4)          | 73.13     |    | 92.88   | 73.05   | 99.02   | 93.86   |

To model the surgical correction, patient-specific MCO displacements (average 4.7mm, range 4.5-6mm) were incorporated into each model. FHL tendon transfer was modeled by reassigning the tendon insertion to the inferior navicular tuberosity at the opening of the osseous tunnel created surgically and visualized on ML and AP x-ray. The Strayer gastrocnemius lengthening procedure acts to reduce the passive tension of the Achilles tendon and is not designed to alter the course or strength of the activated muscle, as a consequence, the Achilles tension elements were unchanged from the preoperative state for all postoperative runs.

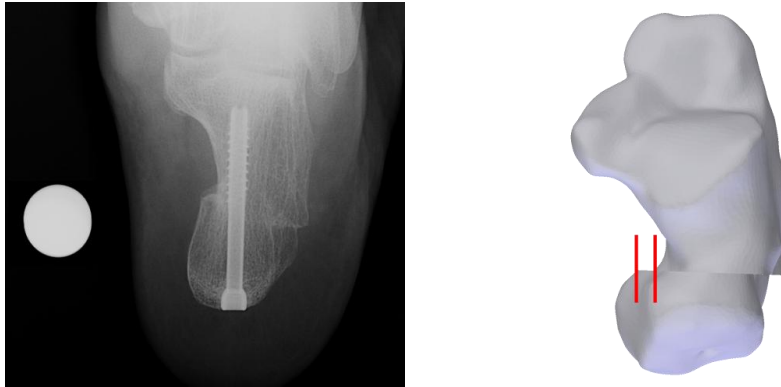


**Figure 8-5: Creation of patient-specific MCO. LEFT: Saltzman view of MCO with nickel for scale. RIGHT: Creation of MCO in model.**

After equilibrating under the prescribed loading, the ML and AP x-ray views were recreated in each model to allow measurement of eight angular and six distance measures recorded for the respective patient as done previously.<sup>22</sup>

Ground contact force was recorded for the calcaneus and five metatarsals and segmented into medial (1st and 2nd metatarsal contacts), lateral (3rd-5th metatarsal contact), and hindfoot (calcaneal contact) regions for comparisons to patient plantar force measures. Once each model reached equilibrium, these forces were averaged across roughly 200 frames (~2 seconds) of simulation time in order to provide an accurate representation of the load.

Additionally, strain in the deltoid ligament, spring ligament, and plantar fascia were tracked in each model. Joint contact force in the models for the talonavicular, navicular-1st cuneiform, and calcaneocuboid joints was also recorded pre- and postoperatively to investigate changes in load distribution through the medial and lateral columns of the foot.



### 8.2.3 *Measurements and Validation*

Model agreement to postoperative radiographic measures was analyzed in terms of coefficients of determination,  $R^2$ , as well as 95% limits of agreement for any given measure.

<sup>135</sup> The data were checked for the presence of fixed bias, indicating the model had a systemic over/under estimation of a parameter, and proportional bias, indicating the level of disagreement was dependent on the magnitude of the observation, in accordance with the methods described by Bland and Altman as used previously.<sup>22,135</sup> Fixed bias was tested using one-sample  $t$  tests of the patient-model differences against the expected null values; significance was reported for  $p < \alpha = 0.05$ . Proportional bias was tested by linearly regressing the differences against their average; significant proportional bias was assumed for  $R_{\text{BIAS}}^2 > 0.5$ .<sup>135</sup>

To examine the effect of surgical correction for both the patients and models, all measures including x-ray, ground contact force, joint contact force, and ligament strain, were compared between the preoperative and postoperative states with 2-sided paired  $t$  tests without assumptions of equal variance; significance was reported for  $p < \alpha = 0.05$ .

Additionally, patient self-reported satisfaction within the cohort was quantified by E. Matheis, M.S. in a companion study to this modeling work. This adjacent analysis was performed using the widely employed Foot and Ankle Outcome Score (FAOS) questionnaire and the Short Form general health survey (SF-36) questionnaire.<sup>138</sup> Briefly, the FAOS questionnaire is specific to foot and ankle function and is designed to characterize the patients' self-reported pain, difficulty with activities of daily living, and overall quality of life. The SF-36 is not tissue specific and is instead designed to give an overall assessment of physical and mental health.

Both questionnaires were administered to the patient cohort before and after their surgical corrections, with mean changes in scores used to assess patient satisfaction.

### 8.3 Results

#### 8.3.1 Radiographic Validation - Postoperatively

The average absolute difference observed between the postoperative patient and model x-ray angles ranged from 1.7° (calcaneal pitch) to 4.3° (AP talo-1st metatarsal angle). The maximum absolute difference in our sample was 11.4° for a single AP talo-1st metatarsal angle. [Figure 8-6] The average absolute difference between the patient and model x-ray distance measures ranged from 1.3mm (talonavicular uncoverage distance) to 3.8mm (1st cuneiform to 5th metatarsal distance). The maximum absolute difference in our sample was 8.7mm for a single talonavicular uncoverage distance measure. [Figure 8-7] There were no significant differences between the model and patient groups postoperatively ( $p>0.05$ ).

The patient cohort changes in x-ray angular measures following surgical correction were generally small to moderate and ranged from an average of -0.3° (ML talo-1st metatarsal) to -4.9° (talonavicular coverage angle). [Figure 8-6] Average cohort changes in x-ray distance measures were likewise small to moderate and ranged from -0.1mm (1st cuneiform height) to -2.8mm (talonavicular uncoverage distance). [Figure 8-7] Across all radiographic measures tracked pre- and postoperatively, only calcaneal-1st metatarsal angle showed a statistically significant change for the cohort ( $p<0.05$ ) though talonavicular coverage angle approached significance ( $p=0.059$ ).

Model changes in x-ray angular measures were similarly small and ranged from an average of -0.6° (calcaneal pitch) to -1.6° (talocalcaneal angle). Average changes in model x-ray

distance measures were again modest and ranged from -0.1mm (talar height) to -0.6mm (talonavicular uncoverage distance). For the model cohort, no measure showed a statistically significant change pre- to postoperatively.

Coefficients of determination ( $R^2$ ) between patient and model angular measures ranged from 0.434 to 0.921 for AP talo-2nd metatarsal and ML calcaneus-1st metatarsal angles, respectively. Further, 95% confidence limits of agreement ranged from  $\pm 4.9^\circ$  (calcaneal pitch) to  $\pm 10.3^\circ$  (talar declination).  $R^2$  agreement between patient and model distance measures ranged from 0.113 to 0.983 for talonavicular uncoverage distance and cuboid height, respectively. [Table 8-2] AP talo-1st metatarsal angle and ML cuboid height demonstrated fixed biases of  $+5.2^\circ$  and -4.0mm, respectively, consistent with the preoperative comparisons investigated previously.<sup>22</sup> However, unlike preoperative comparisons, talar declination angle and cuboid height showed statically significant proportional bias with negative correlations observed between the patient-model differences and their means. [Table 8-2]

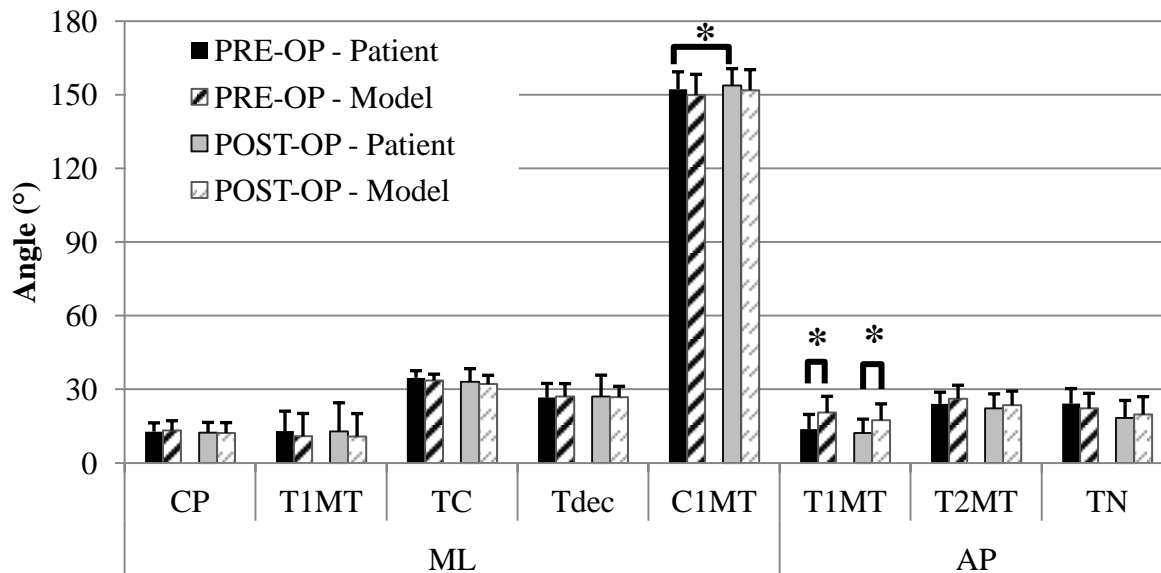


**Figure 8-6: Average x-ray angles for the patient (solid bars) and the model (hashed bars) pre- (black) and postoperatively (gray). \*:  $p < 0.05$**

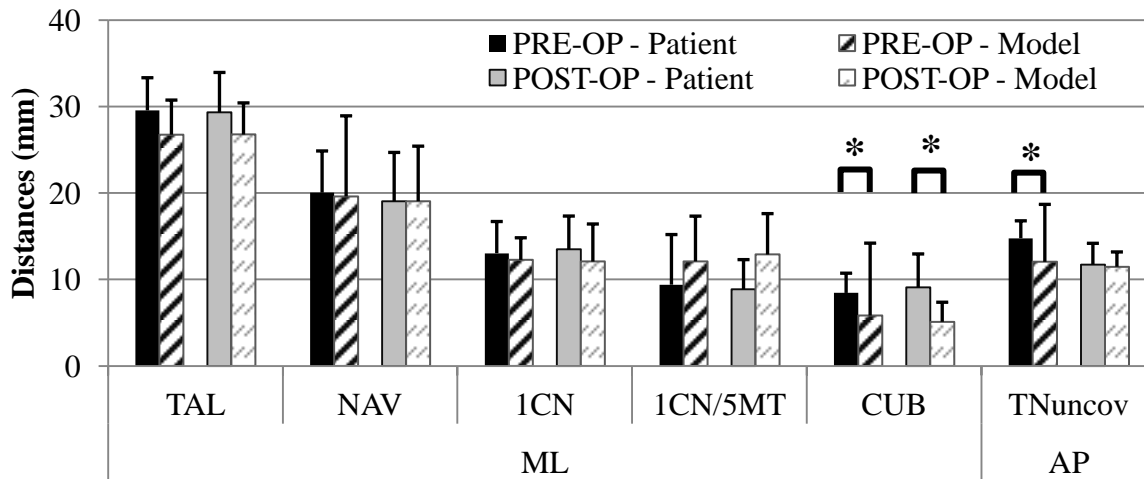


**Figure 8-7: Average x-ray distances for the patient (solid bars) and the model (hashed bars) pre- (black) and postoperatively (gray). \*:  $p < 0.05$**

**Table 8-2: Model to Patient agreement for all postoperative x-ray measures. Fixed model bias tested using one sample t tests of observed differences against expected null values; significance set at  $\alpha>0.05$ . Proportional model bias tested using by regressing the patient-model differences (d) against their mean value ( $\mu$ ); significance set at  $R_{BIAS}^2>0.5$ .**

| Measure          | Avg.  DIFF  (stdev) | Max Diff. | R <sup>2</sup> | 95% Limits of Agreement | Fixed Bias? | Prop. Bias?                          |
|------------------|---------------------|-----------|----------------|-------------------------|-------------|--------------------------------------|
| ML-CP (°)        | 1.7 (2.5)           | 3.6       | 0.682          | ±4.9                    | -           | -                                    |
| ML-T1MT (°)      | 2.5 (5.9)           | -9.9      | 0.852          | ±9.3                    | -           | -                                    |
| ML-TC (°)        | 2.1 (3.1)           | -4.2      | 0.734          | ±5.8                    | -           | -                                    |
| ML-Tdec (°)      | 3.2 (5.5)           | 9.0       | 0.783          | ±10.3                   | -           | d=0.69 $\mu$ , R <sup>2</sup> =0.715 |
| ML-C1MT (°)      | 1.9 (3.7)           | -6.0      | 0.921          | ±5.2                    | -           | -                                    |
| AP-TN (°)        | 2.4 (3.5)           | -5.7      | 0.756          | ±7.2°                   | -           | -                                    |
| AP-T1MT (°)      | 4.3 (4.7)           | 11.4      | 0.616          | ±8.1                    | +5.2        | -                                    |
| AP-T2MT (°)      | 3.4 (4.5)           | 6.7       | 0.434          | ±9.5                    | -           | -                                    |
| ML-Tal-h (mm)    | 2.6 (4.6)           | 7.0       | 0.413          | ±7.1                    | -           | -                                    |
| ML-Nav-h (mm)    | 2.9 (3.9)           | 4.5       | 0.566          | ±8.4                    | -           | -                                    |
| ML-1CN-h (mm)    | 2.1 (3.2)           | 4.5       | 0.587          | ±5.6                    | -           | -                                    |
| ML-1CN/5MT (mm)  | 3.8 (4.3)           | 8.7       | 0.228          | ±8.5                    | -           | -                                    |
| ML-Cub-h (mm)    | 3.3 (3.9)           | 5.4       | 0.983          | ±3.2                    | -4.0        | d=0.52 $\mu$ , R <sup>2</sup> =0.948 |
| AP-TN-uncov (mm) | 1.3 (2.9)           | 4.9       | 0.113          | ±4.7                    | -           | -                                    |

### 8.3.2 Plantar Force Validation

Preoperative patient plantar forces averaged 16.3%, 26.4%, and 57.3% BW for the medial forefoot (1), lateral forefoot (2), and hindfoot regions, respectively. Following surgery, the average changes relative to BW were -6.4%, +7.8%, and -1.4% for the medial forefoot (1),

lateral forefoot (2), and hindfoot regions, respectively. These changes were not statistically significant, (medial forefoot:  $p=0.11$ , lateral forefoot:  $p=0.12$ , hindfoot:  $p=0.84$ ).

The preoperative model plantar force predictions averaged 19.3%, 23.9%, and 57.0% for the medial forefoot (1), lateral forefoot (2), and hindfoot regions, respectively. Following modeled surgical corrections, all three regions demonstrated statistically significant changes ( $p<0.01$ ). The average changes relative to BW were -3.4%, +5.8%, and -2.6% for the medial forefoot (1), lateral forefoot (2), and hindfoot regions, respectively. [Figure 8-8]

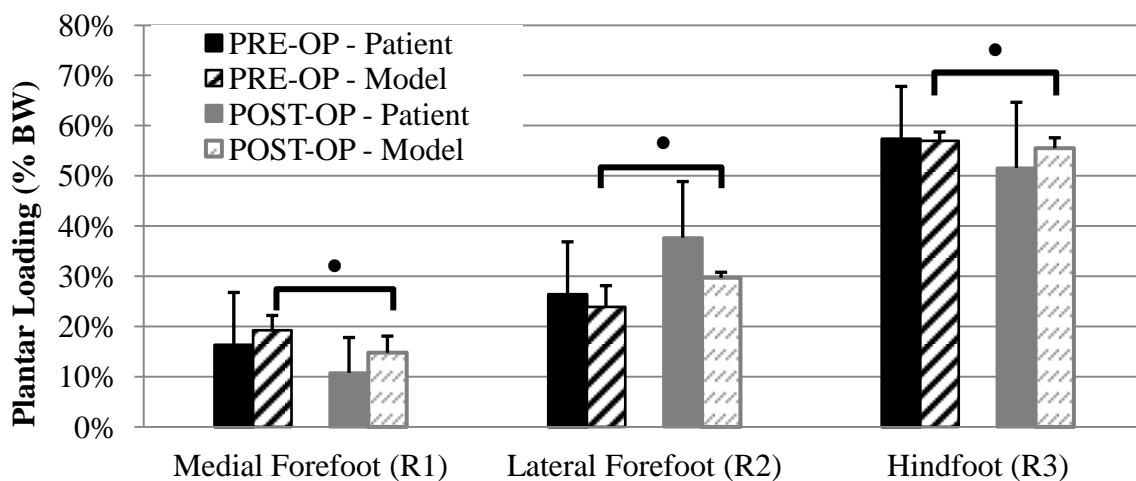


**Figure 8-8: Changes in patient (solid bars) and model (hashed bars) plantar force loading before (black bars) and after (gray bars) surgical AAFD correction. •:  $p<0.01$**

### 8.3.3 Soft-tissue Strains and Joint Contact Force

Strains in the spring ligament were reduced by the surgical procedures an average of 2.7%, 3.1%, and 2.8% relative to their stress-free length for the superomedial, middle, and inferomedial bands, respectively. These changes approached, but did not reach, significance, ( $p=0.09$ ,  $p=0.08$ ,  $p=0.09$ ). The tibionavicular, tibiospring, and tibiocalcaneal bands of the deltoid

likewise saw reductions in strain relative to their stress-free length equal to 0.9%, 0.9%, 0.6%, respectively, though these changes were not statistically significant. The plantar fascia demonstrated the smallest changes in strain of the tissues investigated. Of the five bands used to span the width of the tissue, the medial two bands demonstrated average decreases of <0.2% while the lateral two bands showed increases of <0.5% relative to their stress-free lengths. The central band increased by an average of 0.4% and was the only change to show significance ( $p<0.01$ ). [Figure 8-9]

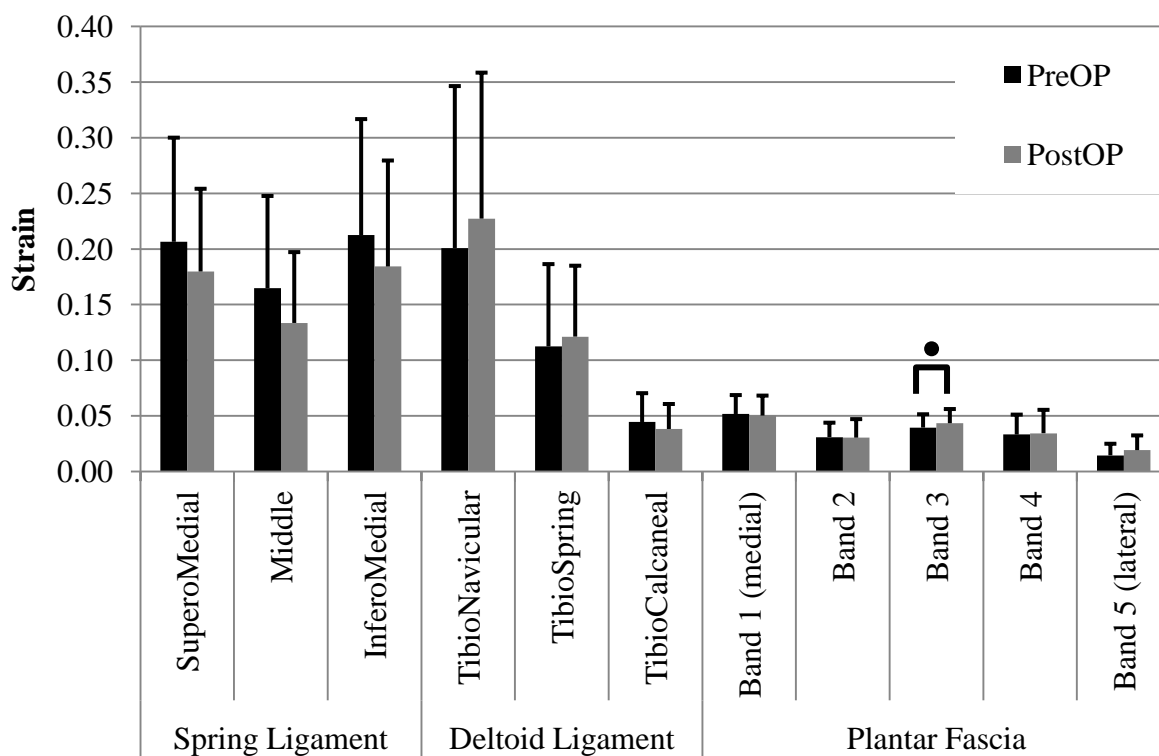


**Figure 8-9: Changes in model soft-tissue strains before (black) and after (gray) surgical AAFD correction. \*:  $p<0.01$**

Finally, following surgical correction, the talonavicular, navicular-1<sup>st</sup> cuneiform, and calcaneocuboid joints demonstrated average changes in joint contact load of -18.8N, -62.2N ( $p<0.5$ ), and +116.5N ( $p<0.01$ ), respectively. [Figure 8-10] When scaled relative to the patient-specific preoperative BW, significant changes in navicular-1<sup>st</sup> cuneiform and calcaneocuboid joint load remained with an average of -7.5% BW ( $p<0.01$ ) and +14.9% BW ( $p<0.01$ ), respectively.

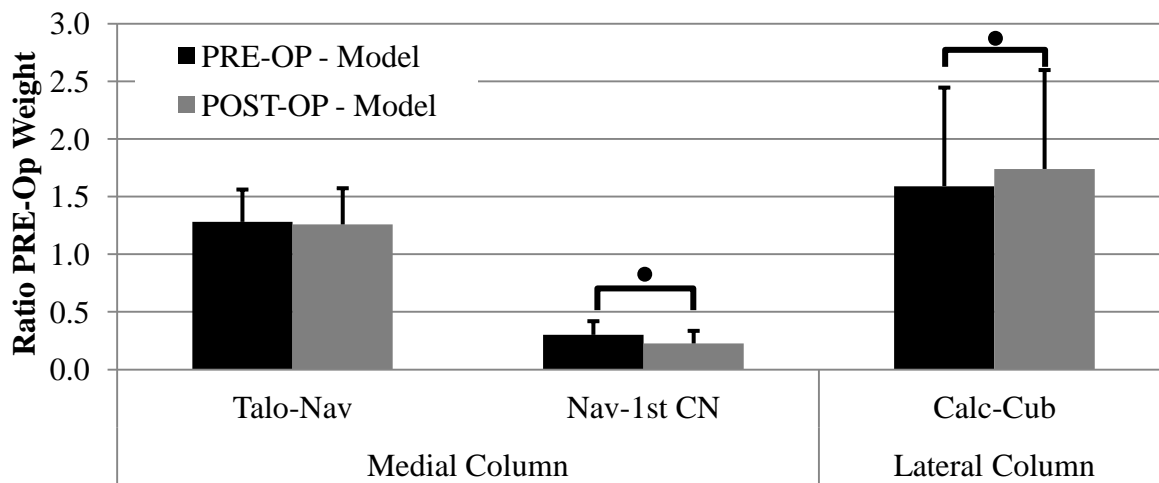


**Figure 8-10: Changes in model medial and lateral column joint contact, normalized to preoperative body weight following surgical AAFD correction. Preoperative shown in black; postoperative shown in gray. •:  $p<0.01$**

#### 8.4 DISCUSSION

This study presents postoperative validation of a cohort of rigid-body models against fifteen clinically relevant radiographic measures and plantar force measures as well as analysis of the effect of surgical correction. Model to patient radiographic agreement was generally very good with average absolute deviations of  $<5^\circ$  across all angular measures and  $<4\text{mm}$  across all distance measures. The best correlated angular measures were the calcaneus-1<sup>st</sup> metatarsal angle



( $R^2 = 0.921$ ), ML talo-1<sup>st</sup> metatarsal angle ( $R^2 = 0.852$ ), and the talonavicular coverage angle ( $R^2 = 0.756$ ). These measures are among the most clinically utilized measures for diagnosing and grading AAFD and the reported correlations are comparable to those published earlier for the preoperative radiographic validation of this cohort.<sup>22,36,37,39</sup> The best correlated distance measures was the cuboid height ( $R^2 = 0.983$ ), followed by the 1<sup>st</sup> cuneiform height ( $R^2 = 0.587$ ) and navicular height ( $R^2 = 0.566$ ), though the cuboid height measure demonstrated significant negative fixed and proportional bias that caused the models to under predict that measure at higher observed patient magnitudes. Along with talo-1<sup>st</sup> metatarsal angle, 1<sup>st</sup> cuneiform height is an often utilized measure of medial column height in those with AAFD.<sup>38,133</sup>

Following surgical correction, average patient radiographic joint measures only changed modestly with the AP talonavicular coverage angle ( $-5.9^\circ$ ) and the AP talonavicular uncoverage distance ( $-3.0\text{mm}$ ) demonstrating the greatest changes. Decreases in these two measures, combined with smaller decreases noted for the AP talo-1<sup>st</sup> metatarsal ( $-1.6^\circ$ ) and AP talo-2<sup>nd</sup> metatarsal ( $-1.9^\circ$ ) angles indicate that across the patient cohort there was a modest improvement in the talonavicular deformity and forefoot abduction that are hallmarks of AAFD.<sup>70</sup> Changes in the ML x-ray view were slight with mixed results across the five angles and five distance measures. Calcaneal pitch changed by an average of  $-1.0^\circ$  in this cohort indicating a slight increase in deformity and ML talo-1<sup>st</sup> metatarsal angle and 1<sup>st</sup> cuneiform height measures improved by an average of  $1.6^\circ$  and  $0.5\text{mm}$ , respectively.

Improvements in both the FAOS and SF-36 questionnaires indicated that patient satisfaction with the surgery was generally high indicating both symptomatic and functional relief of flatfoot disability, in agreement with other investigators.<sup>79</sup> Specifically, the FAOS

scores improved postoperatively to an average of 360/500 ( $\pm 136$ ), up from a preoperative mean of 180/500 ( $\pm 78$ ). SF-36 scores also improved from a preoperative mean of 47/100 ( $\pm 18$ ) to a postoperative mean of 71/100 ( $\pm 19$ ).<sup>138</sup> Interestingly, despite clinical restoration of patient function as evidenced by pain-free single-leg heel raise and marked improvement in self-reported outcome questionnaires, there was not a statistically significant improvement in the most clinically utilized radiographic measures of AAJD, namely the AP talonavicular coverage angle, the AP talo-1st metatarsal angle, the ML talo-1st metatarsal angle, or the ML 1st cuneiform height.<sup>138</sup>

While the magnitude of correcting power contributed to MCO and FHL tendon transfer varies significantly among authors, most agree that the greatest corrections are observed in the standard AP view, with smaller changes in the ML x-ray measures.<sup>79,80,92,93,141–143</sup> In a group of 32 patients, Myerson and Corrigan noted some of the largest improvements in the literature for both ML and AP measures following MCO and tendon transfer. Specifically, these authors reported short term (mean=20 months) improvements in the AP talonavicular coverage angle (average =  $-21^\circ$ ), AP talo-1st metatarsal angle (average =  $-21^\circ$ ), ML talo-1st metatarsal angle (average =  $+12^\circ$ ), and ML 1st cuneiform height (average =  $+10\text{mm}$ ).<sup>143</sup> Guyton et al. observed more modest medium term improvement (mean=32 months) in the AP and ML radiographic measures for their cohort of 19 patients following correction by FDL transfer with MCO. They reported improvements in the AP talonavicular coverage angle (average =  $-11.8^\circ$ ), AP talo-1st metatarsal angle (average =  $-13.9^\circ$ ), AP talo-2nd metatarsal angle (average =  $-14.8^\circ$ ) and ML talo-1st metatarsal angle (average  $-7.7^\circ$ ).<sup>79</sup> In a similar study, Tellisi et al. also reported modest medium term improvements (mean=44.5 months) for their cohort of 29 patients under age 50 in

the AP talonavicular coverage angle (average =  $-12.5^{\circ}$ ), ML talo-1st metatarsal angle (average =  $-5.8^{\circ}$ ), and ML 1st cuneiform height (average =  $+5.9\text{mm}$ ).<sup>144</sup> By contrast, in their cohort of 17 patients, Sammarco and Hockenbury reported similar postoperative trends for their cohort of 19 patients following an FHL transfer with MCO but with much smaller magnitude improvements. Here, they noted small improvements in the ML plane with increases in the 1st cuneiform height (average =  $+0.4\text{mm}$ ) and talo-1st metatarsal angle (average =  $-3.2^{\circ}$ ), though neither measure was significantly different. Interestingly, they reported increases in the AP talonavicular angle (average =  $+6^{\circ}$ ) indicative of an increase in the forefoot abduction measure of deformity.<sup>80</sup>

The large range of radiographic improvements seen in the above four studies underscore that there is significant variability in the magnitude of surgical intervention, namely MCO size, and degree of radiographic change. However, there is not a clear indication that patients with a greater magnitude of radiographic correction have any additional improvement in functional outcomes, e.g. single leg heel raise, or in self-reported satisfaction with the surgery.

Furthermore, though all of the above authors noted that the transfers were tensioned and sutured in similar ways and all reported MCOs of 5-10mm in similar approaches, there are large differences in correction.<sup>79,80,143,144</sup> This incongruity suggests that these authors may be reporting the size of the MCO and degree of radiographic change based on somewhat ambiguous definitions of the angle and distance measures. Thus, while each of these studies follows patients with ostensibly the same surgical reconstruction, weak methodological definitions of intraoperative MCO magnitude and uncertain identification and measurement of the radiographs likely mean that across study comparisons are not possible. In further support of this assessment, all three studies report high patient-reported outcome scores based on the standardized and

validated AOFAS, FAOS, and SF-36 questionnaires though presumably the precise nature of the surgical correction was dissimilar across the three populations.<sup>79,80,143</sup> Thus the specific relationship between improvement in radiographic measures and perceived success of surgery remains ambiguous, and thus the ideal magnitude of MCO and tendon transfer tension remains to be discovered.

Within this cohort, the model angle and distance predictions echoed the changes in x-ray measures observed for the patients by predicting corrective changes in all x-ray measures. Further, the models correctly predicted the direction of x-ray measure change for all angles except talar declination which changed by just  $+0.4^{\circ}$  across the patient cohort and by  $-0.3^{\circ}$  across the model cohort. Though moderately well correlated, changes in the medial column height as measured by the ML x-ray distances were small and generally underestimated the patient x-ray changes.

For patient plantar loading, following surgical correction, average medial forefoot loading decreased concomitant with increases in average lateral forefoot loading. This trend was mirrored in the model cohort though the magnitude of change was somewhat smaller for the medial and lateral forefoot regions. This trend of medial offloading following MCO and tendon transfer supports the conclusions of previous modeling and in vitro works and is presumably the consequence of an increased inversion moment arm for the Achilles following MCO and at the navicular through the redirected FHL.<sup>5,17,48,50,145</sup>

One powerful advantage of computational modeling is that parameters such as ligament strain and joint contact force can be probed with relative ease as compared to in vitro testing or in vivo settings. For this model cohort, predictions of spring ligament function suggest that

following MCO and tendon transfer, there is an approximately 3% reduction in strain relative to the stress-free length for this tissue. This observation coupled with somewhat smaller reductions predicted for the deltoid ligament support the assertion that PTT insufficient feet have increased calcaneal inversion following MCO allowing for the sustentaculum tali to rotate inwardly toward the deltoid origins on the medial malleolus.<sup>142,146</sup> Indeed, Otis et al reported a 3% reduction in superomedial spring ligament strain following a 10mm MCO for their cohort of nine cadaveric lower extremities.<sup>142</sup> For the plantar fascia, the model cohort predicted small reductions in the strain of the medial bands in agreement with in vitro measurements reported by Horton et al.<sup>147</sup> However, predictions of central band plantar fascia strain increases were unexpected and suggest that the plantar fascia may experience varied changes in strain based on the tissue course through the arch. Finally, model predictions of shifting joint contact force from the medial column (talonavicular joint) to the lateral column (calcaneocuboid joint) of the foot mirror changes observed for plantar force measures in both the patient and model. Further, this shift may implicate increased calcaneocuboid joint contact force in the increased incidence of non-surgical site lateral column pain in patients with AAFD corrections and postulated from in vitro models.<sup>48,52,108,144</sup>

The most significant weakness of this study is the small sample size. This led to low statistical power and wide 95% confidence intervals for even well-correlated radiographic measures. This limitation is confounded by the relatively poor inter- and intraobserver correlations reported for some of the radiographic measures investigated.<sup>36</sup> Future studies may utilize more robust angular and distance measures by directly correlating the predicted 3-D motions of the model bones to patient biplane fluoroscopy or weight-bearing computed

tomography, though neither are routinely used clinically. Additionally, assumptions regarding the activation of the extrinsic muscles of the foot would likely affect the outputs predicted by the model. Specifically, while normal activation patterns have been investigated through electromyography and maximal isometric plantar flexion torque, less is known about the relative activation in patients with AAJD secondary to PTT insufficiency.<sup>84,148</sup> Houck et al demonstrated that posterior compartment activity, comprised of the FHL, FDL, and PTT, is diminished for AAJD sufferers resulting in inversion force deficits of 20-30% compared to their unaffected peers. Yet, there is no published literature regarding relative FHL and FDL loading following tendon transfer and MCO, though most authors assume some level of postoperative hypertrophy in the transferred tendon.<sup>148</sup> Consequently, it is likely that underrepresented FHL force contributes to the models' underestimation of ML radiographic improvements postoperatively as well as the negatively correlated proportional bias observed for the talar declination and cuboid height. Finally, we have chosen to validate model predictions using radiographic and plantar force behavior during stance only and while the parameters investigated are widely accepted and utilized in clinical practice, stance nonetheless represents just a portion of overall foot function. Future investigations could be undertaken to further validate these models under a variety of loading conditions representing more dynamic motions such as normal gait.

In conclusion, our model cohort demonstrated good agreement in the angles and distances relative to their patient-matched controls. As in our preoperative validation, these models showed very good predictive power for the talo-1st metatarsal angle and medial cuneiform height in the ML view, as well as the talonavicular coverage angle in the standard AP plane.<sup>22</sup> In addition, these models were able to predict the medial to lateral shift in plantar

forces observed in our patient group following MCO and FHL tendon transfer. Further, model predictions of decreased medial soft-tissue strains in the spring and deltoid ligaments, as well as the plantar fascia mirror those reported for cadaveric studies and provide insight into the mechanism of AAJD surgical correction. Finally, significant increases in lateral column joint contact force concomitant with MCO suggest future in vitro studies could investigate calcaneocuboid joint force as a cause for postoperative lateral foot pain. In conclusion, we believe rigid body modeling remains a powerful tool for predicting in vivo biomechanical foot function for patients with AAJD. Future increases in the number and refinement of these models will allow for continued investigation of relevant physiologic parameters that are difficult or impossible to measure non-invasively with the goal of better supporting the medical field in the treatment of foot pathologies.

## **9. PARAMETRIC ANALYSIS**

### **9.1 OVERVIEW**

As described in Chapters 7 and 8, we were able to validate the radiographic predictions of our model cohort against their patient-matched observations as well as characterize the nature of their error. Following this, we sought to exploit the unique characteristics of rigid-body modeling to predict ground reaction forces, bony contact forces, and ligament strains in the postoperative model states. Finally, we desired to parametrically evaluate the effects of variable magnitudes of the MCO procedure both in isolation and in combination with an FHL tendon transfer.

### **9.2 METHODS**

The five models, representing the five patients available for follow up, were again loaded in neutral plantar flexion against a rigid base as described previously. Postoperative bodyweight was applied vertically down through the tibia and vectors representing muscle tension scaled relative to BW were unchanged from previous postoperative simulations. Likewise, ligament definitions, including assumptions of in situ strain, stiffness, and orientation, were maintained from the pre- and postoperative simulations described previously.

In order to investigate the individual contributions of the MCO and tendon transfers, three additional hypothetical states were created for each of the five models. Thus, there were a total of four modeled states in this parametric investigation: one based on the observed patient-



specific state and three hypothetical states. Specifically, (1) the first was an intact state loaded with the patients' postoperative weight (Intact+PostOpBW). By using the postoperative BW, all subsequent surgical states could be compared to intact without the confounding influence of the patients' variable amount of weight gain observed prior to follow up. (2) The second scenario incorporated the FHL tendon transfer without any MCO and thus allowed for the investigation of the isolated effects of the transfer (PostOp-TTonly). (3) The third state represented an FHL tendon transfer with the radiographically verified patient-specific magnitude of MCO. This series of data points is repeated from Chapter 8 and included here to help demonstrate the relative contributions of each intervention (PostOp-TT+PatSpec MCO). (4) And finally, the fourth state was an FHL tendon transfer combined with an exaggerated MCO of 10mm (PostOp-TT+10mmMCO). This magnitude of medializing fragment movement was chosen as the upper limit of translation seen in the literature and was designed to elucidate any radiographic, soft-tissue, or contact loading trends that may be coupled to the size of the MCO. It is important to note that this larger MCO size was chosen as a hypothetical limit and may not have been viable in any patient's particular surgical case.

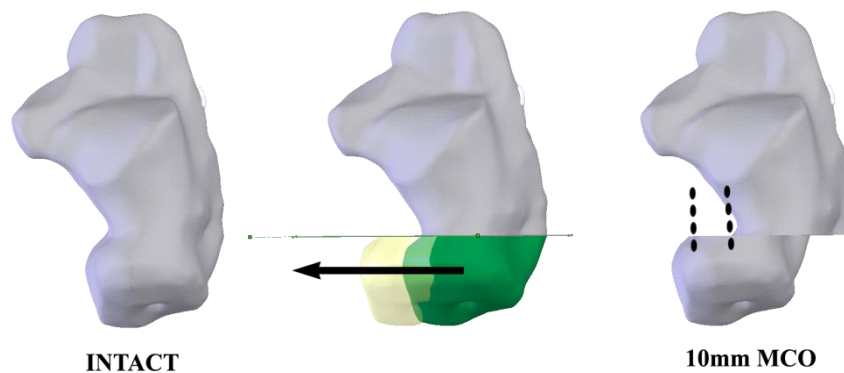


**Figure 9-1: Dorsoplantar view of example variable MCO creation workflow.**

Model fitness was measured using simulated radiographs in the ML and AP views as described in Chapters 7 and 8. The predicted changes in radiographic angles and distances were recorded for the three surgical states using the Intact+PostOpBW as the baseline state.

Additionally, plantar force distribution changes from Intact+PostOpBW were recorded for each of the three surgical states across three regions; medial forefoot, lateral forefoot, and hindfoot as described in Section 8.2.1. Articular contact force changes were recorded at the talonavicular, navicular-1st cuneiform, and calcaneocuboid joints and used as a measure of relative medial versus later column loading in the foot in each of the four states. Finally, spring ligament, deltoid ligament, and plantar fascia strain were investigated across the four states.

Differences in simulated radiographic measures, plantar loading, joint contact force, and ligament strain were analyzed using a mixed model one-way ANOVA, blocked on patient, accompanied by Tukey-Kramer post hoc analyses for those groups demonstrating significance. Models were analyzed using SAS (v9.3, Statistical Analysis System, SAS Institute, 2013); significance was defined as  $p < \alpha = 0.05$ .

## 9.3 RESULTS

### 9.3.1 Radiographic Predictions

The three hypothetical states and one patient-matched postoperative state modeled across the five returning patients required a total of 20 modeling simulations. However, one patient model (#5) was not able to be run in the tendon transfer only state. As a consequence, there were unequal treatment group sizes for the prescribed ANOVAs. Thus, while this patient's overall variance is reflected in the population means, post-hoc statistical analyses are only reflected for Patient #5 in relation to comparisons between the tendon transfer + patient-specific MCO and the tendon transfer + 10mm MCO groups.

Across the four treatments investigated, there were generally small individual and combined effects for the tendon transfer and MCO in the angle measures. Additionally, these changes were always in the direction of normal in surgical states that included an MCO (states 3,4). The largest angular improvements were noted in the standard AP view where the tendon transfer + 10mm MCO state was significantly lower than intact and the tendon transfer only states for all three angular measures ( $p<0.05$ ). [Figure 9-2] In contrast, the largest distance improvements were in the ML view, though only the 1st cuneiform to 5th metatarsal height was significantly increased over the intact + PostOp BW as well as the tendon transfer only states ( $p<0.05$ ). [Figure 9-3]

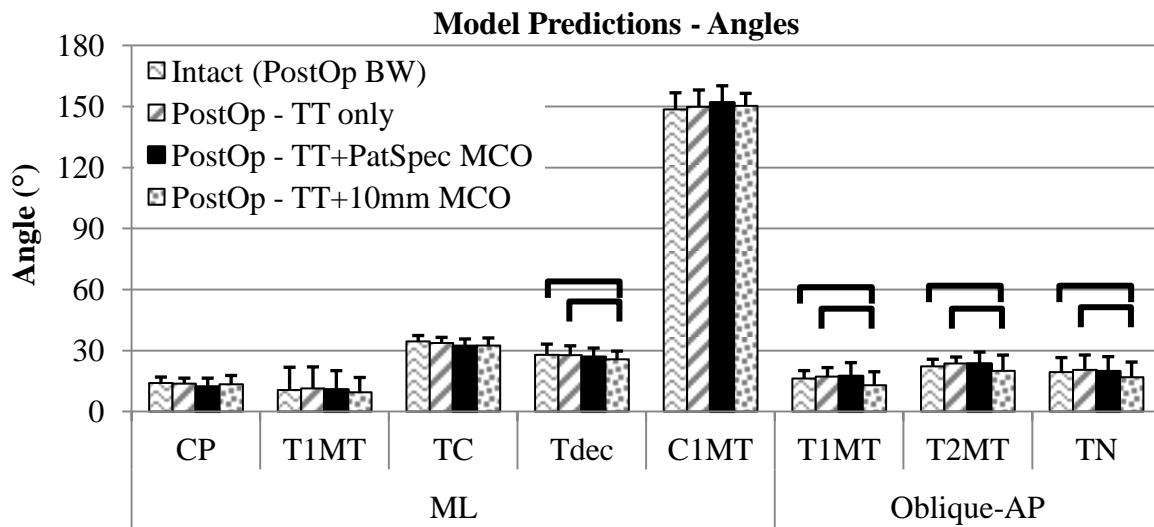


**Figure 9-2: Overview of treatment effect on simulated x-ray angle measures. Bracket bars indicate significant differences,  $p < 0.05$ .**

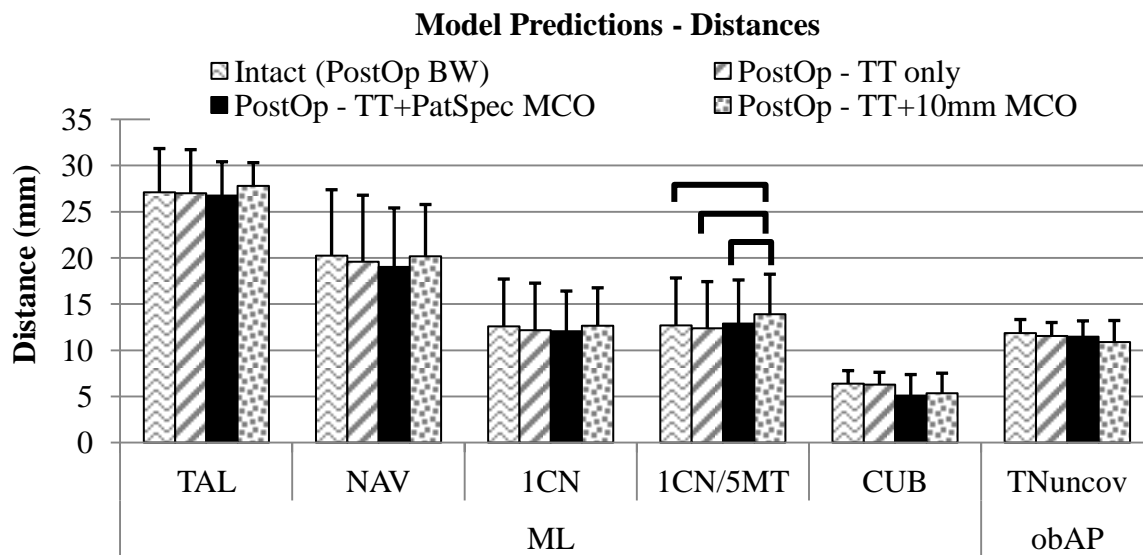


**Figure 9-3: Overview of treatment effect on simulated x-ray distance measures. Bracket bars indicate significant differences,  $p < 0.05$ .**

FHL tendon transfer alone, was predicted to have varied effects on the radiographic measures. In general these were characterized by minor decreases in ML angles and small but

consistent increases in AP angles. There were seemingly trivial changes in ML and AP distance measures as suggested by other investigators.<sup>92</sup> Specifically, the largest angular change in the ML view was observed for the calcaneo-1st metatarsal angle which increased in all models (ML-C1MT; mean =  $1.3^{\circ} \pm 0.5^{\circ}$ ). This was followed by an increase in ML talo-1st metatarsal angles (mean =  $0.8^{\circ} \pm 0.9^{\circ}$ ) and a decrease in ML talocalcaneal angles (ML-TC; mean =  $-0.8^{\circ} \pm 1.5^{\circ}$ ).

[Figure 9-4]

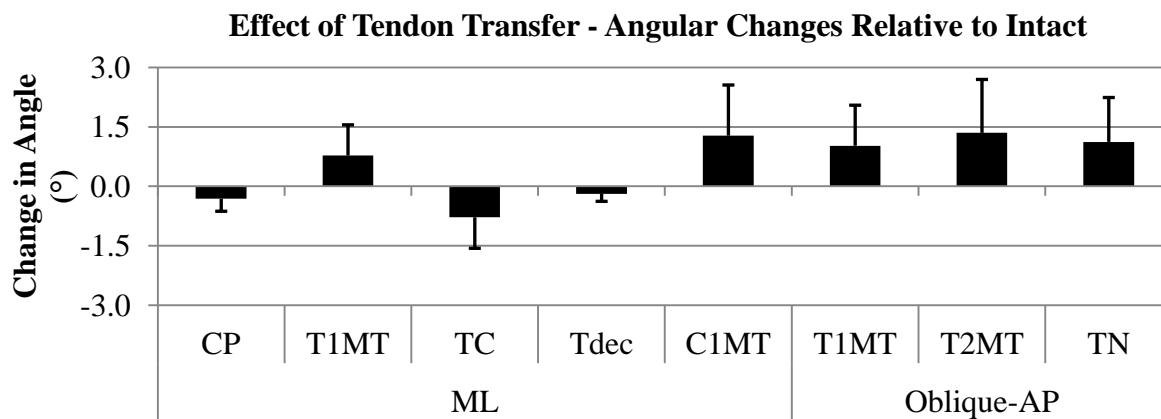


**Figure 9-4: Average angle changes from Intact (+PostOp BW) following isolated FHL tendon transfer.**

All radiographic distance measure averages decreased with isolated tendon transfer, indicating a very small decrease in medial column height. Of these decreases, navicular height demonstrated the largest drop (ML-NAV; mean =  $-0.7\text{mm} \pm 0.1\text{mm}$ ), followed by the 1st cuneiform height (ML-1CN; mean =  $-0.4\text{mm} \pm 0.2\text{mm}$ ). [Figure 9-5]

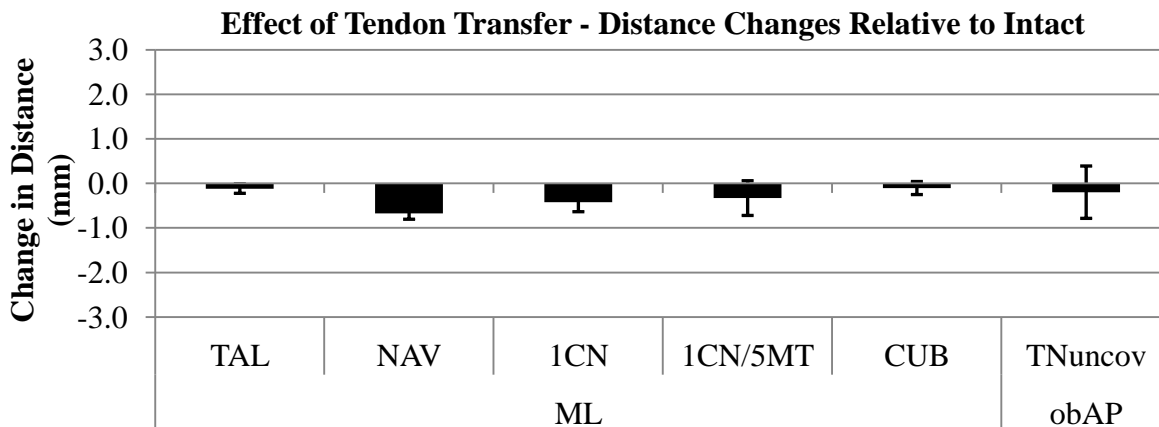


**Figure 9-5: Average distance changes from Intact (+PostOp BW) following isolated FHL tendon transfer.**

Following subsequent 10mm MCO, the radiographic angle and distance measures generally showed changes in the opposite, or offsetting, direction from those observed in the tendon transfer only state. For angles in the ML view, model predicted effects were modest with the talo-1st metatarsal angle demonstrated the largest average angle improvement (ML-T1MT; mean =  $-3.7^{\circ} \pm 4.4^{\circ}$ ). In the standard AP view, the addition of a 10mm MCO resulted in moderate to large improvements for all three angles measured. Specifically, the talo-1st metatarsal (AP-T1MT; mean =  $-6.6^{\circ} \pm 4.2^{\circ}$ ), talo-2nd metatarsal (AP-T2MT; mean =  $-6.2^{\circ} \pm 3.8^{\circ}$ ), and talonavicular coverage (AP-TN; mean =  $-5.4^{\circ} \pm 3.3^{\circ}$ ) angles all moved in the direction of normal. [Figure 9-6] All average distance measures increased with the addition of the 10mm MCO and were thus all in the direction of normal. As with the angular measures, these changes generally counteracted those induced for the tendon transfer only. The exceptions to this trend were the cuboid height (ML-CUB; mean =  $-0.2\text{mm} \pm 1.9\text{mm}$ ) and the talonavicular uncoverage distance (AP-TNuncov; mean =  $-0.9\text{mm} \pm 1.3$ ). For these two measures, the changes effected by the addition of a 10mm MCO were additive. [Figure 9-7]

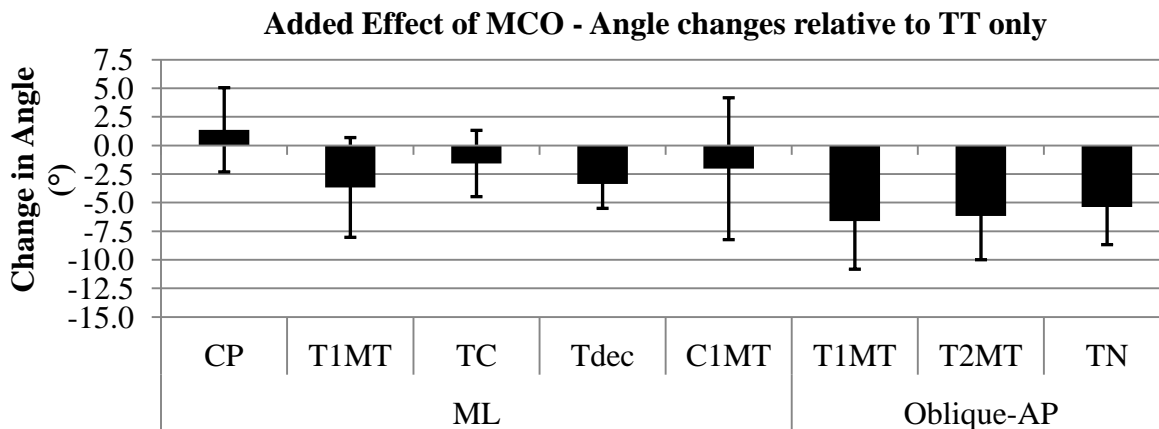


**Figure 9-6: Average angle changes from FHL Tendon Transfer only state following the addition of 10mm MCO.**

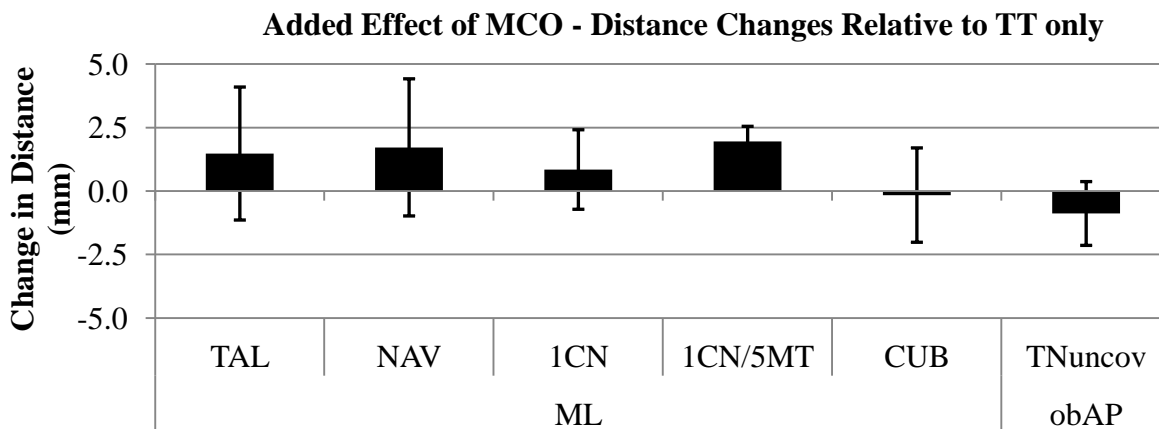


**Figure 9-7: Average distance changes from FHL Tendon Transfer only state following the addition of 10mm MCO.**

### 9.3.2 Plantar Force Predictions

Predictions of medial forefoot loading (Region 1; mean = 17.6% BW) were highest in the intact (+PostOp BW) state and decreased with all three subsequent surgical treatments to a minimum of 12.2% BW for the largest surgical reconstruction. The tendon transfer + patient-specific MCO ( $p < 0.05$ ) and tendon transfer + 10mm MCO ( $p < 0.001$ ) states were significantly

less than intact + PostOp BW; tendon transfer + 10mm MCO ( $p<0.01$ ) was also significantly diminished from the tendon transfer only state. The lateral forefoot demonstrated the opposite trend and rose from a minimum mean of 24.2% BW in the intact + PostOp BW state to a maximum average of 33.2% BW in the tendon transfer + 10mm MCO case. All of these changes were significantly different ( $p<0.01$ ) with the exception of the tendon transfer only state which was not significantly different from intact + PostOp BW. In addition, hindfoot loading was reduced a modest but statistically significant amount ( $p<0.01$ ) following each additional correction for all states except between the intact + PostOp BW and tendon transfer only states, as well as the tendon transfer + patient-specific MCO and tendon transfer + 10mm MCO states which were not different from one another. [Figure 9-8]



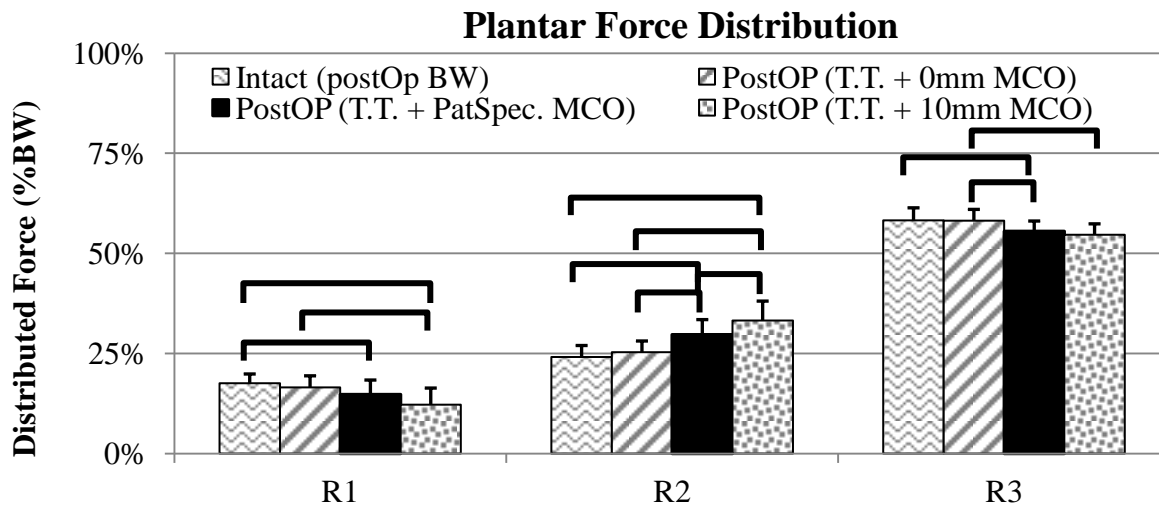


**Figure 9-8: Average plantar force distribution for across states. Bracket bars indicate significant differences,  $p<0.05$ .**

### 9.3.3 Soft-tissue Strains and Joint Contact Force Predictions

Average strain in the three soft-tissue structures investigated generally decreased with increasing surgical correction. The most pronounced reductions were in the three bands of the spring ligament where the inferomedial (IMCN), middle (MCN), and superomedial (SMCN) calcaneonavicular ligament strain reduced from baseline by 0.089, 0.054, and 0.051, respectively, for the tendon transfer + 10mm MCO state. These reductions were significantly different from intact for the two states with an MCO ( $p<0.05$ ). The plantar fascia demonstrated only minor changes in strain for the lateral four bands modeled, though the medial most band, Band 1, showed a consistent and statistically significant increase in strain following isolated tendon transfer ( $p<0.05$ ). This increase was completely abolished in the two states that also included an MCO, such that all four states were different from one another ( $p<0.05$ ). The tendon

transfer + 10mm MCO surgical state showed the largest reduction in strain of 0.015 over the intact + PostOp BW state. [Figure 9-9]

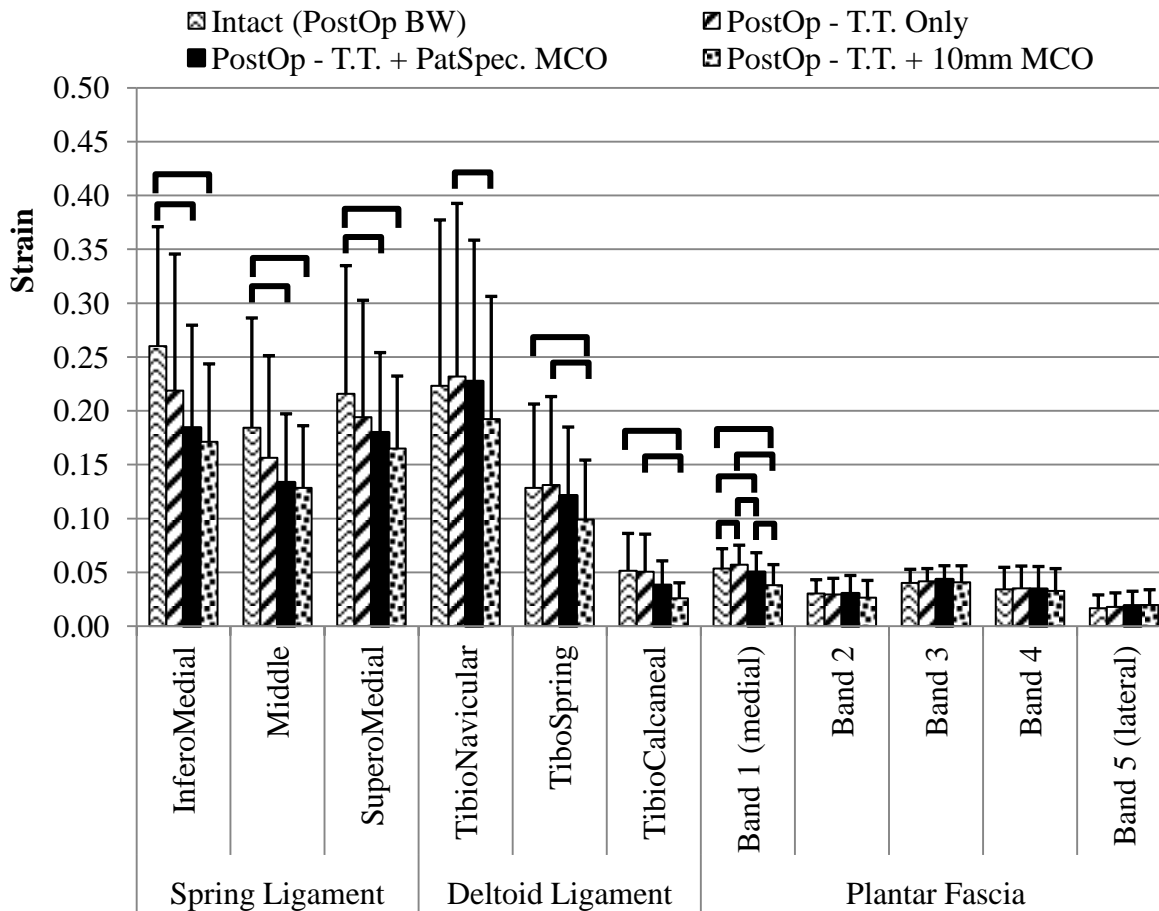


**Figure 9-9: Predicted soft-tissue strains across the models' four states. Bracket bars indicate significant differences,  $p < 0.05$ .**

Finally, mean articular contact force demonstrated marked increases at the calcaneocuboid joint of the lateral column for the two surgical states that included an MCO. While this mean value increased to more than 1.6x BW over the intact + PostOp BW state value of 1.0x BW, it approached but did not reach significance compared to the intact state ( $p=0.08$ ). These lateral column increases were accompanied by significant decreases in navicular-1st

cuneiform loading with additional surgical correction such that all states were significantly different from one another ( $p < 0.05$ ) except for the tendon transfer only and tendon transfer + patient-specific MCO states. [Figure 9-10]

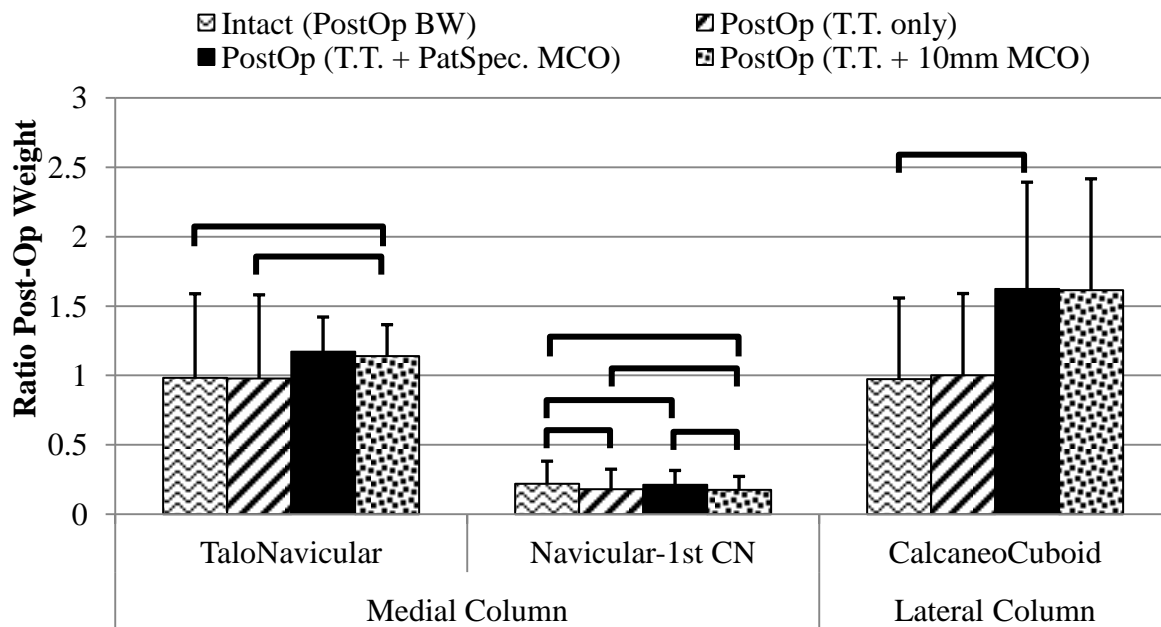


**Figure 9-10: Predicted changes in medial and lateral column joint contact force, normalized to postoperative body weight across the models' four states. Bracket bars indicate significant differences,  $p < 0.05$ .**

#### 9.4 DISCUSSION

This parametric study investigated the effects of three additional hypothetical surgical states in our patient population: (1) an intact state loaded with the BW observed at the postoperative follow up, (2) an FHL tendon transfer only state, and (3) an FHL tendon transfer with an exaggerated 10mm MCO. These three states were then compared to the actual surgical correction which incorporated the patient-specific amount of MCO. Following tendon transfer

only, the radiographic angular and distance changes suggested a slight degradation in most of the indicative measures of AAJD.<sup>36,37</sup> Specifically, there was an average decrease in calcaneal pitch angle and all medial column distance measures. This was coupled to modest increases in the talo-1st metatarsal, talar declination, and calcaneo-1st metatarsal angles in the ML view and minor increases to the talo-1st metatarsal, talo-2nd metatarsal, and talonavicular coverage angles in the standard AP view. While seemingly surprising given the purported effect of PTT augmentation through tendon transfer, these observations support the findings of Mann and Thompson, Funk et al., Trnka et al. and others who have critiqued that soft-tissue reconstructions provide only minor correction of medial column collapse and likely would not maintain those alignment corrections in the absence of other bony procedures.<sup>69,92,149</sup> Indeed, numerous investigations, including ones from this laboratory, have suggested that the effect of the tendon transfer is not to restore the medial column height of the foot, but instead to bolster the subtalar inversion force potential through imitated PTT function.<sup>50,92</sup>

The subsequent inclusion of a 10mm MCO had a larger effect on joint angles and distances than did the tendon transfer alone, though the overall correction remained less than what has been reported in other clinical studies.<sup>93,143</sup> None of the models predicted radiographic improvement at the upper end of those reported in the literature. Specifically, while Myerson and Corrigan reported average improvements of  $-21^{\circ}$ ,  $-21^{\circ}$ ,  $+12^{\circ}$  for the AP talonavicular coverage angle, AP talo-1st metatarsal angle, and ML talo-1st metatarsal angle, respectively, the single largest change for a model with an FHL transfer + 10mm MCO in our cohort was just  $-11.9^{\circ}$  for one AP talo-1st metatarsal angle measurement; average improvements were lower still.<sup>78</sup> This level of disagreement is likely further evidence that more robust and repeatable measures

of intraoperative correction and radiographic changes are critical if the disparate correction values in the literature are to be reconciled.

One of the primary strengths of computational modeling is the ability to probe multiple aspects of the system's behavior without confounding other observations. To this end, both articular contact force in the talonavicular, navicular-1st cuneiform, and calcaneocuboid joints were able to be investigated simultaneously with changing soft-tissue strains in the spring ligament, deltoid ligament, and plantar fascia. For the tissue strains, marked decreases in all three bands of the spring ligament mimic those trends observed in the postoperative state discussed in Section 8.3.2, but with greater magnitudes. Thus, these observations support the findings of Otis et al. that MCO causes a decrease in spring ligament strain.<sup>142</sup> Further, they lend additional support to the notion that increased surgical intervention, especially increased MCO size, diminishes the valgus and plantar tilt of the calcaneus, thereby allowing the talar head to move superiorly and become more covered by the navicular. Radiographically, this is evident in the decreases in AP angles following repair. The underlying mechanism causing this shift may be that the line of action of the Achilles becomes increasingly inverting with increasing MCO size, and so therefore becomes an agonist to the transferred FHL and the deficient PTT.<sup>48</sup> While not proven in this study, this hypothesized mechanism is supported by the concomitant shift in plantar load from the medial forefoot to the lateral forefoot which was most marked when an MCO correction was incorporated.

The relatively modest changes in plantar fascia strain across the four states investigated conflicts with the now disfavored notion that the plantar fascia is pulled taut with increasing MCO, thereby mediating correction through an amplified windlass mechanism.<sup>150</sup> To the

contrary, the constancy of the lateral four bands and *decreases* in strain in the medial most band suggest the opposite mechanism to be driving function. As such, these findings support those of Horton et al. in describing the effect of MCO on the plantar fascia as one that *releases* tension.<sup>147</sup>

Finally, the two surgical states that incorporated an MCO caused a marked increase of more than 60% in calcaneocuboid articular contact force over the intact state. Surprisingly, this increase was not significantly different. This result is at least partly the result of having an incomplete parametric study, as the Patient #5 variance adds to the mean uncertainty, but because it lacks the tendon transfer only state, cannot be accurately assessed using post-hoc tests. This suspicion is bolstered by the fact that the changes are noted to be statistically significant when only complete data sets are analyzed. There was no significant difference between the load predicted for the patient-matched MCO value and the 10mm MCO, so it is not clear at what level of MCO this force begins to climb so steeply. Future simulations focused on covering the entire range of possible MCOs, not just those used clinically, may elucidate this important inflection point. The combined observations of increased lateral column joint load and increased lateral forefoot plantar load seem to support the theory that MCO is a contributor to idiopathic lateral foot pain following medial column correction. While this specific question has not been addressed in vitro, likely due to the technical challenges tracking changes in two variables so confounded by one another, Ellis et al. has posited that large magnitude MCO and lateral column lengthening procedures are indeed responsible for pain in those patients with high lateral forefoot loading postoperatively.<sup>52</sup>

Taken together, the data presented in this parametric study suggest that an MCO is crucial to achieving substantial radiographic improvements in the medial column of the foot, and that

increased MCO size is correlated with increased correction. Further, they demonstrate that increased MCO size leads to increased lateral plantar force transfer and diminished spring ligament strain, all of which are the purported aims of AAFD surgical correction. However, these predictions also underscore the notion that increased MCO may cause a marked increase in lateral column articular contact force. Thus, it appears that while current clinical diagnostics (x-ray) would likely support the use of as large an MCO as is surgically feasible, clinicians should be aware of the altered biomechanics that may lead to unforeseen pain and dysfunction in the future.

## **10. FUTURE DIRECTIONS AND CONCLUSIONS**

The modeling methodology put forth here has proved to be a reasonable predictor of foot and ankle kinematics as validated through clinically utilized radiographic angle and distance measures both pre- and postoperatively. Specifically, these models were able to match the observed trends and often the magnitudes of their respective patient x-ray observations, while demonstrating limited fixed and proportional bias. Further, it has been demonstrated that the rigid-body modeling technique allows for the investigation of additional parameters of clinical interest including changes in soft-tissue strain, articular contact force, and plantar force distribution. However, given the robust and infinitely repeatable nature of computer simulation, there remain tremendous, unexplored avenues of investigation using these models.

The most natural progression of this work is to continue to probe the isolated and combined effects of tendon transfer with a variable MCO. This may ultimately help to identify the optimal level of MCO for a given patient and potentially inform clinical understanding of how best to implement this correction. Following this, the modeled states may be expanded to include surgical states not implemented at all in these patients. Here, the most likely candidate surgeries would be some sort of lateral column lengthening procedure, such as the Evan's opening wedge calcaneal osteotomy, the calcaneal cuboid distraction arthrodesis, or perhaps the newer Z-cut osteotomy, which combines a lateral column and MCO procedure in a single osteotomy. Inclusion of these surgeries would allow for the investigation of isolated and combined effects across all of the major contemporary surgical techniques used to address AAFD.<sup>77</sup>



Beyond these immediate clinical questions, there are a number of areas where the modeling methodology itself can be improved. Perhaps the most expansive addition would be to divide the articular surfaces of bones into fine arrays of individual bodies. Though, still a rigid-body simulation, these equally spaced sub-bodies would allow for better localizations of contact force and approximations of contact area as has been done with discrete element techniques.<sup>151</sup> With regard to ligament definitions, there are also potential avenues of improvement. Specifically, the tissue stiffnesses may be more accurately modeled using nonlinear length-tension relationships for those ligaments where the published data is available. While likely not a revolutionary step, such iterative improvements would allow the models to better predict soft-tissue force at positions of early and late strain.

Finally, while the ability to model numerous parametrically adjusted surgical states across a cohort of models offers exciting opportunities for biomechanical investigations, these parallel modeling tracts also require exponentially more time to analyze and process. Therefore, now that the general methodology has been validated, future studies would benefit greatly from automating the assignment of initial loading conditions and tabulating of the modeling results. Specifically, it would be extremely beneficial to substitute the use of simulated 2-D radiographic views for the real-time analysis of the 3-D angular measures inherent to the modeled bones themselves. While, it would be necessary to correlate these new measures to ones used clinically, the negatives associated with working with new and unfamiliar measures would be wholly offset by the increased pace and number of additional modeling states that could be investigated.

Thus, whether the current patient-specific rigid-body computational models are expanded and refined in their function or simply widened in their application, the methodology described here offers a novel and robust tool to investigate foot and ankle function in patients with Adult Acquired Flatfoot Deformity. Furthermore, given that the models have been created with the use of commercially available software packages and are well validated within the outlined scope of this work, their predictive power strengthened over other rigid-body models currently available. Therefore, with further refinement, models such as these will continue to move forward in their predictive capabilities and clinical application with the ultimate goal of creating a clinical viable patient-specific planning tool to understand and predict postoperative function before surgery.

## **LITERATURE CITED**

1. Cheng H-YK, Lin C-L, Chou S-W, Wang H-W. Nonlinear finite element analysis of the plantar fascia due to the windlass mechanism. *Foot Ankle Int.* 2008;29(8):845–851. doi:10.3113/FAI.2008.0845.
2. Cheung JT-M, Zhang M, An K-N. Effects of plantar fascia stiffness on the biomechanical responses of the ankle-foot complex. *Clin Biomech.* 2004;19(8):839–846. doi:10.1016/j.clinbiomech.2004.06.002.
3. Cheung JT-M, An K-N, Zhang M. Consequences of partial and total plantar fascia release: a finite element study. *Foot Ankle Int.* 2006;27(2):125–132.
4. Iaquinto JM, Wayne JS. Computational model of the lower leg and foot/ankle complex: application to arch stability. *J Biomech Eng.* 2010;132:021009.
5. Iaquinto JM, Wayne JS. Effects of surgical correction for the treatment of adult acquired flatfoot deformity: A computational investigation. *J Orthop Res.* 2011;29(7):1047–1054. doi:10.1002/jor.21379.
6. Isvilanonda V, Dengler E, Iaquinto JM, Sangeorzan BJ, Ledoux WR. Finite element analysis of the foot: Model validation and comparison between two common treatments of the clawed hallux deformity. *Clin Biomech.* 2012;27(8):837–844. doi:10.1016/j.clinbiomech.2012.05.005.
7. Liacouras PC, Wayne JS. Computational modeling to predict mechanical function of joints: application to the lower leg with simulation of two cadaver studies. *J Biomech Eng.* 2007;129:811.
8. Salathe EP, Arangio GA. A biomechanical model of the foot: the role of muscles, tendons, and ligaments. *J Biomech Eng.* 2002;124(3):281–287.
9. Wei F, Hunley SC, Powell JW, Haut RC. Development and Validation of a Computational Model to Study the Effect of Foot Constraint on Ankle Injury due to External Rotation. *Ann Biomed Eng.* 2010;39(2):756–765. doi:10.1007/s10439-010-0234-9.
10. Wei F, Braman JE, Weaver BT, Haut RC. Determination of dynamic ankle ligament strains from a computational model driven by motion analysis based kinematic data. *J Biomech.* 2011;44(15):2636–2641. doi:10.1016/j.jbiomech.2011.08.010.
11. Yu J, Cheung JT-M, Fan Y, Zhang Y, Leung AK-L, Zhang M. Development of a finite element model of female foot for high-heeled shoe design. *Clin Biomech.* 2008;23:S31–S38. doi:10.1016/j.clinbiomech.2007.09.005.

12. Starly B, Fang Z, Sun W, Shokoufandeh A, Regli W. Three-dimensional reconstruction for medical-CAD modeling. *Comput-Aided Des Appl*. 2005;2(1-4):431–438.
13. Delp SL, Loan JP, Hoy MG, Zajac FE, Topp EL, Rosen JM. An interactive graphics-based model of the lower extremity to study orthopaedic surgical procedures. *Biomed Eng IEEE Trans*. 1990;37(8):757–767.
14. Piazza SJ, Delp SL. Three-Dimensional Dynamic Simulation of Total Knee Replacement Motion During a Step-Up Task. *J Biomech Eng*. 2001;123(6):599. doi:10.1115/1.1406950.
15. Davoodi R, Brown IE, Lan N, Mileusnic M, Loeb GE. An integrated package of neuromusculoskeletal modeling tools in Simulink<sup>TM</sup>. In: *Engineering in Medicine and Biology Society, 2001. Proceedings of the 23rd Annual International Conference of the IEEE*. Vol 2.; 2001:1205–1208.
16. Arangio GA, Chen C, Salathé EP. Effect of varying arch height with and without the plantar fascia on the mechanical properties of the foot. *Foot Ankle Int*. 1998;19(10):705–709.
17. Arangio GA, Salathé EP. Medial displacement calcaneal osteotomy reduces the excess forces in the medial longitudinal arch of the flat foot. *Clin Biomech*. 2001;16(6):535–539. doi:10.1016/S0268-0033(01)00011-0.
18. Caravaggi P, Pataky T, Goulermas JY, Savage R, Crompton R. A dynamic model of the windlass mechanism of the foot: evidence for early stance phase preloading of the plantar aponeurosis. *J Exp Biol*. 2009;212(Pt 15):2491–2499. doi:10.1242/jeb.025767.
19. Pandy MG, Zajac FE, Sim E, Levine WS. An optimal control model for maximum-height human jumping. *J Biomech*. 1990;23(12):1185–1198.
20. Pandy MG. Computer modeling and simulation of human movement. *Annu Rev Biomed Eng*. 2001;3(1):245–273.
21. Kwak SD, Blankevoort L, Ateshian GA. A Mathematical Formulation for 3D Quasi-Static Multibody Models of Diarthrodial Joints. *Comput Methods Biomech Biomed Engin*. 2000;3(1):41. doi:10.1080/10255840008915253.
22. Spratley EM, Matheis EA, Hayes CW, Adelaar RS, Wayne JS. Validation Of A Population Of Patient-Specific Adult Acquired Flatfoot Deformity Models. *J Orthop Res*. 2013. doi:DOI 10.1002/jor.22471.

23. Gray H. *Anatomy of the human body*. 20th edition. Philadelphia, PA: Bartleby.com, Inc.; 1918.
24. Agur AMR, Dalley AF. *Grant's atlas of anatomy*. Lippincott Williams & Wilkins; 2009.
25. Sarrafian SK. *Anatomy of the foot and ankle: descriptive, topographic, functional*. 2nd ed. Philadelphia, PA: Lippincott; 1993.
26. Milner CE, Soames RW. Anatomy of the collateral ligaments of the human ankle joint. *Foot Ankle Int*. 1998;19(11):757–760.
27. Schneck CD, Mesgarzadeh M, Bonakdarpour A, Ross GJ. MR imaging of the most commonly injured ankle ligaments. Part I. Normal anatomy. *Radiology*. 1992;184(2):499–506.
28. Milner CE, Soames RW. The medial collateral ligaments of the human ankle joint: anatomical variations. *Foot Ankle Int*. 1998;19(5):289–292.
29. Rule J, Yao L, Seeger L. Spring ligament of the ankle: normal MR anatomy. *Am J Roentgenol*. 1993;161(6):1241–1244.
30. Davis WH, Sobel M, DiCarlo EF, et al. Gross, histological, and microvascular anatomy and biomechanical testing of the spring ligament complex. *Foot Ankle Int*. 1996;17(2):95–102.
31. Taniguchi A, Tanaka Y, Takakura Y, Kadono K, Maeda M, Yamamoto H. Anatomy of the spring ligament. *J Bone Joint Surg Am*. 2003;85-A(11):2174–2178.
32. Gould N, Schneider W, Ashikaga T. Epidemiological Survey of Foot Problems in the Continental United States: 1978–1979\*. *Foot Ankle Int*. 1980;1(1):8–10. doi:10.1177/107110078000100104.
33. Lee MS, Vanore JV, Thomas JL, et al. Diagnosis and treatment of adult flatfoot. *J Foot Ankle Surg*. 2005;44(2):78–113. doi:53/j.jfas.2004.12.001.
34. Deland JT. Adult-acquired Flatfoot Deformity. *J Am Acad Orthop Surg*. 2008;16(7):399–406.
35. Schon LC, Weinfeld SB, Horton GA, Resch S. Radiographic and clinical classification of acquired midtarsus deformities. *Foot Ankle Int*. 1998;19(6):394–404.
36. Younger AS, Sawatzky B, Dryden P. Radiographic assessment of adult flatfoot. *Foot Ankle Int*. 2005;26(10):820–825.

37. Coughlin MJ, Kaz A. Correlation of Harris mats, physical exam, pictures, and radiographic measurements in adult flatfoot deformity. *Foot Ankle Int.* 2009;30(7):604–612. doi:10.3113/FAI.2009.0604.
38. Arangio GA, Wasser T, Rogman A. Radiographic comparison of standing medial cuneiform arch height in adults with and without acquired flatfoot deformity. *Foot Ankle Int.* 2006;27(8):636–638.
39. Ellis SJ, Yu JC, Williams BR, Lee C, Chiu Y, Deland JT. New radiographic parameters assessing forefoot abduction in the adult acquired flatfoot deformity. *Foot Ankle Int.* 2009;30(12):1168.
40. Thomas J, Kunkel M, Lopez R, Sparks D. Radiographic Values of the Adult Foot in a Standardized Population. *J Foot Ankle Surg.* 2006;45:3–12. doi:10.1053/j.jfas.2005.10.014.
41. Bruyn JM, Cerniglia MW, Chaney DM. Combination of Evans calcaneal osteotomy and STA-Peg arthroreisis for correction of the severe pes valgo planus deformity. *J Foot Ankle Surg.* 1999;38(5):339–346. doi:10.1016/S1067-2516(99)80005-2.
42. Murley GS, Menz HB, Landorf KB. A protocol for classifying normal- and flat-arched foot posture for research studies using clinical and radiographic measurements. *J Foot Ankle Res.* 2009;2:22. doi:10.1186/1757-1146-2-22.
43. Krans A van der, Louwerens JWK, Anderson P. Adult acquired flexible flatfoot, treated by calcaneo-cuboid distraction arthrodesis, posterior tibial tendon augmentation, and percutaneous Achilles tendon lengthening: A prospective outcome study of 20 patients. *Acta Orthop.* 2006;77(1):156–163. doi:10.1080/17453670610045858.
44. Saltzman CL, Nawoczenski DA, Talbot KD. Measurement of the medial longitudinal arch. *Arch Phys Med Rehabil.* 1995;76(1):45–49. doi:10.1016/S0003-9993(95)80041-7.
45. Cavanagh PR, Rodgers MM. The arch index: A useful measure from footprints. *J Biomech.* 1987;20(5):547–551. doi:10.1016/0021-9290(87)90255-7.
46. Morag E, Cavanagh PR. Structural and functional predictors of regional peak pressures under the foot during walking. *J Biomech.* 1999;32(4):359–370. doi:10.1016/S0021-9290(98)00188-2.
47. Ledoux WR, Hillstrom HJ. The distributed plantar vertical force of neutrally aligned and pes planus feet. *Gait Posture.* 2002;15(1):1–9.

48. Hadfield MH, Snyder JW, Liacouras PC, Owen JR, Wayne JS, Adelaar RS. Effects of medializing calcaneal osteotomy on Achilles tendon lengthening and plantar foot pressures. *Foot Ankle Int.* 2003;24(7):523–529.
49. Hadfield M, Snyder J, Liacouras P, Owen J, Wayne J, Adelaar R. The effects of a medializing calcaneal osteotomy with and without superior translation on Achilles tendon elongation and plantar foot pressures. *Foot Ankle Int.* 2005;26(5):365–370.
50. Spratley EM, Arnold JM, Owen JR, Glezos CD, Adelaar RS, Wayne JS. Plantar Forces in Flexor Hallucis Longus Versus Flexor Digitorum Longus Transfer in Adult Acquired Flatfoot Deformity. *Foot Ankle Int.* 2013. doi:10.1177/1071100713487724.
51. Oh I, Imhauser C, Choi D, Williams B, Ellis S, Deland J. Sensitivity of Plantar Pressure and Talonavicular Alignment to Lateral Column Lengthening in Flatfoot Reconstruction. *J Bone Jt Surg.* 2013;95(12):1094–1100. doi:10.2106/JBJS.K.01032.
52. Ellis SJ, Yu JC, Johnson AH, Elliott A, O'Malley M, Deland J. Plantar Pressures in Patients with and without Lateral Foot Pain After Lateral Column Lengthening. *J Bone Jt Surg Am.* 2010;92(1):81–91. doi:10.2106/JBJS.H.01057.
53. Schuh R, Gruber F, Wanivenhaus A, Hartig N, Windhager R, Trnka H-J. Flexor digitorum longus transfer and medial displacement calcaneal osteotomy for the treatment of stage II posterior tibial tendon dysfunction: kinematic and functional results of fifty one feet. *Int Orthop.* 2013:1–6. doi:10.1007/s00264-013-2071-6.
54. Goldner JL, Keats PK, Bassett FH 3rd, Clippinger FW. Progressive talipes equinovagum due to trauma or degeneration of the posterior tibial tendon and medial plantar ligaments. *Orthop Clin North Am.* 1974;5(1):39–51.
55. Deland JT. The adult acquired flatfoot and spring ligament complex: Pathology and implications for treatment. *Foot Ankle Clin North Am.* 2001;6(1):129–135. doi:10.1016/S1083-7515(03)00086-X.
56. Deland JT, de Asla RJ, Sung I-H, Ernberg LA, Potter HG. Posterior tibial tendon insufficiency: which ligaments are involved? *Foot Ankle Int.* 2005;26(6):427–435.
57. Williams G, Widnall J, Evans P, Platt S. MRI features most often associated with surgically proven tears of the spring ligament complex. *Skeletal Radiol.* 2013;42(7):969–973. doi:10.1007/s00256-013-1618-3.



58. Mizel MS, Temple HT, Scranton PE Jr, et al. Role of the peroneal tendons in the production of the deformed foot with posterior tibial tendon deficiency. *Foot Ankle Int.* 1999;20(5):285–289.
59. Lim PS, Schweitzer ME, Deely DM, et al. Posterior tibial tendon dysfunction: secondary MR signs. *Foot Ankle Int.* 1997;18(10):658–663.
60. Schweitzer ME, Karasick D. MR imaging of disorders of the posterior tibialis tendon. *Am J Roentgenol.* 2000;175(3):627–635.
61. Neville C, Flemister AS, Houck JR. Deep Posterior Compartment Strength and Foot Kinematics in Subjects With Stage II Posterior Tibial Tendon Dysfunction. *Foot Ankle Int.* 2010;31(4):320–328. doi:10.3113/FAI.2010.0320.
62. Keenan MA, Peabody TD, Gronley JK, Perry J. Valgus deformities of the feet and characteristics of gait in patients who have rheumatoid arthritis. *J Bone Joint Surg Am.* 1991;73(2):237–247.
63. Ringleb SI, Kavros SJ, Kotajarvi BR, Hansen DK, Kitaoka HB, Kaufman KR. Changes in gait associated with acute stage II posterior tibial tendon dysfunction. *Gait Posture.* 2007;25(4):555–564.
64. Semple R, Murley GS, Woodburn J, Turner DE. Tibialis posterior in health and disease: a review of structure and function with specific reference to electromyographic studies. *J Foot Ankle Res.* 2009;2(1):24. doi:10.1186/1757-1146-2-24.
65. Hicks JH. The mechanics of the foot: II. The plantar aponeurosis and the arch. *J Anat.* 1954;88(Pt 1):25.
66. Rush SM, Christensen JC, Johnson CH. Biomechanics of the first ray. Part II: Metatarsus primus varus as a cause of hypermobility. A three-dimensional kinematic analysis in a cadaver model. *J Foot Ankle Surg.* 2000;39(2):68–77. doi:10.1016/S1067-2516(00)80030-7.
67. Jack EA. Naviculo-cuneiform fusion in the treatment of flat foot. *J Bone Joint Surg Br.* 1953;35-B(1):75–82.
68. Mann RA. Acquired flatfoot in adults. *Clin Orthop.* 1983;(181):46–51.
69. Mann RA, Thompson FM. Rupture of the posterior tibial tendon causing flat foot. Surgical treatment. *J Bone Jt Surg Am.* 1985;67(4):556–561.

70. Johnson KA, Strom DE. Tibialis posterior tendon dysfunction. *Clin Orthop*. 1989;(239):196–206.
71. Myerson MS. Instructional Course Lectures, The American Academy of Orthopaedic Surgeons-Adult Acquired Flatfoot Deformity. Treatment of Dysfunction of the Posterior Tibial Tendon. *J Bone Jt Surg*. 1996;78(5):780–792.
72. Parsons S, Naim S, Richards PJ, McBride D. Correction and Prevention of Deformity in Type II Tibialis Posterior Dysfunction. *Clin Orthop*. 2010;468(4):1025–1032. doi:10.1007/s11999-009-1122-1.
73. Vulcano E, Deland JT, Ellis SJ. Approach and treatment of the adult acquired flatfoot deformity. *Curr Rev Musculoskelet Med*. 2013;1–10. doi:10.1007/s12178-013-9173-z.
74. Ogston A. On Flat-Foot, And Its Cure By Operation. *The Lancet*. 1884;123(3152):152–155. doi:10.1016/S0140-6736(02)12753-X.
75. Whitman R. Observations on forty-five cases of flat-foot with particular reference to etiology and treatment. *Boston Med Surg J*. 1888;118(25):616–620.
76. Sangeorzan BJ, Smith D, Veith R, Hansen ST Jr. Triple arthrodesis using internal fixation in treatment of adult foot disorders. *Clin Orthop*. 1993;(294):299–307.
77. Hiller L, Pinney SJ. Surgical treatment of acquired flatfoot deformity: what is the state of practice among academic foot and ankle surgeons in 2002? *Foot Ankle Int*. 2003;24(9):701–705.
78. Myerson MS, Corrigan J. Treatment of posterior tibial tendon dysfunction with flexor digitorum longus tendon transfer and calcaneal osteotomy. *Orthopedics*. 1996;19(5):383–388.
79. Guyton GP, Jeng C, Krieger LE, Mann RA. Flexor digitorum longus transfer and medial displacement calcaneal osteotomy for posterior tibial tendon dysfunction: a middle-term clinical follow-up. *Foot Ankle Int*. 2001;22(8):627–632.
80. Sammarco GJ, Hockenbury RT. Treatment of stage II posterior tibial tendon dysfunction with flexor hallucis longus transfer and medial displacement calcaneal osteotomy. *Foot Ankle Int*. 2001;22(4):305–312.
81. Sutherland D H. An Electromyographic Study of the Plantar Flexors of the Ankle in Normal Walking on the Level. *J Bone Jt Surg*. 1966;48(1):66–71.

82. Pichler W, Tesch NP, Grechenig W, Tanzer K, Grasslobler M. Anatomical variations of the flexor hallucis longus muscle and the consequences for tendon transfer. A cadaver study. *Surg Radiol Anat SRA*. 2005;27(3):227–231. doi:10.1007/s00276-005-0314-y.
83. LaRue BG, Anctil EP. Distal anatomical relationship of the flexor hallucis longus and flexor digitorum longus tendons. *Foot Ankle Int*. 2006;27(7):528–532.
84. Murray MP, Guten GN, Baldwin JM, Gardner GM. A comparison of plantar flexion torque with and without the triceps surae. *Acta Orthop Scand*. 1976;47(1):122–124.
85. Ferris L, Sharkey NA, Smith TS, Matthews DK. Influence of extrinsic plantar flexors on forefoot loading during heel rise. *Foot Ankle Int*. 1995;16(8):464–473.
86. Hahn F, Maiwald C, Horstmann T, Vienne P. Changes in plantar pressure distribution after Achilles tendon augmentation with flexor hallucis longus transfer. *Clin Biomech*. 2008;23(1):109–116. doi:10.1016/j.clinbiomech.2007.08.015.
87. Richardson DR, Willers J, Cohen BE, Davis WH, Jones CP, Anderson RB. Evaluation of the hallux morbidity of single-incision flexor hallucis longus tendon transfer. *Foot Ankle Int*. 2009;30(7):627–630. doi:10.3113/FAI.2009.0627.
88. Coughlin MJ, Mann RA. *Surgery of the foot and ankle*. 7th ed. St. Louis, MO: Mosby; 1999.
89. Mulier T, Rummens E, Dereymaeker G. Risk of neurovascular injuries in flexor hallucis longus tendon transfers: an anatomic cadaver study. *Foot Ankle Int*. 2007;28(8):910–915. doi:10.3113/FAI.2007.0910.
90. O’Sullivan E, Carare-Nnadi R, Greenslade J, Bowyer G. Clinical significance of variations in the interconnections between flexor digitorum longus and flexor hallucis longus in the region of the knot of Henry. *Clin Anat*. 2005;18(2):121–125. doi:10.1002/ca.20029.
91. Hill K, Saar WE, Lee TH, Berlet GC. Stage II flatfoot: what fails and why. *Foot Ankle Clin*. 2003;8(1):91–104.
92. Trnka HJ, Easley ME, Myerson MS. The role of calcaneal osteotomies for correction of adult flatfoot. *Clin Orthop*. 1999;(365):50–64.
93. Nyska M, Parks BG, Chu IT, Myerson MS. The contribution of the medial calcaneal osteotomy to the correction of flatfoot deformities. *Foot Ankle Int*. 2001;22(4):278–282.

94. Saltzman CL, El-Khoury GY. The Hindfoot Alignment View. *Foot Ankle Int.* 1995;16(9):572–576. doi:10.1177/107110079501600911.
95. Matheis E. Plantar Measurements to Determine Success of Surgical Correction of Stage IIb Adult Acquired Flatfoot Deformity. 2012. Available at: <https://digarchive.library.vcu.edu/handle/10156/4117>.
96. Chavhan GB, Babyn PS, Jankharia BG, Cheng H-LM, Shroff MM. Steady-State MR Imaging Sequences: Physics, Classification, and Clinical Applications1. *Radiographics.* 2008;28(4):1147–1160. doi:10.1148/rg.284075031.
97. Blackman AJ, Blevins JJ, Sangeorzan BJ, Ledoux WR. Cadaveric flatfoot model: Ligament attenuation and Achilles tendon overpull. *J Orthop Res.* 2009;27(12):1547–1554. doi:10.1002/jor.20930.
98. Fisk JP, Wayne JS. Development and validation of a computational musculoskeletal model of the elbow and forearm. *Ann Biomed Eng.* 2009;37(4):803–812.
99. Iaquinto J. The design and validation of a novel computational simulation of the leg for the investigation of injury, disease, and surgical treatment. 2010.
100. Spratley EM, Wayne JS. Computational Model of the Human Elbow and Forearm: Application to Complex Varus Instability. *Ann Biomed Eng.* 2010;39(3):1084–1091. doi:10.1007/s10439-010-0224-y.
101. Majors BJ, Wayne JS. Development and Validation of a Computational Model for Investigation of Wrist Biomechanics. *Ann Biomed Eng.* 2011;39(11):2807–2815. doi:10.1007/s10439-011-0361-y.
102. Elmore KA, Wayne JS. Soft tissue structures resisting anterior instability in a computational glenohumeral joint model. *Comput Methods Biomech Biomed Engin.* 2012. doi:10.1080/10255842.2011.641120.
103. *MIMICS Help Pages*. Materialise; 1992.
104. *3-Matic Help Pages*. Ann Arbor, MI: Insight Software Consortium
105. Field DA. Laplacian smoothing and Delaunay triangulations. *Commun Appl Numer Methods.* 1988;4(6):709–712. doi:10.1002/cnm.1630040603.
106. Buell WR, Bush BA. Mesh Generation—A Survey. *J Eng Ind.* 1973;95(1):332–338. doi:10.1115/1.3438132.

107. Wu G, Siegler S, Allard P, et al. ISB recommendation on definitions of joint coordinate system of various joints for the reporting of human joint motion—part I: ankle, hip, and spine. *J Biomech.* 2002;35(4):543–548. doi:10.1016/S0021-9290(01)00222-6.
108. Scott AT, Hendry TM, Iaquinio JM, Owen JR, Wayne JS, Adelaar RS. Plantar pressure analysis in cadaver feet after bony procedures commonly used in the treatment of stage II posterior tibial tendon insufficiency. *Foot Ankle Int.* 2007;28(11):1143–1153. doi:10.3113/FAI.2007.1143.
109. Logan BM, Singh D, Hutchings RT, McMinn RMH. *McMinn's color atlas of foot and ankle anatomy.* Mosby; 2004.
110. Rohen JW, Yokochi C, Lütjen-Drecoll E. *Color atlas of anatomy: a photographic study of the human body.* Lippincott Williams & Wilkins; 2006.
111. Structural Research and Analysis Corporation. *COSMOSMotion 2007 Help Pages.* Santa Monica, CA.: MSC Software Inc.; 2007.
112. Structural Research and Analysis Corporation. *COSMOSMotion Training Manual.* 2006.
113. Gear CW. The automatic integration of stiff ordinary differential equations. *Wash DC January 29-30 1968.* 1968:5.
114. Gear CW. The automatic integration of ordinary differential equations. *Commun ACM.* 1971;14(3):176–179.
115. Radin EL, Paul IL, Swann DA, Schottstaedt ES. Lubrication of synovial membrane. *Ann Rheum Dis.* 1971;30(3):322–325. doi:10.1136/ard.30.3.322.
116. Radin EL, Paul IL. A Consolidated Concept of Joint Lubrication. *J Bone Jt Surg.* 1972;54:607–616.
117. Kumar P, Oka M, Toguchida J, et al. Role of uppermost superficial surface layer of articular cartilage in the lubrication mechanism of joints. *J Anat.* 2001;199(3):241–250.
118. Sale D, Quinlan J, Marsh E, McComas AJ, Belanger AY. Influence of joint position on ankle plantarflexion in humans. *J Appl Physiol.* 1982;52(6):1636–1642.
119. Silver RL, Garza J de la, Rang M. The myth of muscle balance. A study of relative strengths and excursions of normal muscles about the foot and ankle. *J Bone Joint Surg Br.* 1985;67-B(3):432–437.

120. Thordarson DB, Schmotzer H, Chon J, Peters J. Dynamic support of the human longitudinal arch. A biomechanical evaluation. *Clin Orthop*. 1995;(316):165–172.
121. Fukunaga T, Roy RR, Shellock FG, Hodgson JA, Edgerton VR. Specific tension of human plantar flexors and dorsiflexors. *J Appl Physiol Bethesda Md* 1985. 1996;80(1):158–165.
122. Kitaoka HB, Luo ZP, An KN. Effect of the posterior tibial tendon on the arch of the foot during simulated weightbearing: biomechanical analysis. *Foot Ankle Int*. 1997;18(1):43–46.
123. Liacouras PC. Computational Modeling to Predict Mechanical Function of Joints: Validations and Applications of Lower Leg Simulations. 2008. Available at: <https://digarchive.library.vcu.edu/handle/10156/2097>.
124. Minns RJ, Hunter JA. The mechanical and structural characteristics of the tibio-fibular interosseous membrane. *Acta Orthop Scand*. 1976;47(2):236–240.
125. Pfaeffle HJ, Tomaino MM, Grewal R, et al. Tensile properties of the interosseous membrane of the human forearm. *J Orthop Res*. 1996;14(5):842–845.
126. Pfaeffle HJ, Fischer KJ, Srinivasa A, Manson T, Woo SL-Y, Tomaino M. A Model of Stress and Strain in the Interosseous Ligament of the Forearm Based on Fiber Network Theory. *J Biomech Eng*. 2006;128(5):725. doi:10.1115/1.2241730.
127. Attarian DE, McCrackin HJ, DeVito DP, McElhaney JH, Garrett WE Jr. Biomechanical characteristics of human ankle ligaments. *Foot Ankle*. 1985;6(2):54–58.
128. Siegler S, Block J, Schneck CD. The mechanical characteristics of the collateral ligaments of the human ankle joint. *Foot Ankle*. 1988;8(5):234–242.
129. Huang CK, Kitaoka HB, An KN, Chao EY. Biomechanical evaluation of longitudinal arch stability. *Foot Ankle Int*. 1993;14(6):353–357.
130. Kitaoka HB, Luo ZP, An KN. Effect of plantar fasciotomy on stability of arch of foot. *Clin Orthop*. 1997;(344):307–312.
131. Song Y, Debski RE, Musahl V, Thomas M, Woo SL-Y. A three-dimensional finite element model of the human anterior cruciate ligament: a computational analysis with experimental validation. *J Biomech*. 2004;37(3):383–390. doi:10.1016/S0021-9290(03)00261-6.

132. Pomeroy GC, Pike RH, Beals TC, Manoli A. Current concepts review-Acquired flatfoot in adults due to dysfunction of the posterior tibial tendon. *J Bone Jt Surg.* 1999;81(8):1173–1182.
133. Sangeorzan BJ, Mosca V, Hansen ST Jr. Effect of calcaneal lengthening on relationships among the hindfoot, midfoot, and forefoot. *Foot Ankle.* 1993;14(3):136–141.
134. Bryant A, Tinley P, Singer K. A comparison of radiographic measurements in normal, hallux valgus, and hallux limitus feet. *J Foot Ankle Surg.* 2000;39(1):39–43. doi:10.1016/S1067-2516(00)80062-9.
135. Bland JM, Altman DG. Measuring agreement in method comparison studies. *Stat Methods Med Res.* 1999;8(2):135–160. doi:10.1177/096228029900800204.
136. Lo H-C, Chu W-C, Wu W-K, et al. Comparison of radiological measures for diagnosing flatfoot. *Acta Radiol.* 2012;53(2):192–196. doi:10.1258/ar.2011.110387.
137. Chadha H, Pomeroy G, Manoli A. Radiologic Signs of Unilateral Pes Planus. *Foot Ankle Int.* 1997;18(9):603–604. doi:10.1177/107110079701800915.
138. Matheis EA, Spratley EM, Adelaar RS, Wayne JS. Pre-Operative and Post-Operative Plantar Pressures in Stage IIb Posterior Tibial Tendon Insufficiency. In: *Transactions of the 59th Annual Meeting of the Orthopaedic Research Society.* Vol 38. San Antonio, TX: ORS; 2013:1929.
139. Renstrom P, Wertz M, Incavo S, et al. Strain in the lateral ligaments of the ankle. *Foot Ankle.* 1988;9(2):59–63.
140. Ward KA, Soames RW. Morphology of the plantar calcaneocuboid ligaments. *Foot Ankle Int.* 1997;18(10):649–653.
141. Koutsogiannis E. Treatment of Mobile Flat Foot by Displacement Osteotomy of the Calcaneus. *J Bone Joint Surg Br.* 1971;53-B(1):96–100.
142. Otis JC, Deland JT, Kenneally S, Chang V. Medial arch strain after medial displacement calcaneal osteotomy: an in vitro study. *Foot Ankle Int.* 1999;20(4):222–226.
143. Myerson MS, Corrigan J, Thompson F, Schon LC. Tendon Transfer Combined with Calcaneal Osteotomy for Treatment of Posterior Tibial Tendon Insufficiency: A Radiological Investigation. *Foot Ankle Int.* 1995;16(11):712–718. doi:10.1177/107110079501601108.

144. Tellisi N, Lobo M, O'Malley M, Kennedy JG, Elliott AJ, Deland JT. Functional Outcome after Surgical Reconstruction of Posterior Tibial Tendon Insufficiency in Patients under 50 Years. *Foot Ankle Int.* 2008;29(12):1179–1183. doi:10.3113/FAI.2008.1179.
145. Scott G, Menz HB, Newcombe L. Age-related differences in foot structure and function. *Gait Posture.* 2007;26(1):68–75. doi:10.1016/j.gaitpost.2006.07.009.
146. Resnick RB, Jahss MH, Choueka J, Kummer F, Hersch JC, Okereke E. Deltoid Ligament Forces after Tibialis Posterior Tendon Rupture: Effects of Triple Arthrodesis and Calcaneal Displacement Osteotomies. *Foot Ankle Int.* 1995;16(1):14–20. doi:10.1177/107110079501600104.
147. Horton GA, Myerson MS, Parks BG, Park YW. Effect of calcaneal osteotomy and lateral column lengthening on the plantar fascia: a biomechanical investigation. *Foot Ankle Int.* 1998;19(6):370–373.
148. Thordarson DB, Merkle P, Hedman T, Liao W-L. An evaluation of the inversion torque of the posterior tibialis versus flexor digitorum longus and flexor hallucis longus posterior tibialis tendon reconstructions. *The Foot.* 1996;6(3):134–137. doi:10.1016/S0958-2592(96)90006-1.
149. Funk DA, Cass JR, Johnson KA. Acquired adult flat foot secondary to posterior tibial-tendon pathology. *J Bone Joint Surg Am.* 1986;68(1):95–102.
150. Mosca VS. Flexible flatfoot and skewfoot. *J Bone Jt Surg.* 1995;77(12):1937–1945.
151. Davitt JS, Beals TC, Bachus KN. The effects of medial and lateral displacement calcaneal osteotomies on ankle and subtalar joint pressure distribution. *Foot Ankle Int.* 2001;22(11):885–889.



## **ADDITIONAL ACKNOWLEDGMENTS**

Thanks to Primal Pictures® for the use of the Anatomy.TV service whose pictures served as the starting point from which many of the illustrations were adapted.

## APPENDIX A

### LIST OF ABBREVIATIONS

#### *General Abbreviations*

|        |   |
|--------|---|
| AAFD   | Adult acquired flatfoot deformity                     |
| ADAMS  | Automated Dynamic Analysis Of Mechanical Systems      |
| AP     | Anteroposterior                                       |
| BMI    | Body mass index                                       |
| CAD    | Computer aided design                                 |
| CT     | Computed tomography                                   |
| DESS   | Dual echo steady state                                |
| DICOM  | Digital Imaging And Communications In Medicine format |
| EMG    | Electromyography                                      |
| FAOS   | Foot And Ankle Outcome Scores                         |
| FEA    | Finite Element Analysis method                        |
| GSTIFF | Gear stiff numerical integrator                       |
| HU     | Hounsfield unit                                       |
| IRB    | Institutional Review Board                            |
| MCO    | Medializing Calcaneal Osteotomy                       |
| ML     | Mediolateral  |
| mm     | Millimeter  |
| MRI    | Magnetic Resonance Imaging                            |
| N/mm   | Newtons per millimeter                                |
| O      | Origin  |
| PA     | Posteroanterior                                       |
| PCSA   | Physiologic Cross-Sectional Area                      |
| $R^2$  | Coefficients Of Determination                         |
| SF-36  | General health form                                   |
| SIMM   | Software For Interactive Musculoskeletal Modeling     |
| stdev  | Standard deviation                                    |
| TIRM   | Turbo Inversion Recovery                              |
| TSE    | Turbo Spin Echo                                       |
| *.csv  | Comma delimited file                                  |

|       |                        |
|-------|------------------------|
| *.stl | Stereolithography file |
| ±     | Plus or minus          |
| °     | Angle                  |
| 2-D   | Two dimensional        |
| 3-D   | Three dimensional      |

### *Anatomic Abbreviations*

|        |  |
|--------|--|
| DEL_*  | Deltoid tissue                             |
| DIST_* | Distal metatarsal tissue                   |
| DOR_*  | Dorsal tissue                              |
| IOL_*  | Talocalcaneal interosseous tissue          |
| IOM_*  | Tibiofibular interosseous membrane tissue  |
| LCL_*  | Lateral collateral ligament complex tissue |
| MCL_*  | Medial collateral ligament complex tissue  |
| PLAN_* | Plantar tissue                             |
| PROX_* | Proximal tibiofibular tissue               |
| CCC    | Calcaneocuboid Capsule                     |
| FDL    | Flexor Digitorum Longus                    |
| FHL    | Flexor Hallucis Longus                     |
| IM     | Intermalleolar                             |
| IMCN   | Inferomedial Calcaneonavicular             |
| INTCn  | Intercuneiform Tissue                      |
| INTMt  | Intermetatarsal Tissue                     |
| IOL    | Talocalcaneal Interosseous Ligaments       |
| IOM    | Interosseous Membrane                      |
| LCL    | Lateral Collateral Ligaments               |
| LP     | Long Plantar Ligament                      |
| MCL    | Medial Collateral Ligaments                |
| MCN    | Middle Calcaneonavicular Ligament          |
| PB     | Peroneus Brevis                            |
| PF     | Plantar Fascia                             |
| PL     | Peroneus Longus                            |
| PTT    | Posterior Tibialis Tendon                  |
| SFR    | Superficial Fibular Retinaculum            |
| SMCN   | Superomedial Calcaneonavicular Ligament    |

### *X-ray measure Abbreviations*

|              |   |
|--------------|---|
| AP-T1MT      | Anteroposterior Talar 1st Metatarsal Angle              |
| AP-T2MT      | Anteroposterior Talar 2nd Metatarsal Angle              |
| AP-TN        | Anteroposterior Talonavicular Angle                     |
| ML-C1MT      | Mediolateral Calcaneal 1st Metatarsal Angle             |
| ML-CP        | Mediolateral Calcaneal Pitch Angle                      |
| ML-T1MT      | Mediolateral Talo-1st Metatarsal Angle                  |
| ML-TC        | Mediolateral Talocalcaneal Angle                        |
| ML-Tdec      | Mediolateral Talar Declination Angle                    |
|              |   |
| AP-TNuncov-h | Anteroposterior Talonavicular Uncoverage Distance       |
| ML-1CN-h     | Mediolateral 1st Cuneiform Height                       |
| ML-1CN/5MT-h | Mediolateral 1st Cuneiform To The 5th Metatarsal Height |
| ML-Cub-h     | Mediolateral Cuboid Height                              |
| ML-Nav-h     | Mediolateral Navicular Height                           |
| ML-Tal-h     | Mediolateral Talar Height                               |

## APPENDIX B

### STL CHARACTERISTICS

#### Volume BEFORE Surface Modification (mm<sup>3</sup>)

|                       | P1       | P2       | P3       | P4       | P5       | P6       | AVG             | STD            |
|-----------------------|----------|----------|----------|----------|----------|----------|-----------------|----------------|
| Tibia†                | 41518.97 | 52372.86 | 56306.49 | 58594.06 | 65494.47 | 65919.46 | <b>56701.05</b> | <b>9113.41</b> |
| Fibula†               | 12345.32 | 12310.98 | 15737.80 | 15925.07 | 19714.53 | 17484.25 | <b>15586.33</b> | <b>2898.75</b> |
| Talus                 | 27697.60 | 22697.95 | 22952.69 | 28382.55 | 28677.31 | 26364.37 | <b>26128.74</b> | <b>2681.39</b> |
| Calcaneus             | 49411.77 | 40634.76 | 50917.21 | 50573.55 | 55543.45 | 50097.65 | <b>49529.73</b> | <b>4871.07</b> |
| Navicular             | 8120.50  | 6539.98  | 9098.64  | 8814.10  | 12526.44 | 8721.22  | <b>8970.15</b>  | <b>1968.64</b> |
| Cuboid                | 7543.67  | 8635.72  | 9680.52  | 9570.91  | 12641.41 | 10735.46 | <b>9801.28</b>  | <b>1758.52</b> |
| 1 <sup>st</sup> CN    | 7174.60  | 6349.27  | 7804.94  | 6892.13  | 9820.57  | 9101.98  | <b>7857.25</b>  | <b>1347.46</b> |
| 2 <sup>nd</sup> CN    | 3357.42  | 2941.40  | 3528.81  | 3212.18  | 3791.07  | 3200.73  | <b>3338.60</b>  | <b>294.62</b>  |
| 3 <sup>rd</sup> CN    | 4592.31  | 3655.76  | 4520.92  | 4476.74  | 5415.87  | 5580.32  | <b>4706.98</b>  | <b>703.01</b>  |
| 1 <sup>st</sup> Met.  | 10416.82 | 12836.47 | 12432.17 | 12989.10 | 14223.68 | 17233.25 | <b>13355.25</b> | <b>2266.39</b> |
| 2 <sup>nd</sup> Met.  | 4741.76  | 6819.41  | 6397.15  | 5929.39  | 6263.24  | 8660.34  | <b>6468.55</b>  | <b>1284.27</b> |
| 3 <sup>rd</sup> Met.  | 4497.75  | 5195.63  | 5734.55  | 4747.31  | 6483.94  | 9507.82  | <b>6027.83</b>  | <b>1848.13</b> |
| 4 <sup>th</sup> Met.  | 4656.82  | 4964.70  | 5808.87  | *        | 6902.45  | 7335.46  | <b>5933.66</b>  | <b>1171.37</b> |
| 5 <sup>th</sup> Met.† | 3684.04  | 4930.45  | 7786.80  | *        | 5297.81  | 7950.18  | <b>5929.86</b>  | <b>1868.95</b> |

#### Volume AFTER Surface Modification (mm<sup>3</sup>)

|                       | P1       | P2       | P3       | P4       | P5       | P6       | AVG             | STD            |
|-----------------------|----------|----------|----------|----------|----------|----------|-----------------|----------------|
| Tibia†                | 41313.37 | 52356.64 | 56277.82 | 58590.77 | 65480.98 | 65906.21 | <b>56654.30</b> | <b>9178.39</b> |
| Fibula†               | 12343.96 | 12307.38 | 15727.99 | 15925.36 | 19707.25 | 17479.55 | <b>15581.92</b> | <b>2897.09</b> |
| Talus                 | 27537.41 | 22694.75 | 22947.68 | 28372.05 | 28605.75 | 26361.27 | <b>26086.48</b> | <b>2649.80</b> |
| Calcaneus             | 49149.82 | 40630.12 | 50896.14 | 50564.79 | 55535.96 | 50091.36 | <b>49478.03</b> | <b>4871.55</b> |
| Navicular             | 8119.57  | 6539.02  | 9146.02  | 8813.47  | 12527.26 | 8648.53  | <b>8965.64</b>  | <b>1972.09</b> |
| Cuboid                | 7542.76  | 8635.03  | 9675.78  | 9549.15  | 12631.53 | 10736.37 | <b>9795.10</b>  | <b>1756.41</b> |
| 1 <sup>st</sup> CN    | 7173.25  | 6348.38  | 7796.14  | 6891.13  | 9819.21  | 9012.41  | <b>7840.09</b>  | <b>1331.43</b> |
| 2 <sup>nd</sup> CN    | 3326.10  | 2941.11  | 3526.57  | 3185.86  | 3790.67  | 3200.13  | <b>3328.41</b>  | <b>296.56</b>  |
| 3 <sup>rd</sup> CN    | 4559.27  | 3655.37  | 4518.44  | 4474.77  | 5415.27  | 5583.78  | <b>4701.15</b>  | <b>705.32</b>  |
| 1 <sup>st</sup> Met.  | 10414.78 | 12821.22 | 12403.14 | 12973.32 | 14077.57 | 17228.94 | <b>13319.83</b> | <b>2258.48</b> |
| 2 <sup>nd</sup> Met.  | 4740.72  | 6797.27  | 6391.20  | 5922.80  | 6260.83  | 8657.29  | <b>6461.68</b>  | <b>1283.02</b> |
| 3 <sup>rd</sup> Met.  | 4497.00  | 5193.29  | 5728.10  | 4710.39  | 6481.76  | 9406.42  | <b>6002.83</b>  | <b>1815.63</b> |
| 4 <sup>th</sup> Met.  | 4655.34  | 4963.95  | 5801.38  | *        | 6900.23  | 7333.38  | <b>5930.86</b>  | <b>1171.04</b> |
| 5 <sup>th</sup> Met.† | 3682.13  | 4920.68  | 7724.10  | *        | 5295.25  | 7947.54  | <b>5913.94</b>  | <b>1854.89</b> |

| Change in Volume (mm <sup>3</sup> ) |        |        |        |        |        |        |        |
|-------------------------------------|--------|--------|--------|--------|--------|--------|--------|
|                                     | P1     | P2     | P3     | P4     | P5     | P6     |        |
|                                     |        |        |        |        |        |        | AVG    |
|                                     |        |        |        |        |        |        | STD    |
| Tibia†                              | -0.495 | -0.031 | -0.051 | -0.006 | -0.021 | -0.020 | -0.104 |
| Fibula†                             | -0.011 | -0.029 | -0.062 | 0.002  | -0.037 | -0.027 | 0.192  |
| Talus                               | -0.578 | -0.014 | -0.022 | -0.037 | -0.250 | -0.012 | -0.027 |
| Calcaneus                           | -0.530 | -0.011 | -0.041 | -0.017 | -0.013 | -0.013 | 0.228  |
| Navicular                           | -0.012 | -0.015 | 0.521  | -0.007 | 0.007  | -0.833 | -0.104 |
| Cuboid                              | -0.012 | -0.008 | -0.049 | -0.227 | -0.078 | 0.008  | 0.209  |
| 1 <sup>st</sup> CN                  | -0.019 | -0.014 | -0.113 | -0.014 | -0.014 | -0.984 | -0.057 |
| 2 <sup>nd</sup> CN                  | -0.933 | -0.010 | -0.064 | -0.819 | -0.011 | -0.019 | 0.435  |
| 3 <sup>rd</sup> CN                  | -0.719 | -0.010 | -0.055 | -0.044 | -0.011 | 0.062  | -0.061 |
| 1 <sup>st</sup> Met.                | -0.020 | -0.119 | -0.233 | -0.121 | -1.027 | -0.025 | 0.087  |
| 2 <sup>nd</sup> Met.                | -0.022 | -0.325 | -0.093 | -0.111 | -0.038 | -0.035 | -0.193 |
| 3 <sup>rd</sup> Met.                | -0.017 | -0.045 | -0.113 | -0.778 | -0.034 | -1.067 | 0.390  |
| 4 <sup>th</sup> Met.                | -0.032 | -0.015 | -0.129 | *      | -0.032 | -0.028 | -0.309 |
| 5 <sup>th</sup> Met.†               | -0.052 | -0.198 | -0.805 | *      | -0.048 | -0.033 | 0.441  |
|                                     |        |        |        |        |        |        | -0.130 |
|                                     |        |        |        |        |        |        | 0.292  |
|                                     |        |        |        |        |        |        | -0.258 |
|                                     |        |        |        |        |        |        | 0.385  |
|                                     |        |        |        |        |        |        | -0.104 |
|                                     |        |        |        |        |        |        | 0.114  |
|                                     |        |        |        |        |        |        | -0.342 |
|                                     |        |        |        |        |        |        | 0.460  |
|                                     |        |        |        |        |        |        | -0.047 |
|                                     |        |        |        |        |        |        | 0.046  |
|                                     |        |        |        |        |        |        | -0.227 |
|                                     |        |        |        |        |        |        | 0.330  |
| Average                             | -0.246 | -0.060 | -0.094 | -0.182 | -0.115 | -0.216 | -0.151 |

**Table APPENDIX B: The volumes of all bone STLs in each patient model. †: Volume only represents the portion bone within the MRI field of view. \*: Metal artifacts made imaging these bones impossible.**

## APPENDIX C

### LIGAMENT PROPERTIES

| #            | Ligament Element | Stiffness<br>(N/mm) | #          | Ligament Element | Stiffness<br>(N/mm) |
|--------------|------------------|---------------------|------------|------------------|---------------------|
| 1 $\delta$   | DEL_TiCa-1       | 200                 | 43         | DOR_INTMt_3-4    | 90                  |
| 2 $\delta$   | DEL_TiCa-2       | 200                 | 44         | DOR_INTMt_4-5    | 90                  |
| 3 $\gamma$   | DEL_TiNa-1       | 40                  | 45         | DOR_TaNa-1       | 120                 |
| 4 $\gamma$   | DEL_TiNa-2       | 40                  | 46         | DOR_TaNa-2       | 120                 |
| 5 $\gamma$   | DEL_TiSp-1       | 61                  | 47 $\zeta$ | IOL_TaCa-1       | 90                  |
| 6 $\gamma$   | DEL_TiSp-2       | 200                 | 48 $\zeta$ | IOL_TaCa-2       | 90                  |
| 7            | DEL_TiTa-A       | 90                  | 49 $\zeta$ | IOL_TaCa-3       | 90                  |
| 8 $\epsilon$ | DEL_TiTa-P1      | 117                 | 50         | IOM_TiFi-1       | 126                 |
| 9 $\epsilon$ | DEL_TiTa-P2      | 117                 | 51         | IOM_TiFi-2       | 126                 |
| 10           | DIST_INTMt_1-2   | 90                  | 52         | IOM_TiFi-3       | 126                 |
| 11           | DIST_INTMt_2-3   | 90                  | 53         | IOM_TiFi-4       | 126                 |
| 12           | DIST_INTMt_3-4   | 90                  | 54         | IOM_TiFi-5       | 126                 |
| 13           | DIST_INTMt_4-5   | 90                  | 55         | IOM_TiFi-6       | 126                 |
| 14           | DOR_CaCu-1       | 90                  | 56         | IOM_TiFi-7       | 126                 |
| 15           | DOR_CaCu-2       | 90                  | 57         | LCL_CaCu         | 90                  |
| 16           | DOR_Cn1MT-1      | 90                  | 58         | LCL_CaFi-1       | 64                  |
| 17           | DOR_Cn1MT-2      | 90                  | 59         | LCL_CaFi-2       | 64                  |
| 18           | DOR_Cn1MT-3      | 90                  | 60         | LCL_CaNa         | 120                 |
| 19           | DOR_Cn1MT-4      | 90                  | 61         | LCL_SFR-1        | 90                  |
| 20           | DOR_Cn1MT-5      | 90                  | 62         | LCL_SFR-2        | 90                  |
| 21           | DOR_Cn2MT-1      | 90                  | 63         | LCL_TaCa-L       | 90                  |
| 22           | DOR_Cn2MT-2      | 90                  | 64         | LCL_TaFi-A       | 142                 |
| 23           | DOR_Cn2MT-3      | 90                  | 65         | LCL_TaFi-P1      | 82                  |
| 24           | DOR_Cn3MT-1      | 90                  | 66         | LCL_TaFi-P2      | 82                  |
| 25           | DOR_Cn3MT-2      | 90                  | 67         | LCL_TiFi-A1      | 120                 |
| 26           | DOR_CnCu-1       | 120                 | 68         | LCL_TiFi-A2      | 120                 |
| 27           | DOR_CnCu-2       | 120                 | 69         | LCL_TiFi-P       | 90                  |
| 28           | DOR_CnNa-1       | 120                 | 70         | MCL_TaCa-M       | 120                 |
| 29           | DOR_CnNa-2       | 120                 | 71         | MCL_TaCa-P1      | 90                  |
| 30           | DOR_CnNa-3       | 120                 | 72         | MCL_TaCa-P2      | 90                  |
| 31           | DOR_CnNa-4       | 120                 | 73         | PLAN_CaCu-1      | 90                  |
| 32           | DOR_CnNa-5       | 120                 | 74         | PLAN_CaCu-2      | 90                  |
| 33           | DOR_CnNa-6       | 120                 | 75         | PLAN_CaCu-3      | 90                  |
| 34           | DOR_Cu4MT-1      | 90                  | 76         | PLAN_CaCu-INF-1  | 30                  |
| 35           | DOR_Cu4MT-2      | 90                  | 77         | PLAN_CaCu-INF-2  | 30                  |
| 36           | DOR_Cu5MT-1      | 90                  | 78         | PLAN_CaCu-INF-3  | 30                  |
| 37           | DOR_Cu5MT-2      | 90                  | 79         | PLAN_CCC-1       | 90                  |
| 38           | DOR_CuNa         | 120                 | 80         | PLAN_CCC-2       | 90                  |
| 39           | DOR_INTCn-1      | 120                 | 81         | PLAN_CCC-3       | 90                  |
| 40           | DOR_INTCn-2      | 120                 | 82         | PLAN_Cn1MT-1     | 90                  |
| 41           | DOR_INTMt_1-2    | 90                  | 83         | PLAN_Cn1MT-2     | 90                  |
| 42           | DOR_INTMt_2-3    | 90                  | 84         | PLAN_Cn2MT-1     | 90                  |

Continued:

| #          | Ligament Element   | Stiffness<br>(N/mm) | #            | Ligament Element   | Stiffness<br>(N/mm) |
|------------|--------------------|---------------------|--------------|--------------------|---------------------|
| 86         | PLAN_Cn2MT-3       | 90                  | 117          | PLAN_INTMt_3-4     | 90                  |
| 87         | PLAN_Cn3MT         | 90                  | 118          | PLAN_INTMt_4-5     | 90                  |
| 88         | PLAN_Cn4MT         | 90                  | 119          | PLAN_LP_BASE-1     | 75                  |
| 89         | PLAN_CnCu-1        | 90                  | 120          | PLAN_LP_BASE-2     | 75                  |
| 90         | PLAN_CnCu-2        | 90                  | 121          | PLAN_LP_BASE-3     | 75                  |
| 91         | PLAN_CnNa-1        | 90                  | 122          | PLAN_LP_BASE-4     | 75                  |
| 92         | PLAN_CnNa-2        | 90                  | 123          | PLAN_LP_BASE-5     | 75                  |
| 93         | PLAN_Cu4MT         | 90                  | 124          | PLAN_LP_BASE-6     | 75                  |
| 94         | PLAN_Cu5MT-1       | 90                  | 125          | PLAN_LP_END2-1     | 40                  |
| 95         | PLAN_Cu5MT-2       | 90                  | 126          | PLAN_LP_END2-2     | 40                  |
| 96         | PLAN_Cu5MT-3       | 90                  | 127          | PLAN_LP_END3-1     | 40                  |
| 97         | PLAN_CuNa-1        | 90                  | 128          | PLAN_LP_END3-2     | 40                  |
| 98         | PLAN_CuNa-2        | 90                  | 129          | PLAN_LP_END4-1     | 40                  |
| 99 $\eta$  | PLAN_FASCIA_BASE-1 | 40                  | 130          | PLAN_LP_END4-2     | 40                  |
| 100 $\eta$ | PLAN_FASCIA_BASE-2 | 40                  | 131          | PLAN_LP_LAT_o5-1   | 40                  |
| 101 $\eta$ | PLAN_FASCIA_BASE-3 | 40                  | 132          | PLAN_LP_LAT_o5-2   | 40                  |
| 102 $\eta$ | PLAN_FASCIA_BASE-4 | 40                  | 133 $\beta$  | PLAN_SPRING_IMCN-1 | 45                  |
| 103 $\eta$ | PLAN_FASCIA_BASE-5 | 40                  | 134 $\beta$  | PLAN_SPRING_IMCN-2 | 45                  |
| 104 $\eta$ | PLAN_FASCIA_END-1  | 60                  | 135 $\alpha$ | PLAN_SPRING_MCN-1  | 18.3                |
| 105 $\eta$ | PLAN_FASCIA_END-2  | 50                  | 136 $\alpha$ | PLAN_SPRING_MCN-2  | 18.3                |
| 106 $\eta$ | PLAN_FASCIA_END-3  | 50                  | 137 $\alpha$ | PLAN_SPRING_SMCN-1 | 18.3                |
| 107 $\eta$ | PLAN_FASCIA_END-4  | 20                  | 138 $\alpha$ | PLAN_SPRING_SMCN-2 | 18.3                |
| 108 $\eta$ | PLAN_FASCIA_END-5  | 20                  | 139 $\alpha$ | PLAN_SPRING_SMCN-3 | 18.3                |
| 109        | PLAN_FASCIA_LAT-1  | 150                 | 140 $\alpha$ | PLAN_SPRING_SMCN-4 | 18.3                |
| 110        | PLAN_FASCIA_LAT-2  | 150                 | 141          | PROX_TiFi-1        | 200                 |
| 111        | PLAN_INTCn-1       | 90                  | 142          | PROX_TiFi-2        | 200                 |
| 112        | PLAN_INTCn-2       | 90                  | 143          | PROX_TiFi-3        | 200                 |
| 113        | PLAN_INTCn-3       | 90                  | 144          | PROX_TiFi-4        | 200                 |
| 114        | PLAN_INTCn-4       | 90                  | 145          | PROX_TiFi-5        | 200                 |
| 115        | PLAN_INTMt_1-2     | 90                  | 146          | PROX_TiFi-6        | 200                 |

**Table APPENDIX C: Properties for the soft-tissue elements listed alphabetically. All elements incorporated 4.0% in situ strain.  $\alpha$ : Superior Medial Spring Ligament;  $\beta$ : Inferior Medial Spring Ligament;  $\gamma$ : Anterior Deltoid;  $\delta$ : Posterior Deltoid;  $\epsilon$ : Deep Deltoid;  $\zeta$ : Talocalcaneal Interosseous Ligaments;  $\eta$ : Plantar Fascia.**



## APPENDIX D

7/27/2010

### What is AAFD?

Adult Acquired Flatfoot Deformity is when the arch of the foot becomes flat usually resulting in pain and discomfort, particularly during walking.





### Research Study

We will be conducting a research study using non-invasive gait analysis, Xray, and MRI technology to test mechanical functioning of your ankle joint and the effects of correction. You will be paid \$20/session for participation. Each session will take 30-60 minutes for 7 sessions (several of which can be done on the same day).

### Benefits of Participation

- ❖ You will be able to help future cases
- ❖ It may be fun to participate!



Please contact Dr. Jennifer Wayne [jwayne@vcu.edu](mailto:jwayne@vcu.edu) 804.828.2595  
for participation Dr. Robert Adelaar [radelaar@mcvh-vcu.edu](mailto:radelaar@mcvh-vcu.edu) 804.828.6784



## **APPENDIX E**

*See attached IRB PDFs.*

Title:

In Vivo And In Silico Functional Performance Of The Foot/Ankle Complex Before And  
After Corrective Procedures For Posterior Tibial Tendon Insufficiency

VCU IRB Protocol Number:

HM13044

INVESTIGATOR:

Robert S. Adelaar, M.D., Jennifer S. Wayne, PhD

## VITA

Edward Meade Spratley was born on September 25th, 1981 in the south side of Richmond, VA and remains an American citizen. He graduated from Powhatan County High School and later attended the University of Virginia, where he majored in Biochemistry. Following graduation he traveled the West and Southwest working in the outdoor industry with his now wife, Jennifer. In 2007, they moved back to Central Virginia where he was enrolled in a Master's of Science program at Virginia Commonwealth University under the guidance of Dr. Jennifer Wayne. Meade graduated in 2009 and continued on into a doctoral program within the Orthopaedics Research Laboratory. During his time at VCU, Meade has been a student, a teaching assistant, and a researcher. He was inducted into the Alpha Eta Mu Beta Honors Society in 2009, awarded the Phi Kappa Phi Honors Society Scholarship in 2009, and the VCU School of Engineering Special Recognition for Teaching Excellence in 2011. He has served as a member of two tenure and promotion committees, as well as a member of VAS, ASME, and ORS throughout his time at VCU and is currently serving as an inaugural member of the ASME Student Leadership Council. Meade has authored or coauthored six journal articles currently in print or review, one of which was selected as the journal's cover, and ten national conference presentations in the fields of musculoskeletal modeling, in vitro surgical investigation of flatfoot, varus elbow dysfunction, foot and ankle pathology, and acetabular morphology. Upon graduation, Meade will be taking an industry position focused on device design and musculoskeletal mechanics.